Microstructural Control for Creation of High Strength Cast Aluminum Alloys

By

Shaohua Wu

Graduate School of Natural Science and Technology
OKAYAMA UNIVERSITY

A thesis submitted in conformity with the requirements for the degree of Doctor of Philosophy in Okayama University

Abstract

The development of engineering technologies, such as automobiles and electric appliances, makes our daily lives better, and there would be no lack of anything in our lives. However, it seems to be lost sight of something. Now we are required to consider several global issues, and one of them is global warming. This is because a large amount of greenhouse gas CO_2 is exhausted from automobiles and factories to the atmosphere. The temperature of some countries has been growing up sharply, e.g., more than 50 °C, so it can be predicted to have technical difficulty to live on the earth in the future if our lives are not altered.

In order to reduce emission gas from automobiles, an improvement of fuel efficiency is needed. The weight reduction of automobiles is a significant approach: replacement of lightweight materials can be used instead of steel based parts. Aluminum alloy is one of the candidate materials to employ for automobile parts, as a density of Al is about 1/3 of iron. Although Al alloys have been used for automobile parts, such as transmission cases, wheels, and cylinder blocks, the applications of the parts are limited because of their low mechanical properties. The ultimate tensile strength (UTS) of cast Al alloys is less than half of that of ferrous foundry alloys. In this thesis, an attempt was made to create the high mechanical properties of cast Al alloys via controlling the microstructural characteristics, e.g., solidification speed and direction, precipitation and addition of alloying element. The results obtained are summarized as follows:

Firstly, solidification control was carried out to make an adjustment of the size and shape of the grain and eutectic structure of Al-Si-Cu alloy. The samples were created by an original unidirectional casting process with a controlling cooling. The microstructural properties of the cast sample depended on the cooling rate: relatively finer and coarser grain size obtained with cooling rates of 0.14 $°C \cdot s^{-1}$ and 0.02 $°C \cdot s^{-1}$, respectively. The mean secondary dendrite arm spacing (SDAS) of the finer grain size was about 50 μm, which led to a higher tensile strength. The crystal structure was also changed by the cooling rate and resulted in the amount of Si present during solidification. With a higher cooling rate, the α-Al phase formed a relatively organized crystal structure. In contrast, when the cooling rate was a low level of < 0.05 $°C \cdot s^{-1}$, the crystal structure was randomly formed because of the interference of the coarsened Si phase. As a result, fine grain size (SDAS = 11.9 μm) and crystal structure which is almost perfectly formed with $\langle 100 \rangle$ were obtained with cooling rate of 200.5 $°C \cdot s^{-1}$, which made excellent mechanical properties of UTS 330 MPa and fracture strain 12%.

Secondly, the microstructure was controlled by heat treatment to make precipitation hardening. Artificial aging was performed under various conditions after solution treatment. Two cast samples were employed: gravity casting (GC) and heated mold continuous casting (HMC). The samples were solution-treated and then aged under a temperature of 145 to 220 °C and aging time of 1 to 200 h. Hardness changed with aging time: hardness increased with aging for several hours

but decreased with aging for a long time. This was caused by the density and size of the precipitation: θ'(Al_2Cu) metastable phase in the α-Al phase. The highest hardness was obtained under the condition of 175 °C for 13 h. The Vickers hardness of the GC sample was higher than that of the HMC sample under all heat treatment conditions. It was because of the high solubility of the alloying elements in the α-Al matrix of GC samples. In contrast to the hardness results, the UTS of the as-cast GC sample was about 30% lower than that of the HMC sample due to the large brittle eutectic Si and Fe structures. The highest UTS was obtained with the HMC samples aged at 175 °C for 13 h, approximately 390 MPa, which is 20% higher than that of the as-cast HMC sample. The high UTS of the HMC sample was affected by the high-density fine precipitation and the formation of small microstructures. The excellent ductility, e.g., fracture strain 28%, was obtained for the HMC sample aged at 175 °C for 100 h because of the unidirectional crystal structure and over-aging.

Thirdly, rare-earth (RE) elements such as Sr, Sb and Bi were added to Al-Si-Cu (ADC12) alloy to refine the eutectic Si phase. The samples with the addition of three RE elements: 0.04 ~ 0.06Sr, 0.25 ~ 0.75Sb, 0.5 ~ 1.5Bi were prepared by the HMC process. The addition of RE elements significantly changed the size and shape of the eutectic Si phase. For all samples, the size of the eutectic Si phase was refined. In particular, with the addition of 0.5Sb, 0.04Sr and 1.0Bi, the fine eutectic Si phases were obtained: the mean area of the Si phase was less than 0.2 μm^2. In contrast to the result of the size, the shape showed different results: the addition of 0.04Sr produced a fine spherical eutectic Si phase, but the addition of Sb and Bi produced a fine layered eutectic Si phase. In addition, the unidirectional crystal structure collapsed by increasing of Sr added. The mechanical properties of the ADC12-Sr alloy increased with increasing Sr content due to the fine eutectic Si phase and random crystal structure. The high UTS, approximately 380 MPa, was obtained for ADC12-0.06Sr alloy. On the other hand, the ductility increases with the increasing addition of Bi, and the high fracture strain was obtained for the ADC12-1.5Bi alloy.

In this thesis, the mechanical properties of cast aluminum alloys created by microstructural control (solidification, precipitation, and the addition of alloy elements) were systematically investigated. From this work, the mechanical properties can be improved and the high UTS 390 MPa was obtained, which is closed to some ferrous foundry alloys. We believe that this work may contribute to new applications of casting aluminum alloys in automobile parts.

Acknowledgements

I am taking this as an opportunity to express my sincere acknowledgements to the following personalities who have directly and indirectly helped me finish my Ph.D. studies.

I would like to express my sincere gratitude to Professor Mitsuhiro Okayasu for his guidance and cooperation in this research. His advice encouraged me to achieve better results in my research by changing how I logically and rationally analyze and solve problems as an objective researcher.

I am grateful to Professor Naoya Tada, Associate Professor Yoshito Takemoto, and Associate Professor Yuta Nishina for their many suggestions for my research. Moreover, I wish to express my gratitude to all the Structural Materials Engineering Laboratory members who gave me valuable advice and helped my experiments.

I would also appreciate Mr. Shuhei Takeuchi for his support, suggestions, and encouragement.

Finally, I would like to express my sincere gratitude to my parents for their continuous support and encouragement. And a special thank is due to my wife Landi Li for her support and encouragement.

Last but not least, I would like to thank many other organizations and individuals not listed above for every kind of support, help, and cooperation in this work.

Published reference

The research work presented in thesis has resulted in the following publications

Refereed Papers:

(i) Effects of Sb, Sr and Bi on the material properties of cast Al-Si-Cu alloys produced through heated mold continuous casting
Mitsuhiro Okayasu, Shuhei Takeuchi, **Shaohua Wu** and Toshihiro Ochi
Journal of Mechanical Science and Technology, Vol. 30, No. 3, pp. 1139-1147 (2016).

(ii) Method for reducing aluminum alloy heat loss in high pressure die casting shot sleeves
M. Okayasu, **S. Wu**, T. Hirayama and Y.-S. Lee
International Journal of Cast Metals Research, Vol. 31, No. 5, pp. 308-316 (2018).

(iii) Microstructural Characteristics of Unidirectionally Solidified Cast Al–Si–Cu Alloy
Shaohua Wu, Mitsuhiro Okayasu and Tatsuya Kuwada
International Journal of Metalcasting, Vol. 15, No. 3, pp. 1073-1083 (2021).

Other Papers:

(i) Precise analysis of effects of aging on mechanical properties of cast ADC12 aluminum alloy
Mitsuhiro Okayasu, **Shoka Go**
Materials Science and Engineering A, Vol. 638, No. 25, pp. 208-218 (2015).

(ii) Material Properties of High-Speed Steel Rolls
Shaohua Wu, Mitsuhiro Okayasu, Shuhei Takeuchi, Toshiro Tanaka, T. Ikeda, T. Takahashi, R. Kikuchi, A. Hamabe, D. Ochi
International Journal on Smart Material and Mechatronics, Vol. 3, No. 1, pp. 156-159 (2016).

(iii) Mechanical properties of austenitic stainless steel with high niobium contents
M. Okayasu, **S. Wu**, K. Noda, D.-Y. Lin and S.-M. Yang
Materials Science and Technology, Vol. 32, No. 13, pp. 1382-1394 (2016).

(iv) Mechanical Properties of Magnesium Alloys Produced by the Heated Mold Continuous Casting Process
M. Okayasu, **S. Wu**, T. Tanimoto, S. Takeuchi
Archives of Foundry Engineering, Vol. 16, No. 4, pp. 208-216 (2016).

(v) Effects of Oxide Scale on the Corrosion and Mechanical Properties for a High Speed Steel and a Graphite Cast Iron
Mitsuhiro Okayasu, **Shaohua Wu**
Oxidation of Metals, Vol. 87, No. 1, pp. 159-178 (2017).

Oral and Poster Presentation :

(i) アルミニウム合金鋳物の機械的特性に及ぼすカーボン粉末の影響
呉 紹華, 岡安 光博
日本機械学会, 中国四国支部総会・講演会講演論文集, Vol. 54, CD-ROM (松山, 2016).

(ii) 断熱性スリーブによる高品質アルミニウム合金の開発
呉 紹華, 岡安 光博
日本金属学会, 2016年春期講演大会 (東京, 2016).

(iii) The effects of C addition on the mechanical properties of Al-10.6Si-2.5Cu-0.3Mg casting alloys
Shaohua Wu, Mitsuhiro Okayasu
2018 Global Research Efforts on Energy and Nanomaterials (台北, 2018).

(iv) 一方向凝固したADC12合金の組織構造と機械的性質
呉 紹華, 桑田 竜斉, 岡安 光博
日本材料学会, 学術講演会講演論文集, Vol. 68, pp. 211-212 (室蘭, 2019).

- Table of Content -

List of figures

List of tables

Nomenclature

AS: Aspect ratio of eutectic Si phase
ASTM: American society for testing and materials
$\vec{b}$: Burgers vector
b: Fatigue strength exponent
BCC: Body centered cubic
CC: Centrifugal casting
d: Average grain diameter
EBSD: Electron back scattering diffraction
EDX: Energy-dispersive X-ray spectroscopy
FCC: Face centered cubic
FEA: Finite element analysis
G: Shear modulus
GC: Gravity casting
GP: Guinier-Preston
GS: Grain size
HCP: Hexagonal close packed
HMC: Heated mold continuous casting
HPDC: High-pressure die casting
HV: Vickers hardness
IPF: Inverse pole figure
JIS: Japanese industrial standards
k: Strengthening coefficient
MO: Misorientation
N_{f}: Number of cycles to failure for fatigue test
OCC: Ohno continuous casting
r: Size of precipitate
R: Stress ratio in fatigue test
R^2: Correlation rate
RE: Rare earth
S_{a}: Stress amplitude for fatigue test
SEM: Scanning electron microscope
SD: Standard deviation
SDAS: Secondary dendrite arm spacing
STL: Shot time lag
SZ: Size of eutectic Si phase

V : Cooling rate

XRD: X-ray diffraction

α: A correction factor specific to the material

ρ: Dislocation density

ε_f: Fracture tensile strain

σ_0: Materials constant for the resistance of the lattice to dislocation motion

$\sigma_{0.2}$: 0.2% proof strength

σ_e: Fatigue strength (endurance limit)

σ_f: Fatigue strength coefficient

σ_{UTS}: Ultimate tensile strength

σ_{UCS}: Ultimate compressive strength

σ_y: Yield strength

σ_{max}: Maximum stress for fatigue test

τ: Shear stress

τ_0: The intrinsic strength of the material with low dislocation density

λ: Distance between the precipitates

Chapter 1 Fundamental of Casting and Material Strength

1.1 Casting processes
  1.1.1 Gravity casting
  1.1.2 High pressure die casting
  1.1.3 Heated mold continuous casting
  1.1.4 Centrifugal casting

1.2 Casting alloys and die materials
  1.2.1 Aluminum foundry alloys
  1.2.2 Die materials

1.3 High strength mechanisms
  1.3.1 Ductility
  1.3.2 Grain-boundary strength
  1.3.3 Work hardening strength
  1.3.4 Solid solution strength
  1.3.5 Precipitation hardening
  1.3.6 Particle-dispersed reinforcement
References

1.1 Casting process

Casting is one of the manufacturing processes to make various engineering parts. In this process, molten metal is injected into a mold and solidified. Casting has a long history and manufacturing process. The oldest surviving casting is bronze made in Mesopotamia around 3500 BC [1], and iron casting was developed in China around 700 BC. Casting technology has been improved innovatively in Industrial Revolution in 18th century [2].

Because of the technical advantages [3], casting is still used widely in our society:

1) To make complex and thin-walled shapes
2) Excellent recyclability
3) Low production cost
4) High precision shape

Casting is essential manufacturing technology, and with the development of it, our society has evolved. There are various casting technologies in recent years, including gravity casting, pressure casting, centrifugal casting, and continuous casting.

1.1.1 Gravity casting (GC)

Gravity casting is the oldest and fundamental casting method. Figure 1.1 shows a schematic diagram of a general gravity casting method. This casting method is a casting process in which molten metal is poured from the above mold until filling cavity using the forces of gravity. The molds for GC are made of sand and metal base materials. Since the gravity casting does not have any artificial pressure, the casting equipment is formed with a simple structure, i.e., low cost. However, the productivity is disadvantage for the GC process. Even if the fundamental technology of GC, still many automotive parts have been produced, e.g. iron and aluminum alloys.

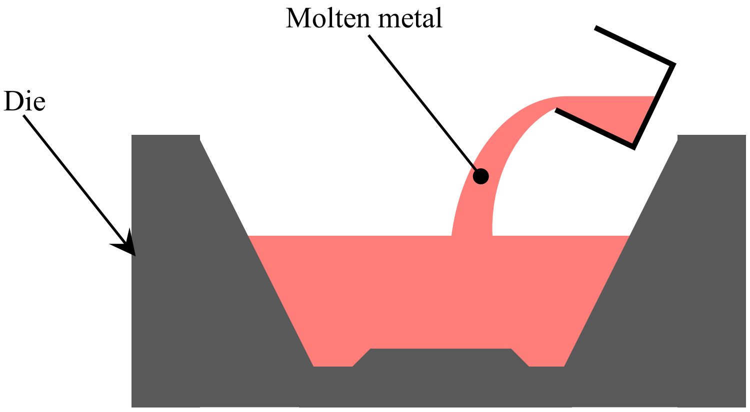

Fig. 1.1 Schematic illustration of the gravity casting.

1.1.2 High-pressure die casting (HPDC)

Like the gravity casting, the high-pressure die casting is used widely in our society, such as automotive and electrical industries. Figure 1.2 shows a schematic diagram of a high-pressure die casting system. This is a casting method in which molten metal, poured into a shot-sleeve, is injected to mold cavity with high pressure and high speed via hydraulic injection system. Because the high temperature melts are employed in this casting process, high toughness of materials for shot-sleeve and mold is needed. Advantages of HPDC are high accuracy of the complicated cast samples, good surface finish, high productivity and low cost for mass production.

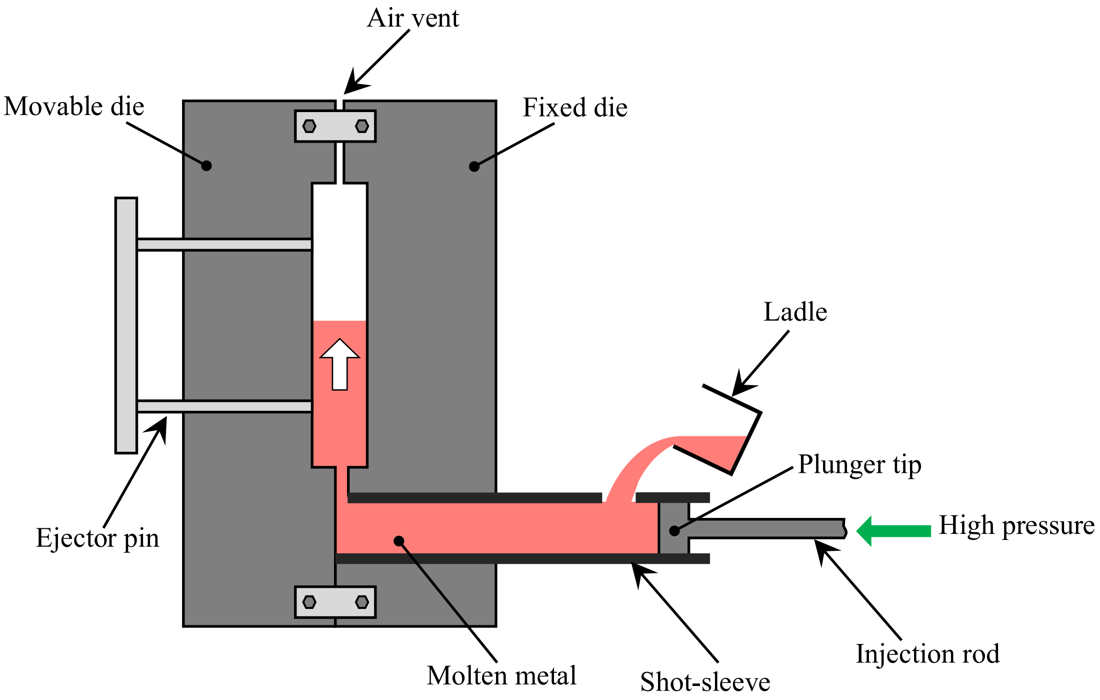

Fig. 1.2 Schematic illustration of the high-pressure die casting.

1.1.3 Heated mold continuous casting (HMC)

A heated mold continuous casting is one of the continuous casting methods, which was developed several decades age [4]. Compared with the conventional continuous casting, as shown in Fig. 1.3(a), the mold heating makes change of solidification process. For conventional continuous casting, the cast material is solidified from the mold surface, resulting in columnar crystals. Due to the spray cooling out of the mold, shown in Fig. 1.3(b), unidirectional solidification occurs for HMC. The size of the cast rod is limited as direct water cooling is conducted and the position of the water cooling device setting to the HMC system is important. Figure 1.4 shows the schematic illustration of heated mold continuous casting system employed in this work.

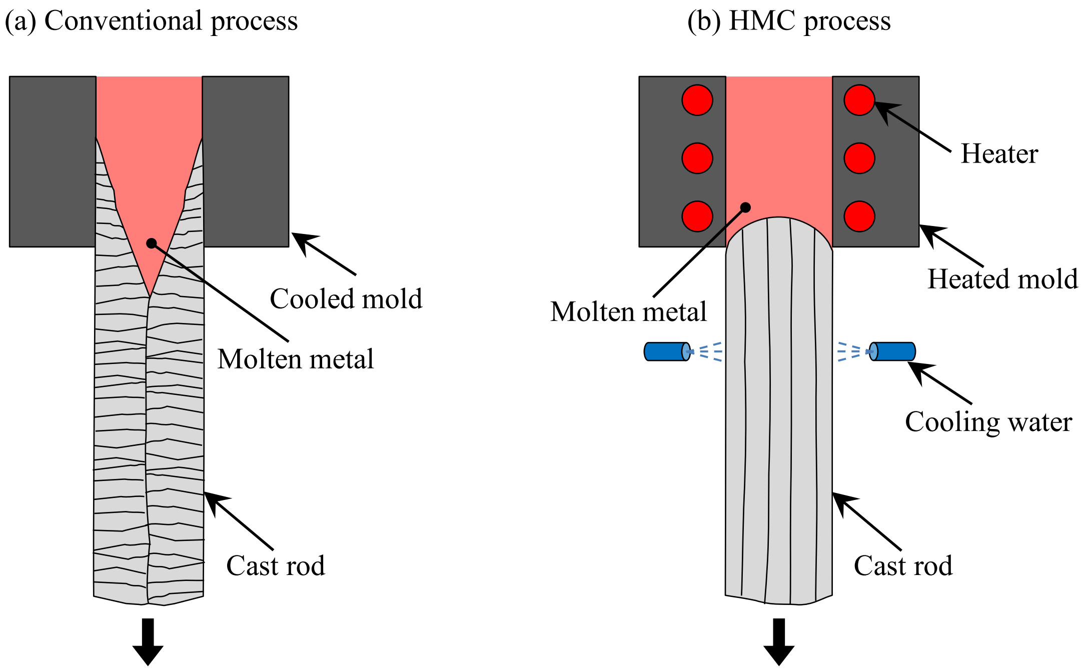

Fig. 1.3 Solidification of cast rod under conventional and heated continuous casting process.

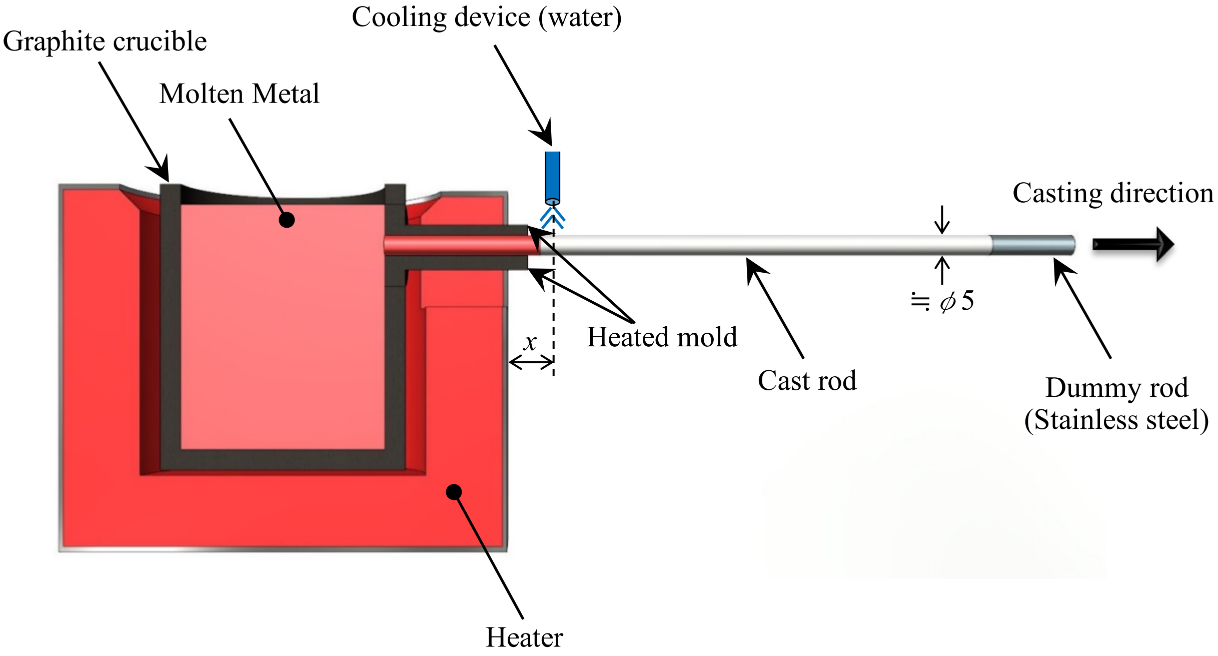

Fig. 1.4 Schematic illustration of the heated mold continuous casting system.

1.1.4 Centrifugal casting (CC)

Centrifugal casting (also called rotating casting) is a casting process under centrifugal force generated by a mold rotating at high speed [5]. Centrifugal casting is used to produce thin-walled cylinders. In this casting, several materials can be employed, such as metals, concrete and plastic. The application of centrifugal casting includes pipes, gears, bearings, etc. [6]. Moreover, centrifugal casting has been used for rolling rolls with multi-layer structures: the outer layer is a hard material with excellent wear resistance and rough skin resistance, and the inner layer is a tough material with excellent breakage resistance [7]. Because the high centrifugal force applies the cast materials during the solidification process, high dense material with less gas defect is creatable. It is also considered that a high quality is attainable by control of crystal and microstructural formation although there is no clear information. To examine the material properties of cast metals made by centrifugal casting, an original casting system was proposed. Figure 1.5 shows a schematic diagram of originally designed centrifugal casting device. In this device, molten metal is poured from the gate setting on the top of the mold. The mold can be rotated at 50 ~ 400 rpm and heated to 600 ℃.

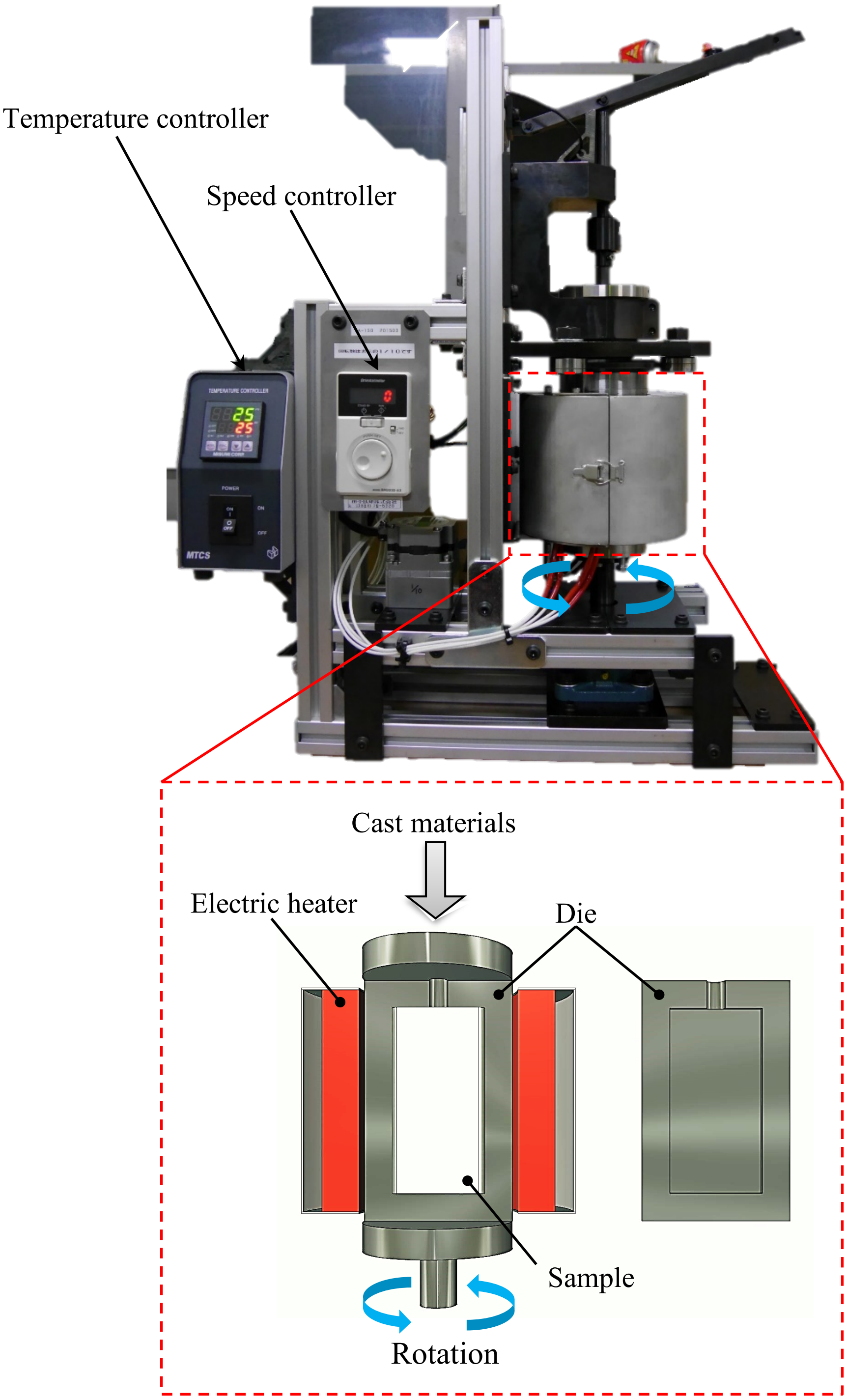

Fig. 1.5 Photograph and schematic illustration of the centrifugal casting.

1.2 Casting alloys and die materials

There are various conventional casting metals in our industries, including iron, aluminum, copper, magnesium, zinc, nickel and titanium alloys. Due to environmental issues of gas emission and global warming, lightweight cast metals have received special attention, in particular, aluminum alloys in addition to high strength steels.

1.2.1 Aluminum foundry alloys

Aluminum has a density of only 2.7 $g \cdot cm^{-3}$, about one-third of steel (7.83 $g \cdot cm^{-3}$), and generally has a face-centered cubic (FCC) crystal structure. Pure aluminum is soft, ductile, corrosion-resistant and highly conductive. With other elements alloying, the aluminum alloy exhibited advantageous properties such as strength, lightness, corrosion resistance, recyclability and formability. It is generally to divide aluminum alloys into two major categories as follows [8]:

(i) Wrought aluminum alloys: originally cast as billets or ingots and then hot or cold-formed into shape by, for example, rolling, extrusion, or forging.
(ii) Cast aluminum alloys: directly cast into ashape in a mold made from primarily sand or steel.

Due to casting is an economical way of producing near-final shaped products with complicated geometries, cast aluminum alloys are wildly used in various industries.

As shown in Table 1.1, cast aluminum alloys are divided into casting (e.g., sand casting, die casting) and die casting in Japanese Industrial Standards (JIS), and they are named C and DC, respectively [9, 10]. Alloying elements are used in order to improve properties such as; casting characteristics and strength. Main alloying elements The significant effects of the main alloying elements are summarized as follows:

- Silicon (Si) increases the castability, i.e., the ability to improve fluidity and readily fill dies. In addition, the eutectic liquid lowers the risk of hot cracking [11].
- Copper (Cu) improves strength and hardness in both as-cast and heat-treated conditions. Copper also improves machinability by increasing the hardness of the matrix [8].
- Magnesium (Mg) improves the strength and hardness after heat treatment by forming $MgSi_2$ precipitates [12].

With the addition of Si and Cu, ADC12 alloy shows good mechanical properties, machinability and castability. Therefore, ADC12 alloy is widely used for various automotive parts, such as engine blocks, transmission cases, and converter housing.

Table 1.1 Representative cast aluminum alloys specified in Japanese Industrial Standards.

Principal alloy compositions	Aluminum alloy	
	Casting	Die casting
Al-Si	AC3A	ADC1
Al-Mg	AC7A	ADC5, ADC6
Al-Cu	AC1A, AC1B	
Al-Si-Cu	AC2A, AC2B, AC4B	ADC10, ADC12
Al-Si-Mg	AC4A, AC4C, AC4CH	ADC3
Al-Si-Mg-Cu	AC4D	ADC14

1.2.2 Die materials

- Pressure casting

Since die materials are heated to high temperature during casting process, Hot-tool steels (SKD61) with high resistance of thermal stress and high wear resistance are used for pressure casting, e. g., gravity casting and high pressure die-casting. Die is usually heat treated by quench and tempered to make high toughness: hardness is about 5 GPa [13]. The issue of die is heat-check, which is rough die surface due to a large number of cracks. In order to solve heat-check, surface treatment of die is effective approach, TiAlN [14, 15]. TiAlN has high hardness of 23 ~ 34 GPa, which coated by 1 ~ 5 μm in thickness [16].

- Continuous casting

In continuous casting, cast materials are continuously produced using the related casting machine, including a dummy rod, die, cooling spray, etc. Molten materials are poured into the die and withdrawn with the dummy rod as the melt solidifies. There are several continuous processes, and currently heated mold continuous casting (HMC) is paid the most attention to make high quality cast samples under controlling the microstructural characteristics. In fact, the HMC process used die heated to about melting point of the cast materials; and the melt is solidified directly by water spray out of die. The die is made of graphite heated by electric heaters. Due to the direct cooling, there is technical limitation to make cast samples: small round or rectangular rod.

1.3 Material properties

As the high reliability of structures and components is required in recent years, an attempt was made to propose the high quality materials by a large number of scientists, such as high strength and high ductility. In particular, improvement of the material properties is needed for cast metals because of various defects and scattered microstructural formations. In basic, the strength and ductility are in the typical trade off relationship, so high strength materials have low ductility. Namely, the definition of material strength is considered to be extent of resistance of plastic deformation. Thus, the deformation characteristics and high strength mechanisms of cast metals are important in this work.

1.3.1 Ductility

There are two types of plastic deformation of metallic materials with a crystal structure: slip deformation and twin deformation. Twin deformation is a phenomenon in which atoms move so that the arrangement of atoms is formed with mirror status, i.e., line symmetry based on twin plan [17, 21]. This deformation occurs in low temperature conditions for FCC and BCC metals. This deformation is formed during crystals growing from the gas phase or liquid phase (growth twins) or when crystals are transformed by quenching (transformation twins). On the other hand, slip deformation is a shear deformation phenomenon that occurs along a slip direction on a slip plane. Table 1.1 shows the possible slip systems for the main metals with FCC, BCC and HCP structures: slip plans and slip direction [17, 18]. Due to the different slip systems and closed-packed planes, the severity of deformability is altered depending on the crystal structures, in which the higher and lower ductility are obtained for FCC and HCP structures, respectively. In the present study, aluminum alloys, magnesium alloys, and steels are mainly used, and the three materials (Al, Mg and Fe) consists of FCC, HCP and BCC structure, respectively.

Table 1.2 Slip systems for FCC, BCC and HCP crystal structures.

Crystal structure	Slip Plan	Slip Direction
FCC	$\{111\}$	$\langle 110 \rangle$
BCC	$\{110\}$	$\langle 111 \rangle$
	$\{112\}$	$\langle 111 \rangle$
	$\{123\}$	$\langle 111 \rangle$
HCP	$\{0001\}$	$\langle 11\bar{2}0 \rangle$
	$\{10\bar{1}0\}$	$\langle 11\bar{2}0 \rangle$
	$\{10\bar{1}1\}$	$\langle 11\bar{2}0 \rangle$

Figure 1.6 shows a schematic diagram of the process of shear deformation. As shear stress (τ) applies to the material (Fig. 1.6(a)), atoms are shifted to the right-hand side. In this case, one extra atomic line is created (Fig. 1.6(b)), which is related to line defect as well as dislocation, when the shear stress is further applied (Fig. 1.6(c)), the dislocation is moved to the slip direction along the slip plane. Eventually, the shape of the material is altered permanently as plastic deformation as shown in Fig. 1.6(d) [19, 20].

As mentioned above, in order to increase the strength of metallic materials, prevent of the slip deformation or high resistance of the slip is indispensable. There are several methods to make high strength materials with controlling the microstructural characteristics.

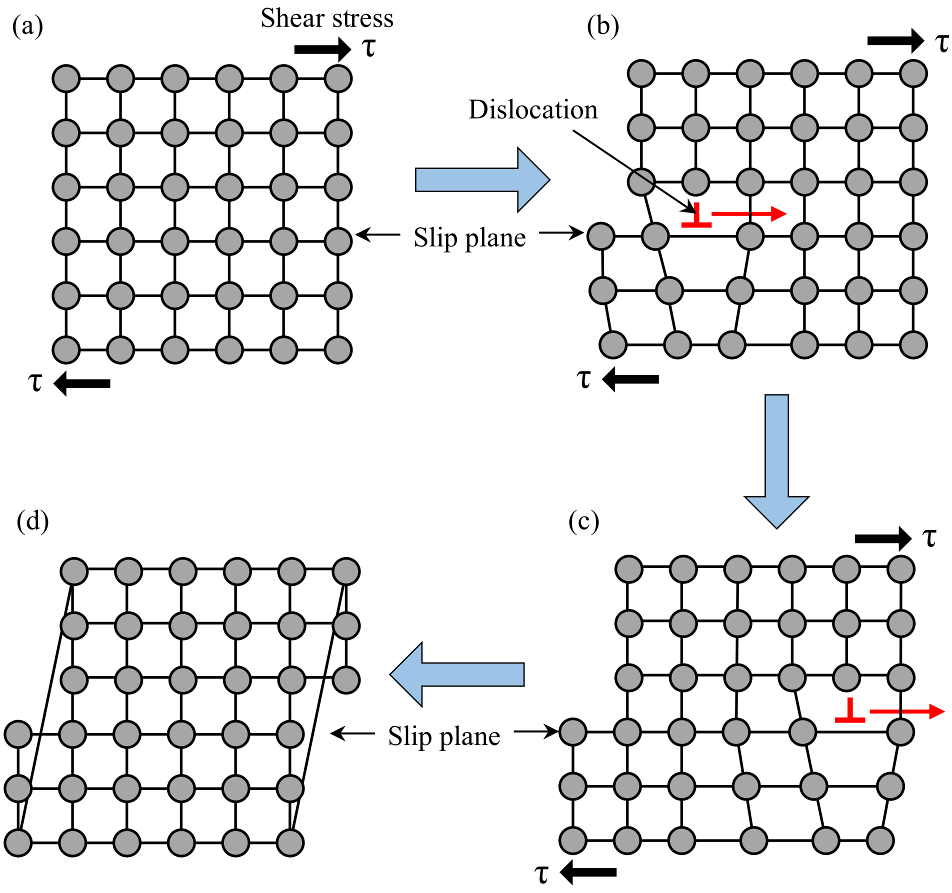

Fig. 1.6 A schematic diagram of the slip deformation.

1.3.2 Grain-boundary strength

The crystal grain size of polycrystalline metals affects mechanical properties. Each grain has crystallographic orientations individually, and a grain boundary is formed between adjacent grains, as displayed in Fig. 1.7. When plastic deformation occurs in Grain A, the dislocation is moved to Grain B. However, the grain boundary has an additional effect on the plastic deformation behavior by serving as an effective barrier to the dislocation movement, The extent of the interruption affects the strength of the materials [21]. Thus, material properties of a fine-grained material are harder and stronger than those of coarse grained ones: the former material has many grain boundaries to block dislocation motion. From Hall and Petch, the yield strength σ_y of polycrystalline material could be given by grain size as Hall-Petch relation:

$$\sigma_y = \sigma_0 + kd^{-1/2} \tag{1.1}$$

where d is the average grain diameter, σ_0 is overall resistance of lattice to dislocation movement, and k is locking parameter of grain boundary [22, 23]. Grain size can be controlled by the solidification and heat treatment process. A rapid cooling process makes the fine grain of polycrystalline materials, which is an effective approach to create high yield strength. However, the yield strength would either remain constant or decrease with decreasing grain size of less than 10 nm, in which the material failure could occur mainly along the grain boundaries. This phenomenon has been termed the inverse Hall-Petch relation.

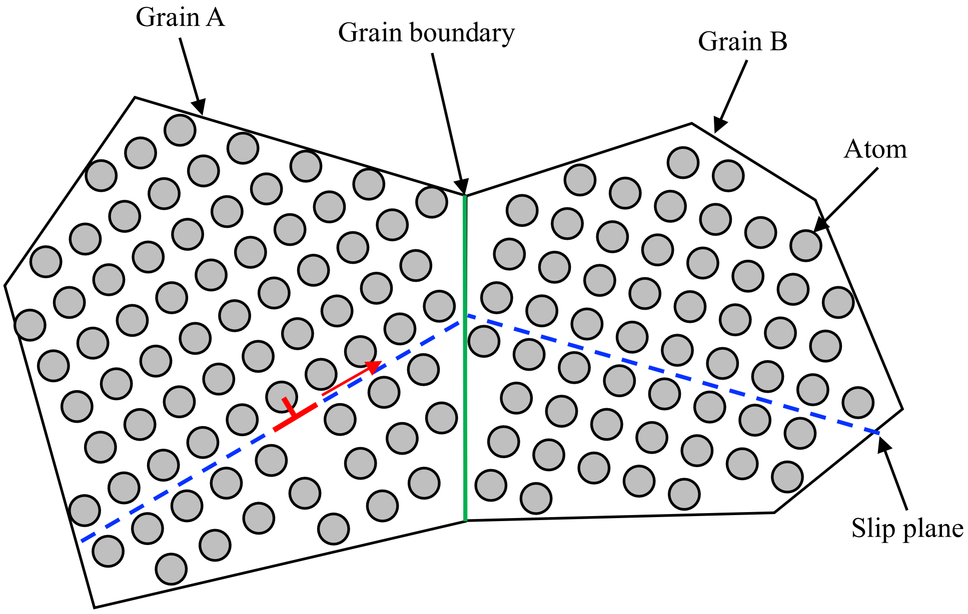

Fig. 1.7 The motion of a dislocation as it encounters a grain boundary.

1.3.3 Work hardening strength

Work hardening is the phenomenon whereby a ductile metal becomes harder and stronger as it is plastically deformed. Work hardening results from a drastic increase in a large number of dislocation-dislocation interactions, reducing dislocation movement. As a result, considerable stress must be applied in order that additional deformation may take place. Most metals underwent work hardening when cold worked at less than half their absolute melting point. Cold worked metals have a high dislocation density ($\geqq 10^9$ cm^{-2}) due to the disordered crystal lattice [24]. Work hardening behavior has been investigated using single crystal materials. The ratio of the work-hardening coefficient to shear modulus is independent of stress and temperature. Dislocation tangles make eventually the formation of dislocation cell structure resulting in the increment of material strength. It may have technical difficulty to measure the heterogeneity of dislocation distribution, but the resolved shear stress (τ) can be approximated using the mean dislocation density (ρ) as follows:

$$\tau = \tau_0 + \alpha G\vec{b}\rho^{1/2} \tag{1.2}$$

where τ_0 is the shear stress needed to move a dislocation and, α is a numerical constant: 0.3 ~ 0.6 for FCC and BCC metals, G is shear modulus and $\vec{b}$ is Burgers vector [17].

1.3.4 Solid solution strength

Solute atoms into solid solution in solvent-atom lattice produces an alloy, which is stronger than the pure metal. There are two types of solid solution: (a) substitutional solid solution and (b) interstitial solid solution. Figure 1.8 shows schematic diagrams of the two solid solution systems. If solute and solvent atoms are similar or larger in size, the solute atoms will occupy lattice points in crystal lattice of the solvent atoms, i.e., substitutional solid solution. If the solute atoms are much smaller than the solvent atoms, they occupy interstitial positions in solvent lattice. Since the solute atoms have different properties, the crystal lattices are strained, which makes interruption of dislocation movement resting in the high strength of the material [25]. For example, the larger and smaller solute atoms occupy substitutional positions in solvent lattices, compressive and tensile strains are created, respectively.

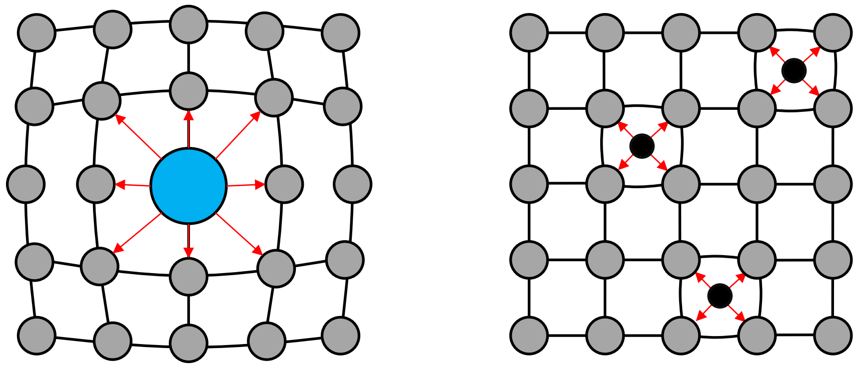
(a) Substitutional solid solution
(b) Interstitial solid solution

Fig. 1.8 Schematic diagrams of (a) substitutional solid solution and (b) interstitial solid solution.

1.3.5 Precipitation hardening

As the supersaturated materials by solid solution is aged, the second phases with different from in the phase are precipitated. Precipitates on a slip plane can promote strengthening by interrupting the motion of dislocations. There are two main mechanism of precipitation hardening, as shown in Fig.1.9: (a) a dislocation cutting a precipitates and (b) dislocation curving around a precipitates. When the precipitates are small and/or soft, dislocations can cut and deform the precipitate (Fig. 1.9(a)). On the other hand, the precipitates are lager and/or hard, dislocations can't cut the precipitates (Fig. 1.9(b)). In the later case, stage (1) shows a straight dislocation line approaching a precipitate. At stage (2), the dislocation line begin to bend, and, at stage (3), the line reach the critical curvature. The forming a loop is Orowan's mechanism. The dislocation can move forward without further decreasing its radius curvature. The energy for dislocation movement is needed to make Orowan loop, which leads to high hardness and high strength. The stress required to move dislocation between the two precipitates is considered to be obtained from the following equation [17]:

$$\tau_0 = G\vec{b} \;/\; \lambda \tag{1.3}$$

where λ is the distance between the precipitates. The Orowan loops created make the dislocation motion more difficult, resulting in increment of hardness and strength [25, 26]. The extent of precipitation shear strength is also depending on the size (radius: r) of the precipitates. Figure 1.10 shows the relationship between the size of precipitate and shear strength for two hardening mechanisms. The strength increase with increasing the size of precipitates for the cutting mode, while the reduction of the strength occurs with increasing the size of precipitates [27, 28].

(a) Cutting through a precipitate

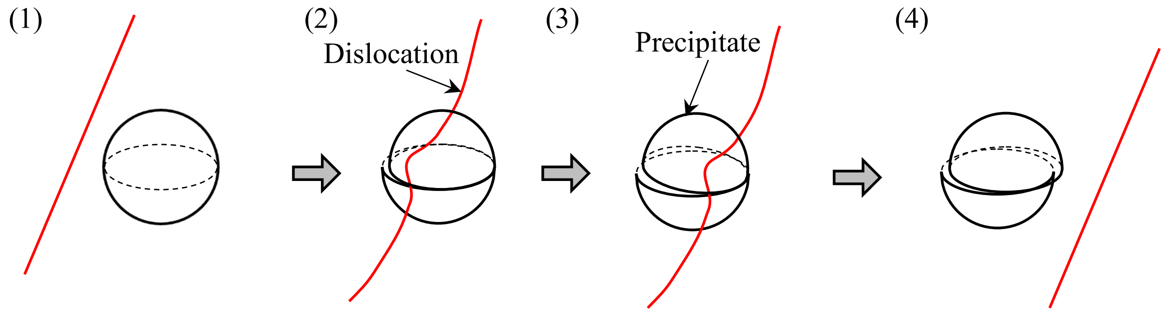

(b) Curving around a precipitate

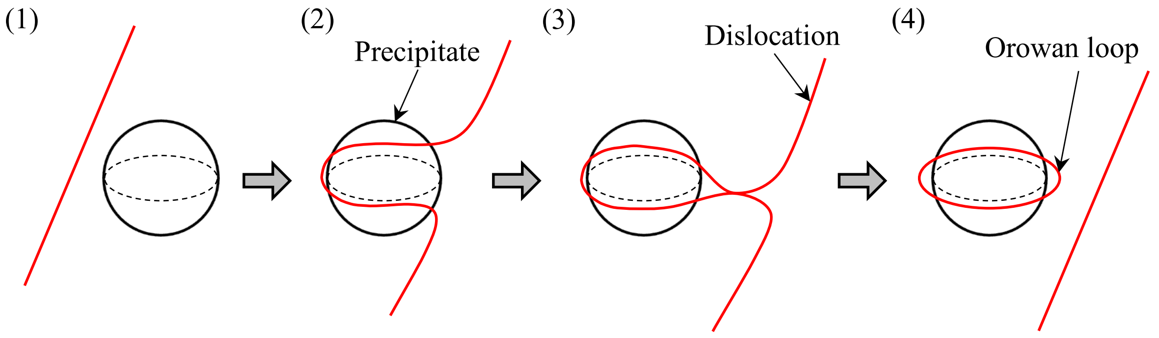

Fig. 1.9 Schematic illustration of precipitation strengthening due to (a) dislocation line cutting of precipitates and (b) dislocation line curve around the precipitate.

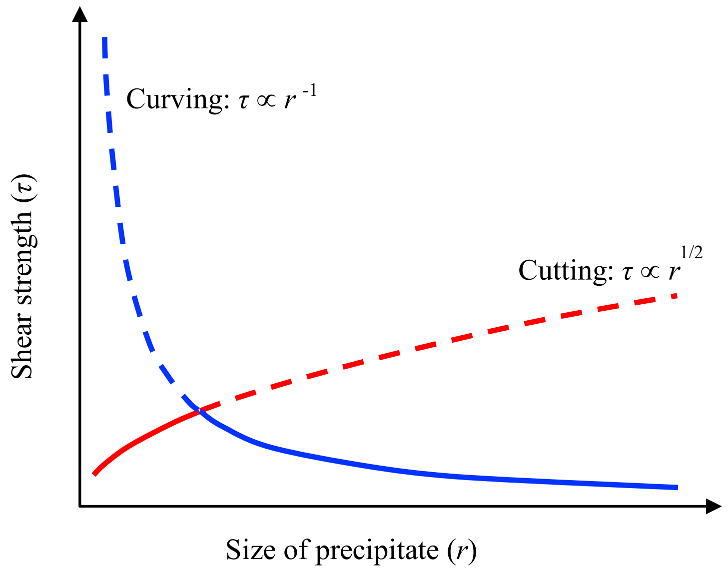

Fig. 1.10 Schematic of the role of precipitation hardening mechanisms.

1.3.6 Particle-dispersed reinforcement

The strengthening mechanism of particle-dispersion reinforcement is the same as precipitation hardening as mentioned in Section 1.3.5, although the manufacturing method is different. Precipitation hardening occurs by the precipitations of the second phase aging process, while particle-dispersion reinforcement is a method, in which hard particles are mired into the melt alloy [17]. For example, ceramic particles of SiC with 0.3 μm in diameter are employed for cast aluminum alloy, e.g., metal matrix composites (MMC) [30]. Such particles are not cut by the dislocation movement. Hence, the Orowan mechanism is only the method of its reinforcement. Furthermore, hard ceramic particles wouldn't decompose or disappear even at high temperatures, so the high quality of the cast samples could be made [25].

References

1. H. Nakae, History of Casting, J. JFS, 85(2013)233-237.
2. H. Kimura, Subject of casting technology and its long term vision, Int. J. Jpn. Soc. Prec. Eng., 76(2010)373-377.
3. M. Ohtaki, T. Soutome, K. Mori, H. Kudoh, S. Tanaka, Development of aluminum recycling process in the national project, Furukawa Electric Review, 104(1999)25-30.
4. 本保元次郎, 加熱鋳型式連続鋳造鋳塊に関する基礎的な研究, 千葉工業大学, (1991)5-8.
5. J.T. Black, R.A. Kohser, DeGarmo's materials and processes in manufacturing, Wiley, (2011)333-335
6. P. Beeley, Foundry technology, Butterworth-Heinemann, (2001)622-645.
7. Y. Sekimoto, Recent rolls for hot rolling mills, Hitachi Hyoron, 56(1974)73-78.
8. J.R. Davis, Alloying: Understanding the Basics, ASM International, (2001)351-387.
9. Japanese Industrial Standards, JIS H 5202, (2010)
10. Japanese Industrial Standards, JIS H 5302, (2006)
11. M.D. Sabatino, L. Arnberg, Castability of aluminium alloys, Trans. Indian Inst. Met., 62 (2009)321-325.
12. A. Bjurenstedt, Imperfections in Recycled Aluminium-Silicon Cast Alloys, Jönköping University, (2015)3-4.
13. S. Yoshitani, Current status and recent trend in die steels (Cold-Work Dies, Semi-Hot and Hot-Work Dies, Plastic Mold Dies), Denki-Seiko, 57(1986)222-235.
14. S. Fujiki, Recent advance in surface harding treatment of dies steel, J. Surf. Finish. Soc. Jpn. 52(2001)535-539.
15. Y. Tamura, T. Okuno, New hot working tool steels for die casting, J. JFS., 62(1991)1002-1014.
16. K. Kawata, Trend of recent surface treatment technology, Denki-Seiko, 76(2005)269-277.
17. A. Sakaida, A. Ueno, K. Isonishi, S. Nishino, N. Horikawa, Strength and fracture of materials, Corona, (2011)25-33.
18. W.D. Callister, D.G. Rethwisch, Materials science and engineering. Wiley, (2010)200-205.
19. D. Hull and D. Bacon, Introduction to dislocations. Butterworth-Heinemann, (2001)42-49.

20. R. Abbaschian, Reed-Hill, Physical metallurgy principles, Cl-Engineering, (2009)82-91.

21. W.D. Callister, D.G. Rethwisch, Fundamentals of materials science and engineering: An integrated approach loose leaf, Wiley, (2015)244-263.

22. E.O. Hall, The deformation and ageing of mild steel: III Discussion of results, Proc. Phys. Soc., B64(1951)747-753.

23. N.J. Petch, The cleavage strength of polycrystals, J. Iron Steel Inst., 174(1953)25-28.

24. G.K. Williamson, R.E. Smallman, Dislocation densities in some annealed and cold-worked metals from measurements on the X-ray debye-scherrer spectrum, The Philosophical Magazine: A Journal of Theoretical Experimental and Applied Physics, 1(1956)34-46.

25. W. Soboyejo, Mechanical properties of engineered materials, CRC Press, (2002)223-246.

26. J. Pelleg, Mechanical properties of materials, Springer Science & Business Media, (2012)246-256

27. 牧 正志, 鉄鋼の組織制御: その原理と方法, 内田老鶴圃, (2005)115-116.

28. A.J. Ardell, Precipitation harding, Metall. Mater. Trans., 16A(1985)2131-2165.

29. R.W. Hertzberg, R.P. Vinci, J.L. Hertzberg, Deformation and fracture mechanics of engineering materials, Wiley, (1996)167-170.

30. H. Morimoto, H. Iwamura, M. Abe, Y. Ashida, Strengthening of SiC particulate reinforced aluminum composites due to refinement of particles, J. Jpn. Inst. Metals, 58(1994)973-979.

Chapter 2 Introduction

2.1 Overview

In recent years, due to global warming, which is one of the environmental problems, it is required to reduce greenhouse gas emissions such as CO_2. Therefore, especially in the rapidly growing automobile industry, fuel efficiency improvement is needed to reduce CO_2 [1]. In response to this, research and development to further reduce the weight of the vehicle body to improve fuel efficiency are vigorously carried out worldwide.

An automobile consists of various materials, including 70% ferrous alloys, 8% lightweight resin, 7% aluminum alloys, etc. [2]. Evidently, ferrous alloys are the main component at present, and it is conceivable that the weight of automobiles will be reduced by using lighter materials. Therefore, expectations are rising for aluminum alloys and composite materials (CFRP), which are light metal materials, as alternatives to ferrous alloys. Although CFRP has an excellent specific strength, it has not yet been put into practical use due to its high cost and poor recyclability. Therefore, aluminum alloys, which are lightweight and have excellent recyclability, are attracting attention as alternative materials instead of ferrous alloys.

As described in Chapter 1, the casting process has a number of technical advantages for the manufacture of metal components with complicated geometries at high productivity levels. Most automotive parts made from aluminum alloys are manufactured by gravity casting and a high-pressure die casting process. Cast aluminum alloys are widely used in the automotive industry for components such as transmission cases, converter housings, wheels and cylinder blocks [3]. However, their range of applications is still limited by their mechanical properties, which are significantly lower than those of ferrous foundry alloys [4]. In addition, due to coarsened grains and cast defects (e.g., porosity, inclusions, and cold flakes), which occurred during the casting process, the strength is not yet satisfactory. Therefore, to expand the range of cast aluminum and magnesium alloys on the automobile, it is necessary to improve their material properties.

So far, many studies have been conducted on the material properties of cast aluminum and magnesium alloys. Zhao et al.[5] have investigated the effects of porosity and serrated faces on the tensile properties of ADC12 die-cast plate samples. It has been reported by Jana et al. [6] that fatigue cracks in cast aluminum alloy originate from the edges of porosities because of the high-stress concentration. Mechanical properties are also affected by microstructural characteristics, such as α-Al grains and eutectic phases. Many researchers have found that secondary dendrite arm spacing (SDAS) is an influential factor determining the mechanical properties of cast aluminum alloys. The smaller SDAS can be leading to better mechanical properties, i.e., grain refinement strengthening. It is also considered that high mechanical properties could be obtained in the aluminum alloys with smaller SDAS due to the decrement of porosity [7]. Youssef et al. [8] synthesized a bulk nanocrystalline Al-Mg alloy (Al-5083 alloy), which possessed excellent strength with good ductility. Good mechanical properties are attained in cast aluminum alloys by α-Al grain refinement, i.e., a sub micrometer grain size is a significant advantage [9]. However, for most metals, tiny grains (10 nm) result in more inferior mechanical properties because of an incapacity to support the dislocation pileups [10]. Furthermore, the effect of eutectic structure (size and shape) on mechanical properties has been examined for cast aluminum alloys, and it appears that large and elongated eutectic particles (Fe-based phase) result in lower mechanical strength [11]. The crack propagation rate in Al-Si-Mg alloy varies because of the agglomerated Si particles in the eutectic region; moreover, cracks in the α-Al grains propagate rapidly compared to cracks growing in the eutectic and grain boundaries [12]. Impressive work has been carried out by Wang [13], where the tensile properties and fracture characteristics of cast aluminum alloys are dependent on not only SDAS but also the size and shape of eutectic Si particles and Fe-rich intermetallic. Wang [14] has also reported the plastic deformation behavior of the cast aluminum alloys: at low strain region, the aspect ratio of the eutectic particles and matrix strength is attributed to the work hardening, whereas at large strain region, the hardening rate depends on SDAS.

It is considered that high quality casting alloy would be obtained by reducing the above casting defects. Cold flakes, one of the cast defects peculiar to the cold-chamber die casting process, are among the critical defects responsible for cast products' low strength and low-pressure resistance. In general, it is said that the cold flakes generated as follows: rapidly solidified melt on an inner surface of a shot-sleeve is injected into the mold cavity, where it breaks into small pieces and becomes mixed into the cast sample as defects [15]. Because of the low boundary strength between the two different structure, resulting in poor material properties for the cast product [15]. A numerical analysis was performed to clarify the creation of cold flakes during the injection process [16]. Furthermore, Lee et al. [17] have examined Al-4.7Mg-0.7Mn (A5083) solidification characteristics numerically and have discussed the influence of casting pressure and cooling rate on macro segregation. It has been reported that the appearance of cold flakes in die-cast components makes them predisposed to break, resulting in tensile strength of less than 30% of that for the components without defects [18]. The injection system is one of the most important factors to be considered when attempting to reduce the incidence of cold flakes [19]. In cold-chamber die casting, a powder lubricant can be sprayed onto the inner shot-sleeve surface to provide an insulating effect, thereby inhibiting the production of cold flakes and leading to improved mechanical properties [20]. However, due to the health risks of casting workers, powder lubricants are seldom employed. Alternatively, ceramic shot sleeves make excellent heat retention and low injection resistance, but the price of ceramic sleeves is very high. Due to the above reasons, the shot-sleeve system needs to be further improved.

The solidification process is also one of the crucial methods to improve the quality of castings. In recent years, attention has focused on unidirectional solidification via continuous casting. As introduced in Section 1.1.3, continuous casting is a process that involves pouring molten metal into a hollow mold. Ohno has proposed the continuous casting process using a heated hollow mold to control the microstructure and crystal orientation (OCC) [21]. The mold temperature is set to a temperature slightly higher than the solidification temperature of the cast metal. The OCC process has also been reported to produce castings with an infinite length directional structure without internal defects [22]. Following the OCC process, our research group has attempted to produce high-quality cast aluminum alloys using heated mold continuous casting (HMC). With the HMC process, the molten alloy solidifies unidirectionally at a high cooling rate. As a result, HMC samples are formed with refined grains, uniformly organized crystal orientation, and few cast defects, resulting in excellent mechanical properties such as high strength and high ductility [23]. However, the process suffers from a technical limitation: the HMC sample can only be made in a relatively simple shape, a thin round bar of 5 mm in diameter. Therefore, further research is needed for the practical application of this technology. Furthermore, although the HMC process can produce high-strength cast aluminum alloys, it is still inferior to ferrous foundry alloys. Therefore, it is necessary to increase further the strength of the cast aluminum alloys.

Heat treatment (T6), i.e., precipitation hardening, is an important method to increase the strength of aluminum alloy. Cast aluminum alloys are primarily based upon Al-Si-Cu alloy, which possesses excellent castability and good mechanical properties. Al-Si-Cu alloy could have the capacity to respond to age hardening with the addition of Mg [24] because of the formation of θ (Al_2Cu) and β (Mg_2Si) phases. Lumley et al. [24] investigated the effects of rapid heat treatment on high-pressure die cast aluminum alloy mechanical properties. They found that high tensile properties could be obtained: the 0.2% proof strength of the heat treated alloy exceeded 300 MPa. Such excellent tensile properties are attributed to precipitation hardening of the complicated Q' phase in the alloy for Mg content greater than 0.2% [24]. Several investigators have examined the mechanical properties of cast aluminum alloys following T6 treatment. High-quality die casting aluminum alloy with high strength has been produced from Al-Si alloy containing Cu and Mg by appropriate heat treatment resulting in precipitation hardening of Al_2Cu and Mg_2Si intermediate phases [25, 26]. During the aging of aluminum alloys, the precipitation sequences go through several intermediate stages before forming equilibrium precipitates. In Al-Si-Cu-Mg alloys, the precipitation sequences generally arising from the solid solution are as follows: Guinier-Preston (GP) zones-$\theta'' \rightarrow$ -$\theta' \rightarrow$ -θ (Al_2Cu, equilibrium) and GP zones-$\beta'' \rightarrow$ -$\beta' \rightarrow$ -β (Mg_2Si, equilibrium) [27]. The high tensile strength and high ductility obtained for A356 cast aluminum alloys (Al-Si-Mg base alloy) are due to spheroidization of Si particles arising from the T6 treatment and a consequent reduction of the stress concentration on Si eutectic and matrix interfaces [28, 29]. The high tensile properties also could be attributed to the presence of precipitated spherical GP zones with enrichment of Mg and Si, i.e., β' (Mg_2Si) [30]. Similar microstructural characteristics in 319 alloys (Al-8Si-3.3Cu-0.3Mg) after T6 treatment are reported in Ref. [31]. Li et al. [32] have examined that there are double aging peaks in the age-hardening curves of Al-Si-Cu-Mg alloys, and the first peak is higher than the second when the aging is carried out above a specific temperature. The first peak is related to the high-density GP zone, and the second is affected by the metastable phases. Although some researchers have investigated age-hardening characteristics to obtain high mechanical properties for aluminum alloys [26, 32], the associated experimental data are insufficient to determine suitable aging conditions. It is because the heat treatment conditions in previous studies were performed at limited aging temperatures and times. In addition, the main mechanical property previously investigated was the hardness of the material, so there may still be a lack of experimental data to clearly understand the effect of age hardening on mechanical properties.

As mentioned above, the size and shape of the eutectic structure significantly influence the mechanical properties of the aluminum alloy. Rare earth (RE) metals are utilized to create fine eutectic structures in aluminum alloys. The mechanism responsible for modifying eutectic Si in Al-Si alloys has been the subject of scientific research for an extended period [33]. The beneficial effect of adding RE metal (Na) to Al-Si alloys was reported about 100 years ago by Pacz [34]. The addition of minor Sc and Zr to aluminum alloy results in high mechanical properties because of fine-grain strengthening [35]. With the Sb addition to Al-Si alloys, the hardness of the sample increased, and Si particle spacing refinement and Al solid solution strength occur. In another case, the addition of Sr to Al-Si alloys results in well dispersed and rounded porosity in cast samples [36]. Hideo et al. [37] have created an Al-Si alloy with the addition of Na, P, Sr, Sb, B and La, through the unidirectional solidification method. The addition of the RE element could modify the microstructural formation, and the change in the Si phase at the solid/liquid interface caused by the addition of the RE elements has been observed. The microstructural characteristics of Al-21Si alloys with different RE values have also been investigated [38]. In the study of Farahany et al., the interaction between Sb and Sr in an ADC12 die casting alloy was examined through computer-aided cooling curve thermal analysis. In their study, Sb reduced the efficiency of Sr in modifying eutectic Si, and the threshold Sr/Sb ratio exceeded approximately 0.5 to obtain a fully modified structure [39]. Combinative addition of La and B elements has been conducted to allow for grain refinement of Al-Si alloys, in which high material ductility of Al-Si alloys was obtained with the addition of La content [40]. Although several researchers have employed RE metals in aluminum alloys to refine the eutectic structure, there is an apparent lack of information on their mechanical properties. In addition, there is no clear approach to create the cast aluminum alloys with RE metals additional by the HMC process.

2.2 Objective

From the above literature survey, it is considered that the control of the microstructure is significantly essential to improve the mechanical properties of aluminum alloys. The researchers have significantly improved the mechanical properties of aluminum alloys by controlling the microstructure with various means such as improvement of the thermal insulation of shot-sleeves, development of unidirectional casting process, and optimization of heat treatment conditions, .etc. However, the mechanical properties of these cast alloys are still incomparable to ferrous foundry alloys. The σ_{UTS} of ferrous foundry alloy is about 400 ~ 700 MPa, while the cast aluminum alloys is about 300 MPa [23]. Therefore, it is imminent to increase the strength of the cast aluminum alloys to reduce the weight of automobile vehicles.

The insufficient of the previous researches mentioned in Section 2.1 can be concluded as follows:

(i) It is challenging to apply the unidirectional casting process to the manufacturing industry because of the limitation of the size as well as shape of cast samples.

(ii) Insufficient understanding of the precipitation hardening mechanism due to the few heat treatment conditions.

(iii) There is a deficiency in the evaluation of mechanical properties (e.g., fatigue properties).

(iv) Only basic research on the HMC process has been carried out, and further studies on increasing the strength of castings are insufficient.

(v) Thermal insulation is low level for conventional shot-sleeve.

Based on the above information, this thesis designed the experiment the intends to pursue three main objectives. The first objective is to elucidate the solidification process of a large cast sample created by the unidirectional casting process. This study aims to clarify the effect of cooling speed and direction on the microstructure of the casting samples. Secondly, to develop a high-strength casting alloy based on the HMC process. In this approach, high-strength cast aluminum alloys are created by microstructure control according to the heat treatment and elements added. The microstructural and mechanical properties of the developed samples are investigated. Finally, to reduce casting defects in cold-chamber die casting, a newly shot-sleeve with safety and low cost is developed.

2.3 Structure of the thesis document

The rest of the thesis is organized as follows:

- Chapter 3, *Material properties of unidirectionally solidified cast Al-Si-Cu alloy*, introduces a newly developed unidirectional casting process to attempt a larger cast sample and reveal solidification characteristics of Al-Si-Cu alloy. The results of investigating material properties and mechanical properties are explained and discuss the effects of casting conditions (cooling rate, cooling direction) on the microstructure and mechanical properties.
- Chapter 4, *Effects of artificial aging on mechanical properties of Al-Si-Cu foundry alloy*, discusses the effects of artificial aging on the mechanical properties of Al-Si-Cu foundry alloy. The mechanical properties and microstructure of the cast sample aged under various temperature conditions are investigated, and the optimum aging treatment conditions are clarified.
- Chapter 5, *Effects of Sb, Sr and Bi on the material properties of Al-Si-Cu foundry alloy*, discusses the effects of RE (Sb, Sr, and Bi) on the material properties of Al-Si-Cu foundry alloy. Appropriate amounts of RE elements are added to the casting process. The effects of the above

additional elements on the microstructural are elucidated through microstructure observation and mechanical tests.

- Chapter 6, *New high pressure diecast shot-sleeves for creation of high-quality cast aluminum alloy*, investigates the thermal conductivity of the newly developed shot-sleeve for die casting, and the effect is verified by investigating the mechanical properties of the prepared casting sample.
- Chapter 7, *Conclusions*, provides a brief review of Chapters 3 through 6 and presents the achievement in this study.

References

1. S. Shibata, Approach to automotive weight reduction, Tetsu-to-Hagané, 78(1992)1512-1516.

2. Y. Maki, Current status and future trend of automotive ferrous materials, Denki-seiko, 70(1999)5-15.

3. T. Ito, H. Shirai, Magnesium diecast alloys and application for automobile parts, J. Jpn. Inst. Light Met., 42(1992)707-719.

4. T. Chikada, Aluminum application in automobile: Present and future prospects, J. Jpn. Inst. Light Met., 38(1988)118-125.

5. H.D. Zhao, F. Wang, Y.Y. Li, W. Xia, Experimental and numerical analysis of gas entrapment defects in plate ADC12 die castings, J. Mater. Process. Technol., 209(2009)4537-4542.

6. S. Jana, R.S. Mishra, J.B. Baumann, G. Grant, Effect of friction stir processing on fatigue behavior of an investment cast Al-7Si-0.6 Mg alloy, Acta Mater., 58(2010)989-1003.

7. M.S. Kabir, E.A. Ashrafi, T.I. Minhaj, M.M. Islam, Effect of foundry variables on the casting quality of as-cast LM25 aluminum alloy, Int. J. Eng. Adv. Technol., 3(2014)115-120.

8. K.M. Youssef, R.O. Scattergood, K.L. Murty, C.C. Koch, Nanocrystalline Al-Mg alloy with ultrahigh strength and good ductility, Scripta Mater., 54(2006)251-256.

9. Z. Horita, T. Fujinami, M. Nemoto, T.G. Langdon, Equal-channel angular pressing of commercial aluminum alloys: grain refinement, thermal stability and tensile properties, Metall. Mater. Trans. A, 31A(2000)691-701.

10. C.E. Carlton, P.J. Ferreira, What is behind the inverse Hall-Petch effect in nanocrystalline materials?, Acta Mater., 55(2007)3749-3756.

11. Q.G. Wang, D. Apelian, D.A. Lados, Fatigue behavior of A356/357 aluminum cast alloys. Part II-Effect of microstructural constituents, J. Light Met., 1(2001)85-97.

12. M. Kobayashi, H. Hara, H. Toda, D. Sugiyama, N. Kuroda, Fatigue behaviour of hot worked cast aluminum alloys with different Si contents, Int. J. Cast Met. Res., 25(2012)31-37.

13. Q.G. Wang, Microstructural effects on the tensile and fracture behavior of aluminum casting alloys A356/357, Metall. Mater. Trans. A, 34A(2003)2887-2899.

14. Q.G. Wang, Plastic deformation behavior of aluminum casting alloys A356/357, Metall. Mater. Trans. A, 35A(2004)2707-2718.

15. H. Kato, T. Suzuki, Y. Annou, K. Kageyama, Nondestructive detection of cold flakes in aluminum alloy die-cast plate with ultrasonic measurement, Mater. Trans., 45(2004)2403-2409.

16. R . Helenius, O. Lohne, L. Arnberg, H.I. Laukli, The heat transfer during filling of a high-pressure die-casting shot sleeve. Mater. Sci. Eng. A, 413-414(2005)52-55.

17. J.H. Lee, H.S. Kim, C.W. Won, et al., Effect of the gap distance on the cooling behavior and the microstructure of indirect squeeze cast and gravity die cast 5083 wrought Al alloy, Mater. Sci. Eng. A, 338(2002)182-190.

18. H. Iwahori, K. Tozawa, T. Asano, Y. Yamamoto, M. Nakamura, M. Hashimoto, S. Uenishi, Properties of scattered structures included in aluminum die castings, J. Jpn. Inst. Light Met., 34(1984)525-530.

19. G.O. Verran, R.P.K. Mendes, M.A. Rossi, Influence of injection parameters on defects formation in die casting Al12Si1,3Cu alloy: Experimental results and numeric simulation, J. Mater. Proc. Technol., 179(2006)190-195.

20. S. Aoyama, M. Tashiro, K. Sakamoto, T. Umemura, Quality improvement of aluminum alloy die castings by powder lubricant for shot sleeve, Jpn. Foundry Eng. Soc., 64(1992)684-692.

21. A. Ohno, Solidification, 1st ed. Springer, Germany, (1987)113-118.

22. Z.M. Zhang, T. Lu, G.J. Xu, X.F. Guo, Microstructure of binary Mg-Al eutectic alloy wires produced by the Ohno continuous casting process, Acta Metall. Sin., 21(2008)275-281.

23. M. Okayasu, K. Ota, S. Takeuchi, H. Ohfuji, T. Shiraishi, Influence of microstructural characteristics on mechanical properties of ADC12 aluminum alloy, Mater. Sci. Eng. A, 592(2014)189-200.

24. R.N. Lumley, I.J. Polmear, P.R. Curtis, Rapid Heat Treatment of Aluminum High Pressure Diecastings, Metall. Mater. Trans. A, 40A(2009)1716-1726.

25. O.S. Es-Said, D. Lee, W.D. Pfost, D.L. Thompson, M. Patterson, J. Foyos, R. Marloth, Alternative heat treatments for A357-T6 aluminum alloy, Eng. Fail. Anal., 9(2002)99-107.

26. M. Furui, T. Kitamura, T. Ishikawa, S. Ikeno, S. Saikawa, N. Sakai, Evaluation of age hardening behavior using composite rule and microstructure observation in Al-Si-Mg alloy castings, Mater. Trans., 52(2011)1163-1167.

27. F.J. Tavitas-Medrano, A.M.A. Mohamed, J.E. Gruzleski, F.H. Samuel, H.W. Doty, Precipitation-hardening in cast AL-Si-Cu-Mg alloys, J. Mater. Sci., 45(2010)641-651.

28. Y. Bai, H. Zhao, Tensile properties and fracture behavior of partial squeeze added slow shot die-cast A356 aluminum alloy, Mater. Des., 31(2010)4237-4243.

29. J. Peng, J. Tang, J. He, D. Xu, Effect of heat treatment on microstructure and tensile properties of A356 alloys, Trans. Nonferr. Met. Soc. China, 21(2011)1950-1956.

30. E. Sjölander, S. Seifeddine, The heat treatment of Al-Si-Cu-Mg casting alloys, J. Mater. Process. Technol., 210(2010)1249-1259.

31. K.A. Ragab, A.M. Samuel, A.M.A. Al-Ahmari, F.H. Samuel, H.W. Doty, Influence of fluidized sand bed heat treatment on the performance of Al-Si cast alloys, Mater. Des., 32(2011)1177-1193.

32. R. Li, R. Li, Y. Zhao, L. He, C. Li, H. Guan, Z. Hu, Age-hardening behavior of cast Al-Si base alloy, Mater. Lett., 58(2004)2096-2101.

33. M. Zarif, B. Mckay, P. Schumacher, Study of heterogeneous nucleation of eutectic Si in high-purity Al-Si alloys with Sr addition, Matell. Mater. Trans. A, 42A(2011)1684-1691.

34. A. Pacz, Alloy, U.S. Patent No.1, 387900A(1921)1-3.

35. Z. Yin, Q. Pan, Y. Zhang and F. Jiang, Effect of minor Sc and Zr on the microstructure and mechanical properties of Al-Mg based alloys, Mater. Sci. Eng. A, 280(2000)151-155.

36. C.M. Dinnis, M.O. Otte, A.K. Dahle, J.A. Taylor, The influence of strontium on porosity formation in Al-Si alloys, Metall. Mater. Trans. A, 35(2004)3531-3541.

37. H. Nalae, K. Song, H. Fujii, New application of unidirectional solidification method for observation of interfacial morphology, Mater. Trans. JIM, 33(1992)1051-1056.

38. J. Chang, I. Moon, C. Choi, Refinement of cast microstructure of hypereutectic Al-Si alloys through the addition of rare earth metals, J. Mater. Sci., 33(1998)5015-5023.

39. S. Farahany, M. H. Idris, A. Ourdjini, Evaluations of antimony and strontium interaction in an Al-Si-Cu-Zn die cast alloy, Therm. Acta, 584(2014)72-78.

40. Y. Chen, Y. Pan, T. Lu, S. Tao, J. Wu, Effects of combinative addition of lanthanum and boron on grain refinement of Al-Si casting alloys, Mater. Des., 64(2014)423-426.

41. M. Yamasaki, K. Hashimoto, K. Hagihara, Y. Kawamura, Effect of multimodal microstructure evolution on mechanical properties of Mg-Zn-Y extruded alloy, Acta Mater., 59(2011)3646-3658.

42. M. Matsuda, S. Ando, M. Nishida, Dislocation structure in rapidly solidified $Mg_{97}Zn_1Y_2$ alloy with long period stacking order phase, Mater. Trans., 46(2005)361-363.

43. A. Datta, U.V. Waghmare, U. Ramamurty, Structure and stacking faults in layered Mg-Zn-Y alloys: a first-principles study, Acta Mater., 56(2008)2531-2539.

44. K. Hagihara, N. Yokotani, Y. Umakoshi, Plastic deformation behavior of $Mg_{12}YZn$ with 18R long-period stacking ordered structure, Intermetallics, 18(2010)267-276.

Chapter 3 Material properties of unidirectionally solidified cast Al-Si-Cu alloy

3.1 Experimental procedures

The microstructural characteristics and mechanical properties of the Al-10.5Si-3Cu cast aluminum alloy, ADC12, were examined. Note that ADC12 is a JIS (Japanese Industrial Standards) die casting alloy that is similar to the ASTM (American society for testing and materials) standards alloy, A383. The cast ADC12 alloy has been used in various automotive parts, including the engine block, transmission case, and wheels. The chemical composition of the ADC12 alloy are presented in Table 3.1. Figure 3.1 shows a schematic diagram of the casting arrangement. A cast mold was designed and consisted of three separated parts, which made the handling of the cast sample simpler. The cast mold was made of SKD61 steel (AISI H13), and the mold surface was coated with TiAlN, providing high resistance to heat and corrosion. The ADC12 melt was poured into the mold (ϕ20 mm × 100 mm), as shown in Fig. 3.1(a), and the melt was solidified from the bottom of the mold, where the cast cavity was connected to a basin of molten metal via a thin spiraled hole. This mold system was designed for the creation of single-crystal metals via unidirectional solidification (Fig. 3.1(b)), which is explained in detail in a previous study [1]. For the solidification process, the mold was set in an electret furnace, and then heated to above 590 °C (the liquidus temperature for ADC12 was 587 °C). When the temperature of the mold was stable, the ADC12 melt, at 700 °C, was poured into the mold. Water cooling was conducted after one hour. The furnace temperature was set at 10 $°C{\cdot}h^{-1}$ after water cooling until reaching the solidus temperature for ADC12, 577 °C. To understand the thermal properties of the cast mold, the temperature profiles of the mold at three different points were measured. Figure 3.2 shows the temperature profiles of the cast mold. It appeared that the mold temperature varied depending on the measurement point: the temperature at the upper point was higher than that for the center and lower points. As the ADC12 melt was poured to the mold, the mold temperature increased for a period of time before becoming stable. Note that cast defects, such as porosity and inclusions, were not detected in our cast sample.

Table 3.1 Chemical composition of ADC12 (mass%).

Si	Cu	Fe	Zn	Mg	Mn	Ni	Al
10.99	1.89	0.82	0.82	0.24	0.19	0.06	Bal.

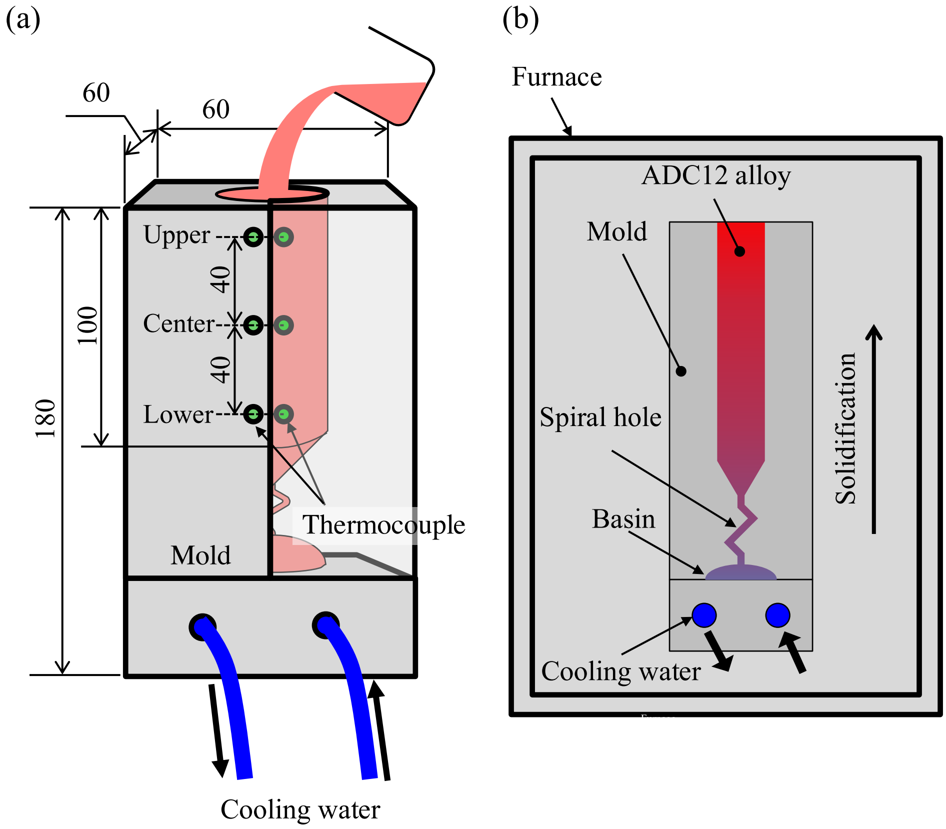

Fig. 3.1 A schematic illustration of the unidirectional casting arrangement: (a) the pouring process and (b) the solidification process.

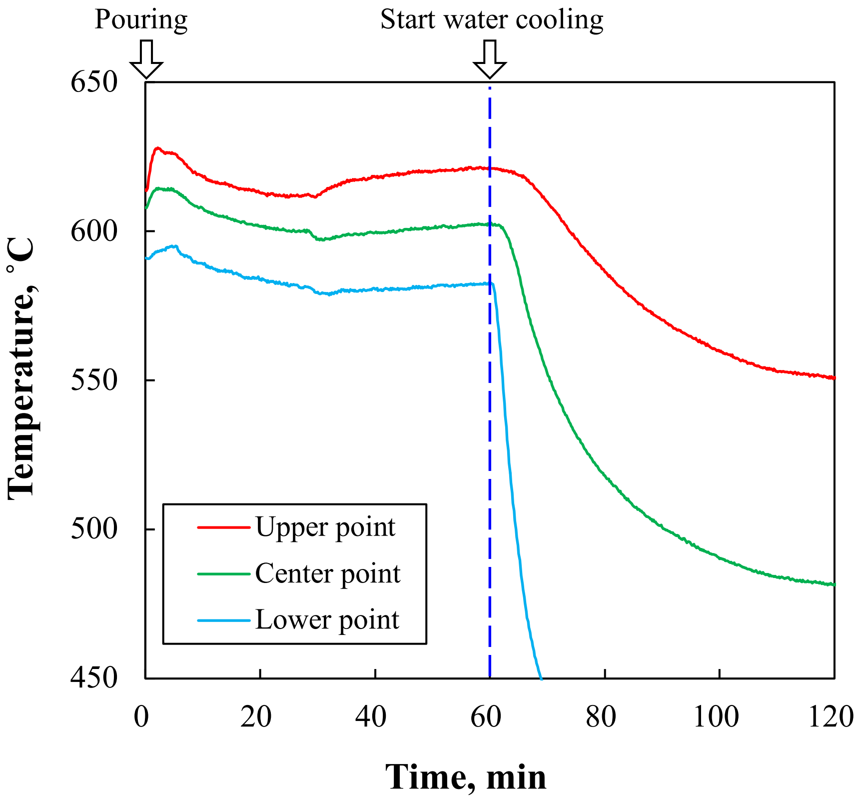

Fig. 3.2 The temperature profiles of the cast mold.

Fig. 3.3(a) shows a schematic diagram of the test specimen, which was shaped like a rectangular dumbbell with dimensions of 30 × 4 × 1 mm. The test specimen was obtained from the upper and lower regions of the cast sample, as shown in Fig. 3.3(b). A tensile test was conducted using a screw-driven universal testing machine with a 50 kN capacity. The tensile properties were evaluated via a tensile stress versus strain curve, which was monitored using a data acquisition system in conjunction with a computer through a standard load cell and strain gage. The tensile load was applied to the specimen using the fixture of the testing machine until the fracture point was reached. The loading speed was maintained at 1 mm·min^{-1} using stroke control. Hardness measurements were carried out using a micro Vickers hardness tester with a force of 9.8 N for 15 s. The hardness values were measured at specific areas on the cast sample, including the areas containing α-Al grains and Si precipitates.

The microstructural characteristics of the surface of the cast ADC12 sample were examined using scanning electron microscopy (SEM), energy-dispersive X-ray spectroscopy (EDX), and electron backscatter diffraction (EBSD). The sample surface for these analyses were prepared using mechanical polishing with a cloth containing alumina particles. The EBSD analysis was conducted with an accelerating voltage of 15 kV, a beam current of 12 mA, and a step size of 1 μm.

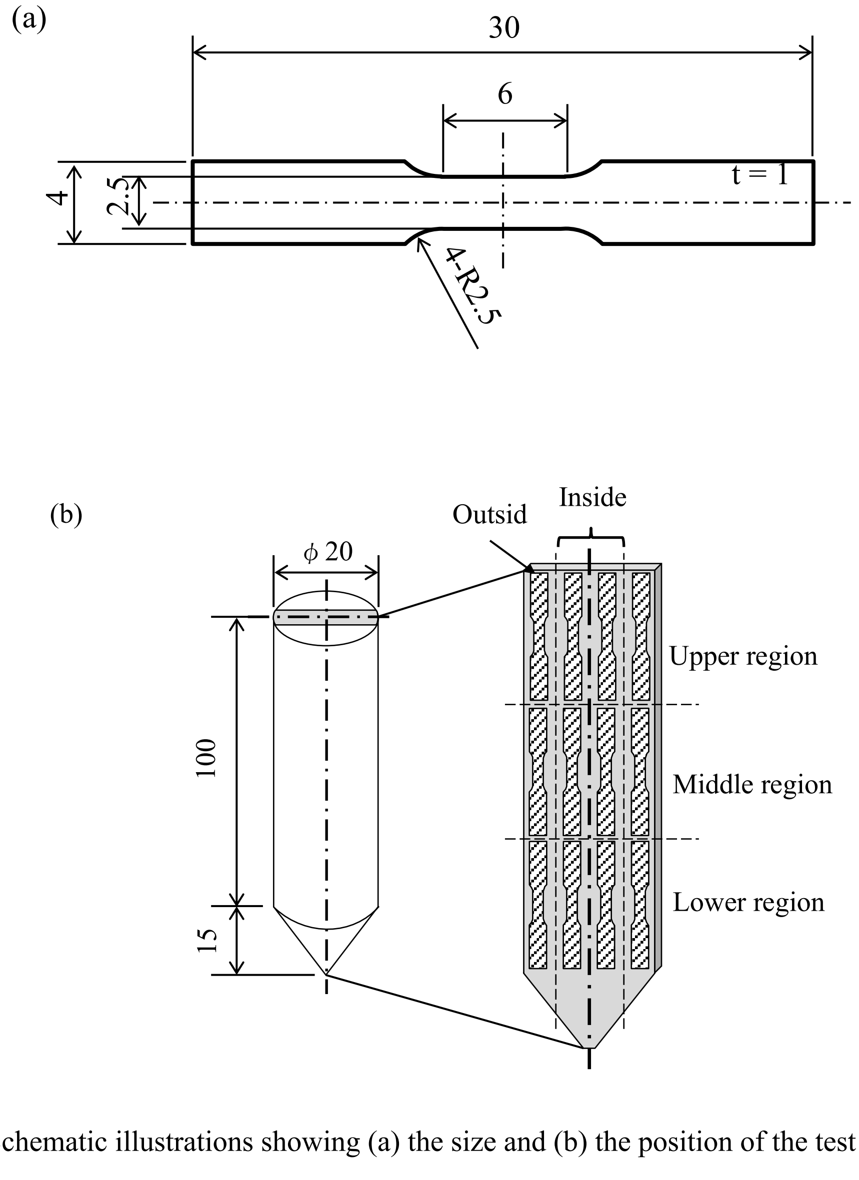

Fig. 3.3 Schematic illustrations showing (a) the size and (b) the position of the test specimen.

3.2 Results and discussion

3.2.1 Microstructural characteristics

The EBSD results shown in Fig. 3.4(a) depict the crystal orientation of the cast sample. The EBSD measurements were conducted in 11 different areas of the sample. Based on the inverse pole figure map (Fig. 3.4(a)), columnar grain growth with ⟨121⟩ orientation (purple in color) occurred adjacent to the solidification point (the triangular area in Fig. 3.4(a)). This columnar grain growth continued into the lower (areas 1-4) and middle (areas 5-7) regions of the sample, in which the crystal orientation was altered to ⟨215⟩ and ⟨101⟩. In the upper region (areas 8-11), columnar grain growth with ⟨001⟩ orientation occurred, and the area of columnar grain was narrower. In contrast, randomly orientated crystals were observed, especially on the outer region of the cast rod. We discuss the reason for this random orientation later.

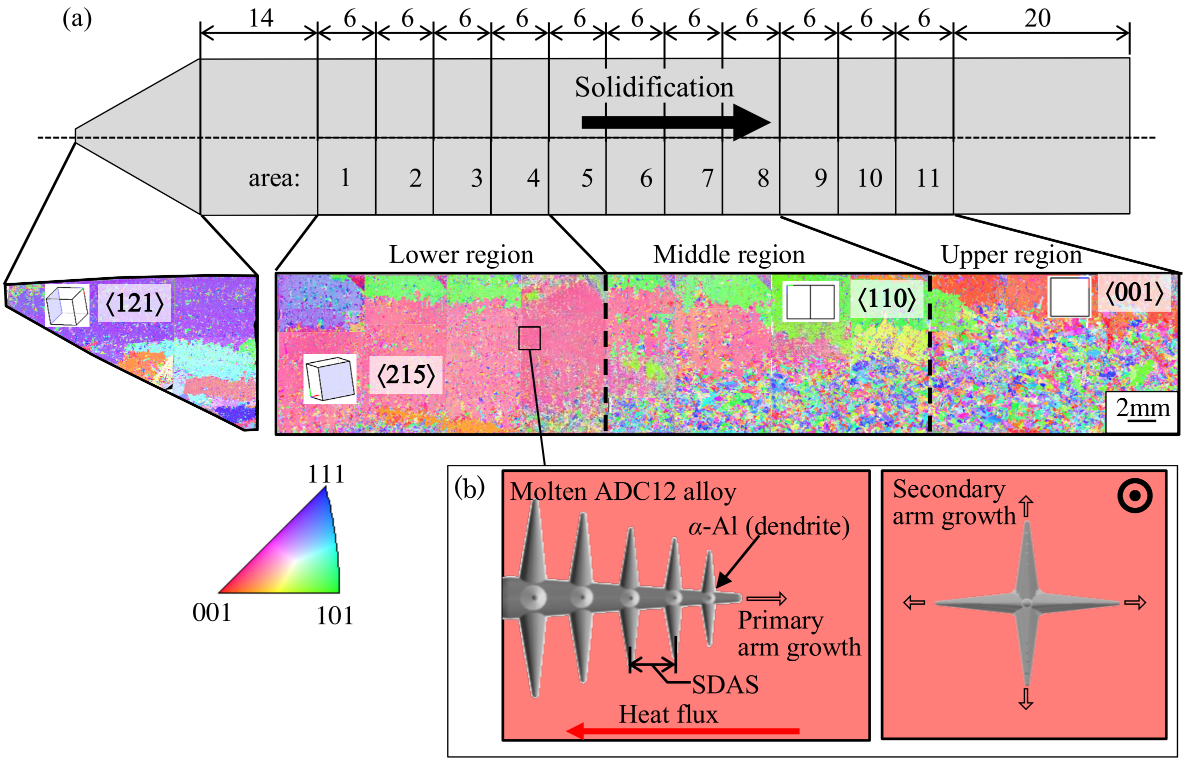

Fig. 3.4(a) EBSD-based inverse pole figure maps of the cast sample showing the crystal orientations in different locations on the sample, (b) a schematic illustration of the dendrite formation process.

Fig. 3.4(b) shows a schematic diagram of α-Al dendrite formation, which is configured with primary and secondary dendrite arms. To obtain a better understanding of the solidification characteristics, the mean secondary dendrite arm spacing (SDAS) of the cast sample was investigated. Fig. 3.5 shows the SDAS results measured in each area of the sample. No significant difference in SDAS was detected between the outer and inner regions of the cast sample. Distinct SDAS values were obtained for the fine and coarse microstructure in the lower and upper regions, respectively, with the middle region (areas 6 and 7) representing the transition between these two distinct SDAS regimes (Fig. 3.5). It is known that changes in SDAS values are strongly influenced by the cooling rate [2]. The cooling rate (V) of a cast aluminum alloy can be estimated using $V = 2 \times 10^{4}$ SDAS $^{-2.67}$ [3]. Based on this equation, the cooling rate was approximately 0.5 °C·s^{-1} in the lower region (areas 1-5) and 0.3 °C·s^{-1} in the upper region (areas 8-11). To obtain a more accurate cooling rate, direct measurement of the cast temperature was performed at three different points using thermal couples.

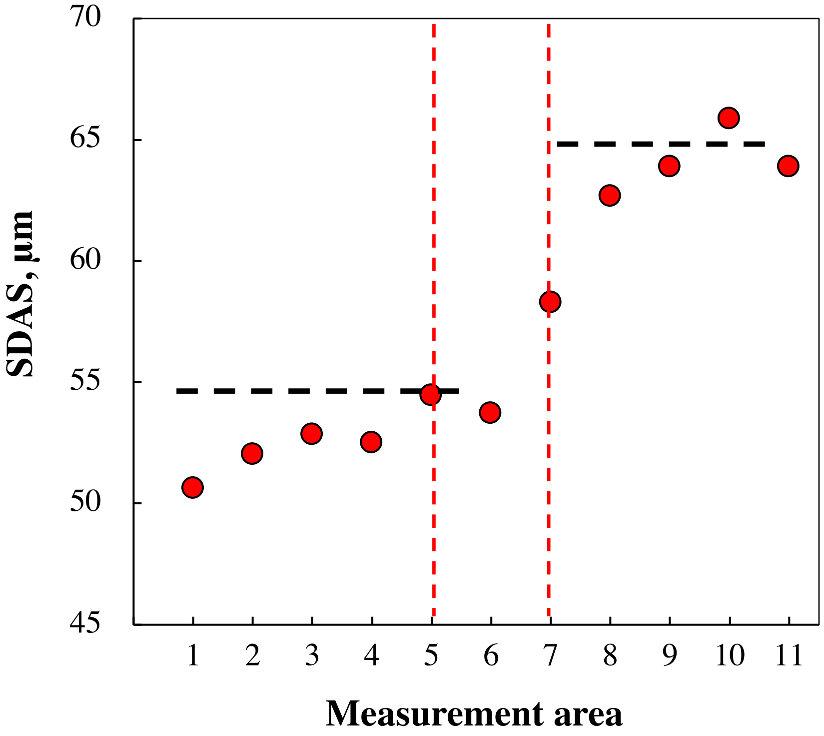

Fig. 3.5 The SDAS values measured in each area of the cast sample.

Figure 3.6(a) shows the temperature profiles of the ADC12 melt examined at the upper, center, and lower points. Similar to the mold temperature measurement results, the cast temperature was also altered: the temperature at the upper point was higher than that for the center and the lower points. The cooling rate of the three points was also calculated from the temperature curves. The lower point solidified faster, with a cooling rate of 0.14 °C·s^{-1}. Whereas, the ADC12 alloy melt solidified slowly at the middle and upper points, with a cooling rate of less than 0.05 °C·s^{-1}. The cooling rates obtained in the solidification processes reported here are similar to those of aluminum alloys reported in the literature [4, 5]. It should be pointed out that, in general, the liquidus region can be clearly detected from the point at which the temperature drops suddenly in the temperature curve [4, 6-7]. However, we did not observe this in our measurements, which might be attributed to the lower cooling rate of our casting process. In fact, the cooling rates reported here are lower than those reported for conventional gravity and die casting processes. To understand the solidification characteristics in more detail, the cooling curves were analyzed using the first derivative (dT/dt). The results obtained are shown in Fig. 3.6(b). As seen at the lower point, the dT/dt curve changes slightly at approximately 580 °C, marked as points A and B, indicating the formation of *α*-Al and eutectic Si, respectively [4]. However, similar to the result shown in Fig. 3.6(a), there is no clear change in the dT/dt curves for the center and upper points because of the slow cooling rate, which results in no significant change to the microstructure in the middle and upper regions. Based on the cooling rates of our sample, the cast rod may have solidified completely in only a few minutes even though the mold was cooled at a rate of 10 $°C{\cdot}h^{-1}$.

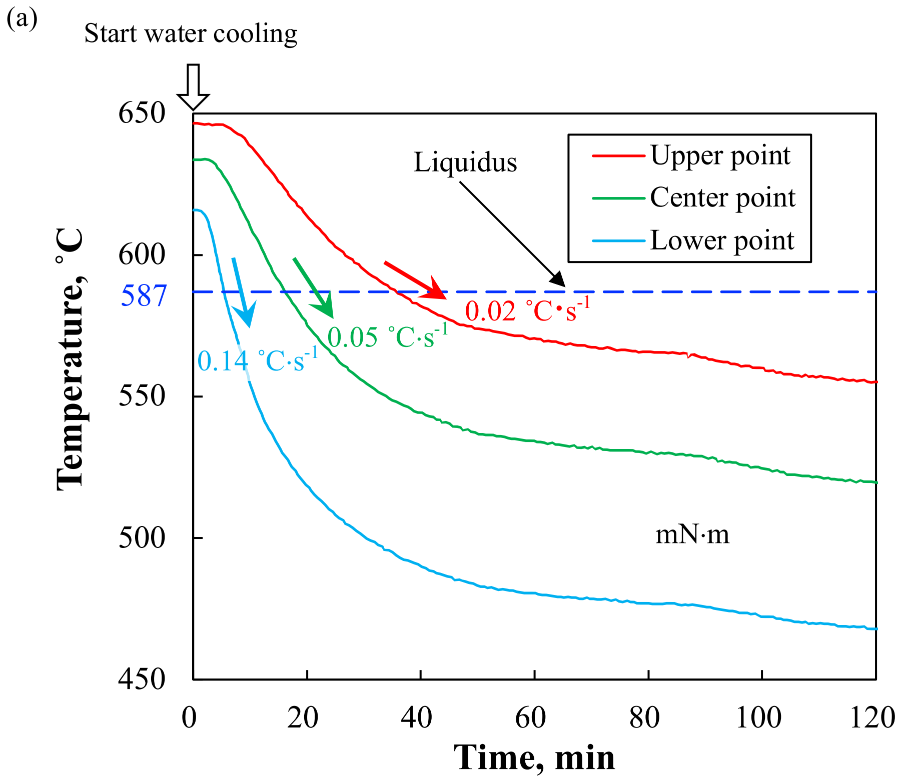

Fig. 3.6(a) Temperature profile and (b) first derivative (dT/dt) curves obtained at the upper, center, and lower points of the cast sample.

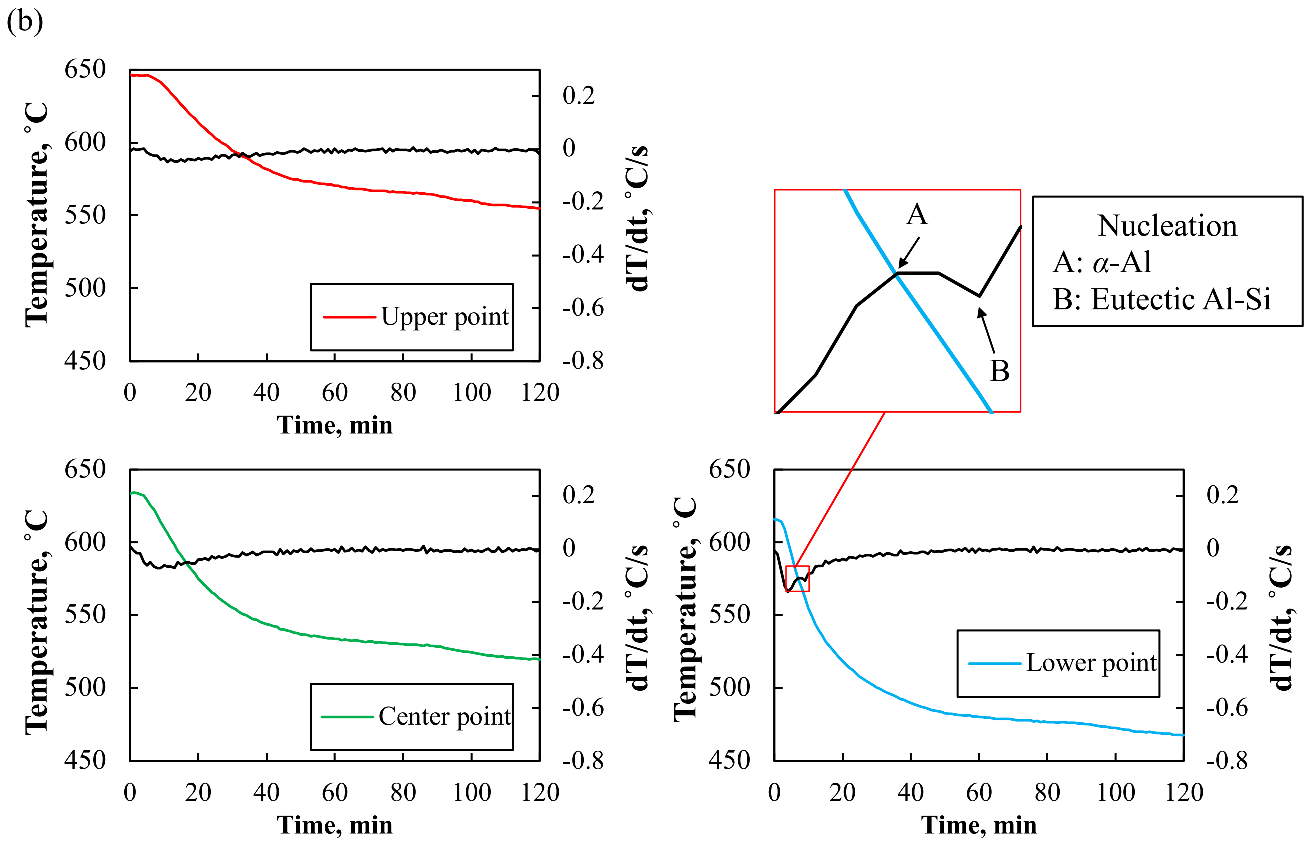

Fig. 3.6 Cont.

To understand the effects of the microstructural characteristics on the mechanical properties, hardness measurements were carried out. Figure 3.7 presents the mean Vickers hardness examined in each area of the sample. The mean hardness values were obtained from five measurement points and the standard deviation of the data was between 4.8 and 15.9. As can be seen, the hardness value changes depending on the measurement area, e.g., the hardness in the lower region (108 HV) was approximately 10% lower than that in the middle and upper regions. Overall, the hardness value for our sample was higher than that for the HPDC samples, which was 96 HV [3]; as described earlier, this may be caused by the low number of defects in the sample. As shown in Fig. 3.7, the variation in hardness values throughout the sample was similar to the variation in SDAS values. However, this result is questionable because cast aluminum alloys with fine microstructures (small SDAS) usually have high hardness values (i.e., the Hall-Petch relationship) [8].

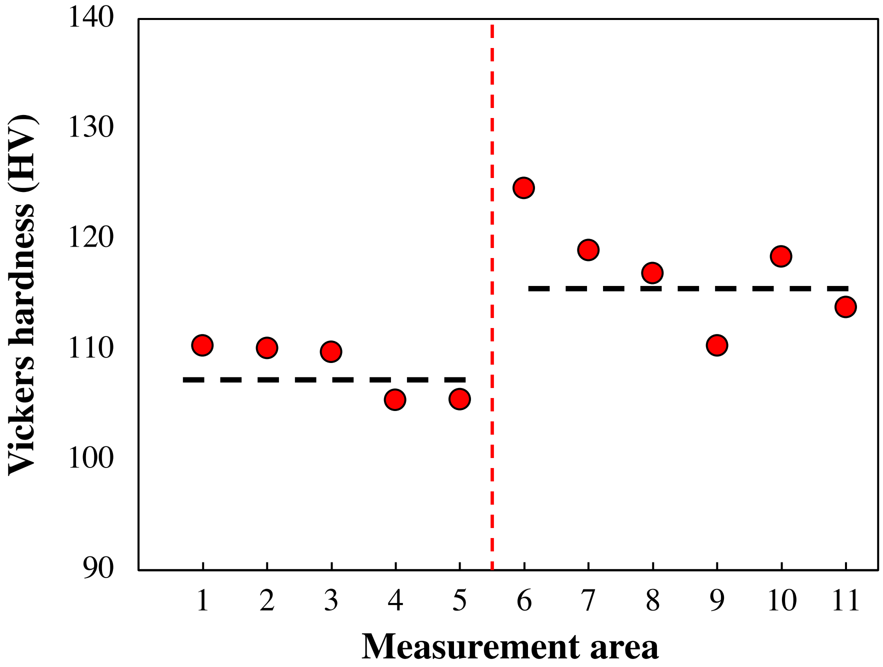

Fig. 3.7 The mean Vickers hardness results for each area of the cast sample.

To explain the above results, the microstructural characteristics were further examined. Figure 3.8(a) shows the SEM images and EDX maps for area 11 of the sample. It can be seen that the cast sample consists of α-Al, Si and Al-Fe-Mn phases. Figure 3.8(b) shows the SEM images and Si EDX maps for areas 1, 6, and 11 of the sample. It is clear that eutectic Si precipitates to a different extent in different areas; compared to the middle and lower regions, the eutectic Si grain size was larger in the upper region of the cast sample due to the lower cooling rate. Interestingly, we also confirmed the presence of primary Si with a rectangular shape in areas 6 and 11, despite the presence of the hypoeutectic Al-Si alloy (ADC12). Figure 3.9 shows the rate of Si formation, based on area 1, in each area of the sample. The area fraction of Si precipitate is clearly different between the sample areas. A low amount of Si precipitated in the lower region (areas 1-4), while the Si area fraction was significantly higher in area 5. The area fraction of Si precipitate further increased in the upper region moving from area 5 to area 11. The high Si content in the upper region is considered to correspond to primary Si [i.e., the amount of Si element increases to more than 11.6% Si (a hypereutectic Al-Si alloy), see Fig. 3.10]. As shown in Fig. 3.7, a high hardness value was obtained in the upper region, which may be caused by the high amount of hardened Si precipitate. In our previous work, the hardness of eutectic Si was examined using nanoindentation hardness testing, and was found to be significantly higher (approximately 3500 MPa) than that of α-Al grains [10]. It is also clear that the hardness in the middle region is as high as that in the upper region, which may be caused by high amounts of Si element, as shown in Fig. 3.9.

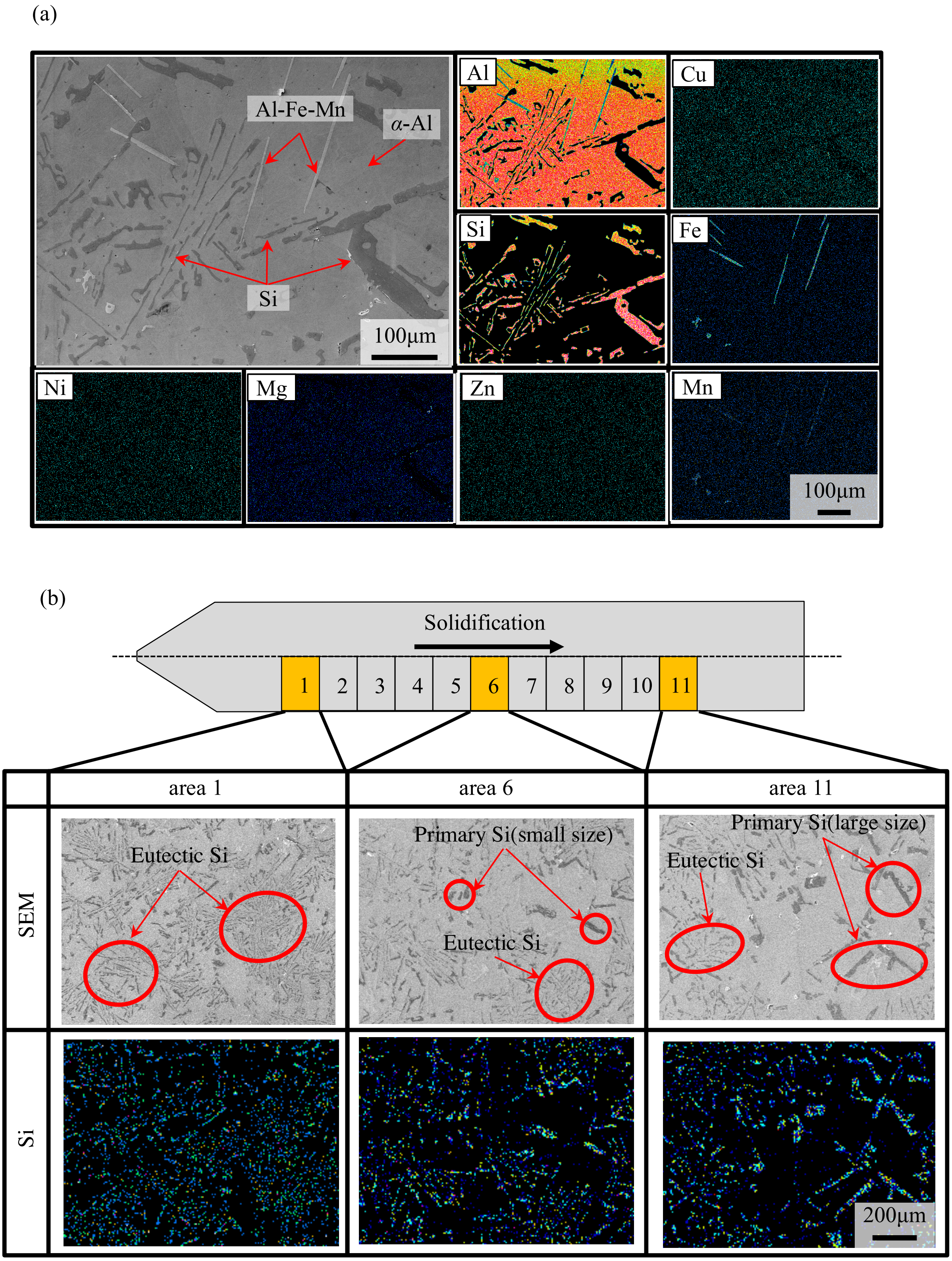

Fig. 3.8(a) SEM images and EDX maps for area 11, (b) SEM images and EDX maps of Si obtained for the lower, middle, and upper regions of the cast sample.

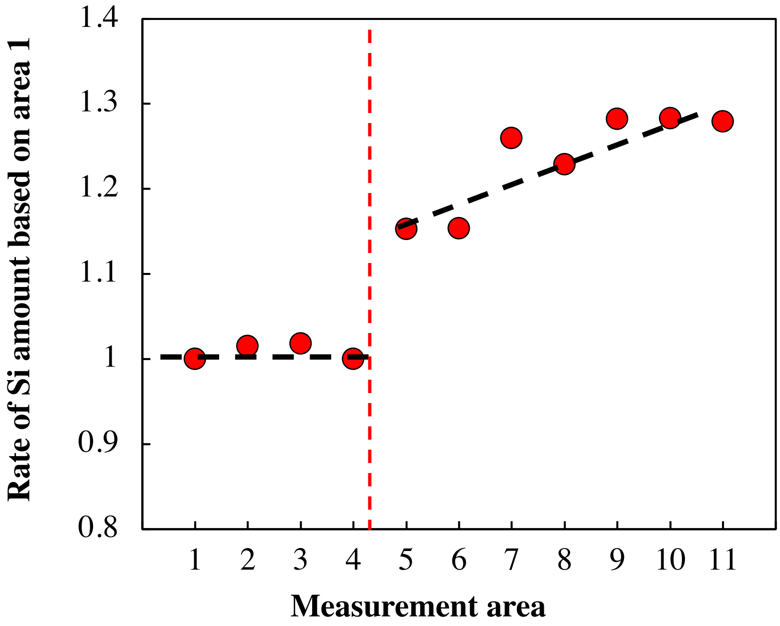

Fig. 3.9 The rate of Si formation, based on area 1, in each area of the cast sample.

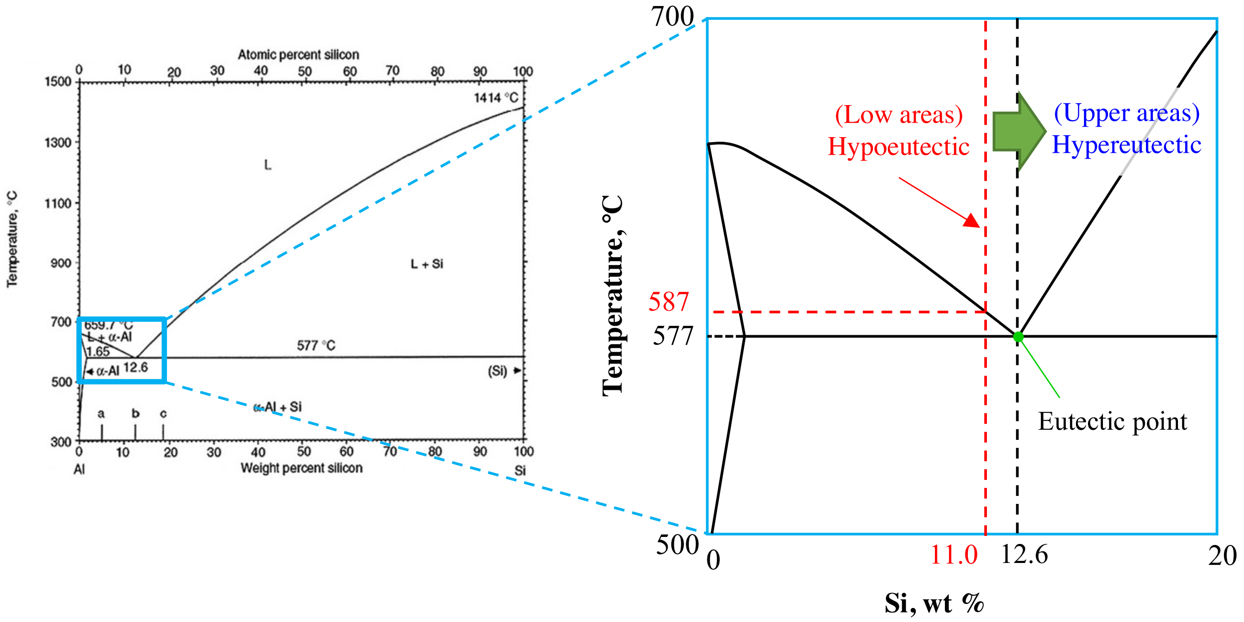

Fig. 3.10 A phase diagram for the Al-Si alloy representing the lower and upper regions of the cast sample [9].

A solidification mechanism for the cast sample was proposed based on the microstructural characteristics and is schematically illustrated in Fig. 3.11; it shows the direction of solidification and the sizes of eutectic and primary Si. Unidirectional solidification occurred in the lower region, leading to a relatively organized crystal orientation. In contrast, such controlled solidification was not observed in the upper region, which resulted in random crystal orientation. In this case, the difference in atomic dynamics and the creation of a core for the eutectic Si phase in the liquid state provided resistance to columnar grain growth during the solidification process [11].

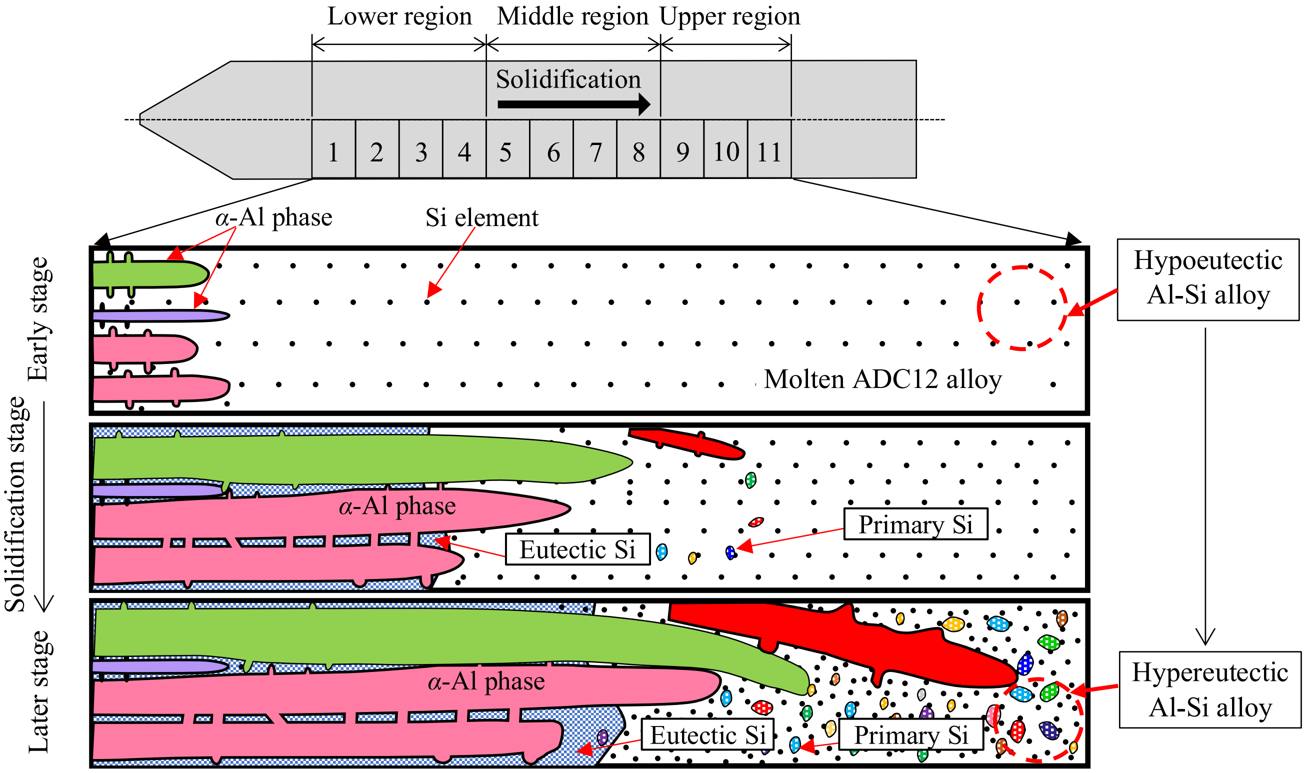

Fig. 3.11 The solidification models for the α-Al, eutectic Si, and primary Si phases in the different regions of the cast sample.

3.2.2 Mechanical properties

Figure 3.12 shows the measured tensile properties in the representative lower (area 3), middle (area 6), and upper (area 9) regions of the sample. Tensile tests were performed twice for each area. The tensile properties indicated a different trend than that observed for the hardness values (Fig. 3.7). A high tensile strength and high fracture strain were clearly observed in area 1: σ_{UTS} = 170 MPa and ε_{f} = 0.8%, while the tensile strength and fracture strain were lower in areas 6 and 11. The high tensile strength in the lower region was related to the fine, uniformly oriented microstructure with low Si content. In contrast, the low tensile strength in the upper region can be attributed to the α-Al phase and a large amount of hard, primary Si (Fig. 3.8(b)) as well as the formation of a large amount of eutectic Si precipitate. The tensile strength was relatively low and variable in the upper and outer regions of the cast sample, which may be caused by the microstructural characteristics, as mentioned above. In this study, the tensile properties (σ_{UTS} and ε_{f}) are much lower than that of the HPDC samples (σ_{UTS} = 240 MPa and ε_{f} = 4%) [3]. This is influenced by the high stress concentration, which is caused by the large amount of eutectic Si phase formed as a result of the slow cooling rate.

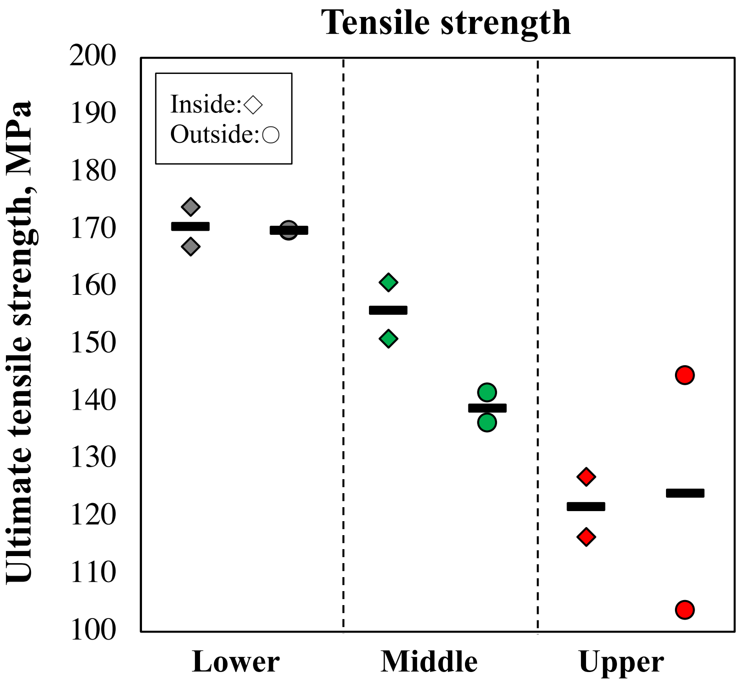

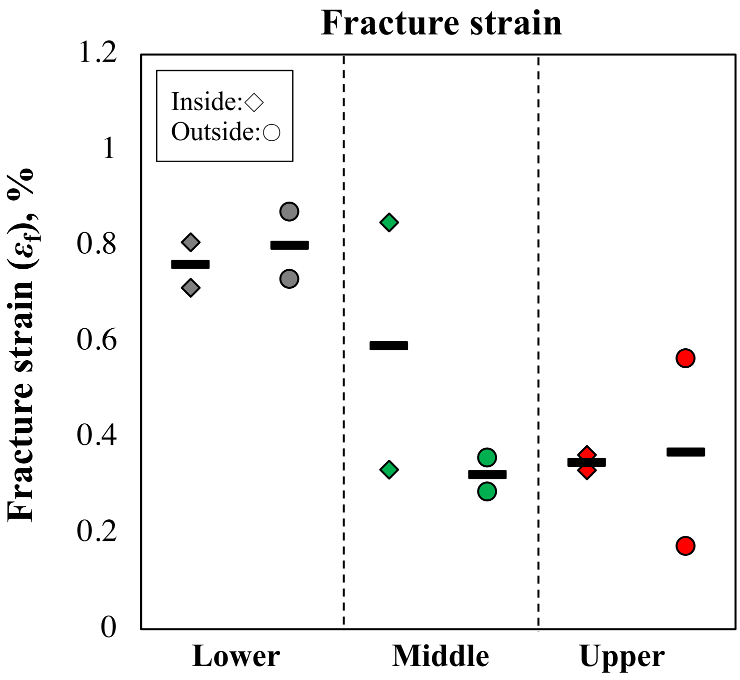

Fig. 3.12 The tensile properties of the cast sample obtained in the lower, middle, and upper regions.

3.3 Summary

The properties of an ADC12 alloy material produced via a unidirectional casting process were investigated. The results obtained can be summarized as follows:

1) The microstructural characteristics of the cast sample differed depending on the solidification area. Columnar grain growth was observed in the lower (areas 1-4) and middle (areas 5-7) regions of the sample, where crystals with ⟨215⟩ and ⟨101⟩ orientations were formed. In comparison, in the upper region (areas 8-11), the area of columnar grain growth was narrower, and randomly oriented crystals were formed. This was attributed to the interruption of columnar α-Al dendrite growth resulting from a higher Si content in the upper region.

2) Despite the Al-Si alloy of ADC12 being hypoeutectic, primary Si precipitated in addition to the eutectic Si in the middle and upper regions of the cast sample. This was caused by the migration of Si into the upper region, as the columnar growth of α-Al dendrites occurs before the precipitation of eutectic Si.

3) Fine and coarse microstructures were observed in the lower and upper regions of the sample, respectively, with the middle region (areas 6 and 7) representing a transition zone. The cooling rates in our cast sample were of both high and low levels: approximately 0.14 $°C\cdot s^{-1}$ for the lower region and 0.05 $°C\cdot s^{-1}$ for the upper region, respectively.

4) Low and high hardness values were observed in the lower and upper regions, respectively. The high hardness value was primarily attributed to a large amount of precipitated hard Si phases. In addition, a high tensile strength and high ductility were obtained in the lower region of the sample due to the fine microstructure with unidirectional crystal formation.

References

1. L.S. Langston, Each blade a single crystal, Am. Sci., 103(2015)30-33.

2. H. Borkar, S. Seifeddine, A. E. W. Jarfors, Microstructure analysis of Al-Si-Cu alloys prepared by gradient solidification technique, Int. J. Mod. Phys. B, 29(2015)1-7.

3. M. Okayasu, Y. Ohkura, S. Takeuchi, S. Takasu, H. Ohfuji, T. Shiraishi, A study of the mechanical properties of an Al-Si-Cu alloy (ADC12) produced by various casting processes, Mater. Sci. Eng. A, 543(2012)185-192.

4. R. Mackay, J. Sokolowski, Experimental observations of dendrite coarsening & Al-Si eutectic growth in progressively quenched structures of Al-Si-Cu casting alloys, Int. J. Metalcast., 2(2008)57-75.

5. S.M. Sadrossadat, S. Johansson, R.L. Peng, EBSD investigation of the effect of the solidification rate on the nucleation behavior of eutectic components in a hypoeutectic Al-Si-Cu alloy, Met. Mater. Int., 18(2012)405-411.

6. M. Ayabe, T. Nagaoka, K. Shibata, H. Nozute, H. Koyama, K. Ozaki, T. Yanagisawa, Effect of high thermal conductivity die steel in aluminum casting, Int. J. Metalcast., 2(2008)47-55.

7. R. Mackay, J. Sokolowski, Comparison between wedge test castings and component engine block casting properties, Int. J. Metalcast., 4(2010)33-50.

8. W.R. Osório, P.R. Goulart, G.A. Santos, C.M. Neto, A. Garcia, Effect of dendritic arm spacing on mechanical properties and corrosion resistance of Al 9 Wt Pct Si and Zn 27 Wt Pct Al alloys, Metall. Mater. Trans. A, 37(2006)2525-2538.

9. M. Warmuzek, Aluminum-silicon casting alloys: Atlas of microfractographs, ASM Intl., (2004)1-3.

10. M. Okayasu, S. Takasu, M. Mizuno, Relevance of instrumented nano-indentation for the assessment of the mechanical properties of eutectic crystals and α-Al grain in cast aluminum alloys, J. Mater. Sci., 47(2012)241-250.

11. M. Okayasu, S. Takeuchi, Crystallization characteristics of cast aluminum alloys during a unidirectional solidification process, Mater. Sci. Eng. A, 633(2015)112-120.

Chapter 4 Effects of Artificial Aging on Mechanical Properties of Al-Si-Cu Foundry Alloy

4.1 Experimental procedures

4.1.1 Material and sample preparation

A JIS-ADC12 (Al-Si-Cu-based) aluminum alloy was employed. The chemical composition of the alloy is presented in Table 3.1. Cast samples were prepared by conventional gravity casting (GC) and by heated mold continuous casting (HMC). Figure 4.1 shows the schematic illustration of the GC and HMC samples and the location of the test samples to investigate their microstructural and mechanical properties. For the GC, the metal ingot was created by pouring the molten metal from a ladle into a mold of approximately 600 × 90 × 40 mm^3. For the HMC, a round rod cast sample of ϕ5 mm × 1 m was created using a horizontal HMC device (see Fig. 1.4) consisting of a melting furnace, a graphite mold, a graphite crucible, and a cooling device. [1]. The ADC12 ingot, cut into small pieces (15 × 15 × 15 mm^3), was melted using an air furnace maintained at 635 °C, which is about 50 °C, higher than the alloy's melting point. The molten metal was fed continuously from the mold to the outside at 1.9 $mm{\cdot}s^{-1}$ via a runner using a motor-driven system. The mold was heated directly using ceramic heaters to a target temperature of 625 °C. The round rod HMC sample was cooled directly by a water droplet spray applied at a rate of approximately 1.3 $ml{\cdot}s^{-1}$ to its top surface. The details of the HMC process can be found in Refs. [1, 2]. The cooling rate of the GC and HMC processes was 14.5 $°C{\cdot}s^{-1}$ and 200.5 $°C{\cdot}s^{-1}$, respectively.

4.1.2 Aging conditions

Heat treatment was carried out under various aging conditions to obtain excellent mechanical properties for cast aluminum alloys(Fig. 4.2), with the aging temperature and time determined on the basis of previous work [3-5]. The aging process was performed and maintained at five different temperatures (145, 160, 175, 190 and 220 °C), with aging times ranging from 1 to 200 h. Before the aging process, solution treatment was performed; the samples were heated to 525 °C in an air furnace for 12 h and then quenched with water. It should be noted that no apparent defects (blisters or cracks) were detected in the cast samples after heat treatment.

GC sample

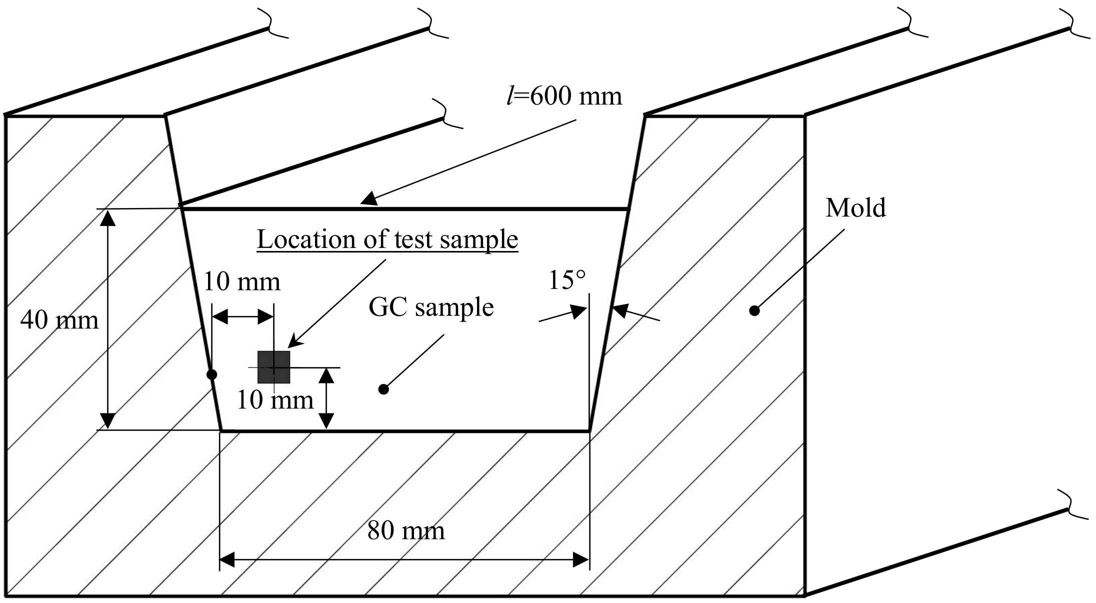

HMC sample

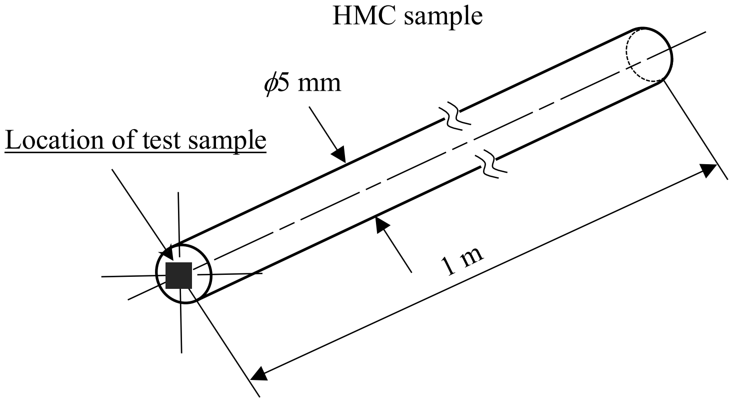

Fig. 4.1 Schematic diagrams of the GC and HMC samples and location of the test sample for examination of microstructural.

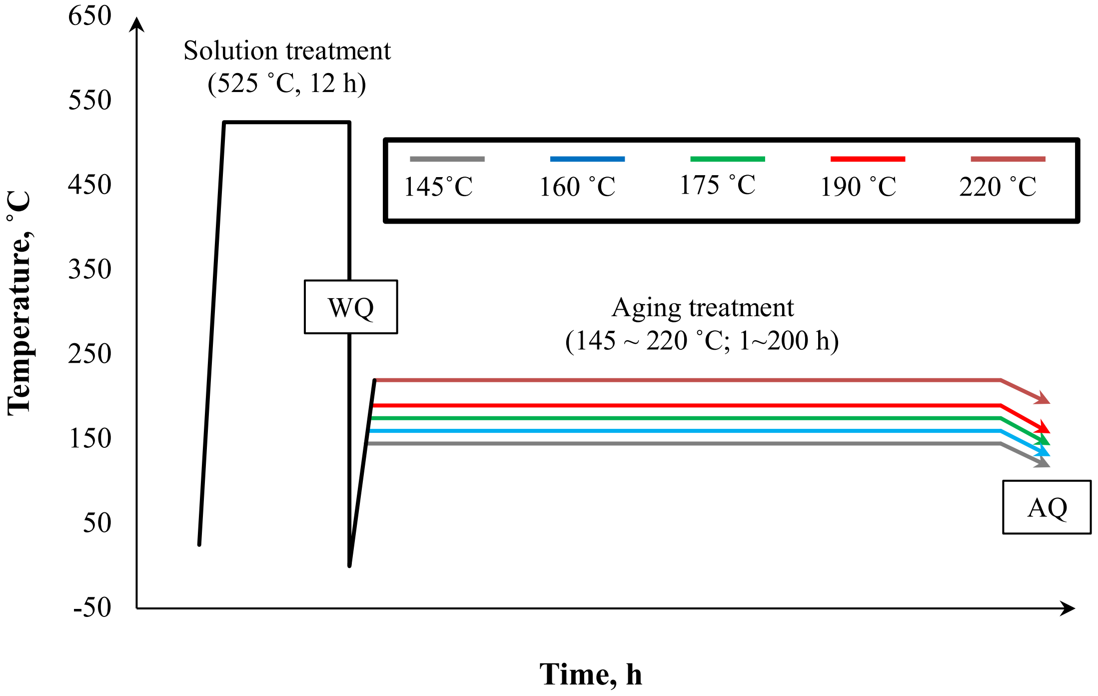

Fig. 4.2 Heat treatment conditions for casting sample.

4.1.3 Mechanical and microstructural examinations

The mechanical properties of the cast samples were investigated by hardness, tensile and fatigue tests. The hardness was evaluated by a Vickers hardness tester, where a standard diamond indenter was loaded on the sample surfaces at 9.8 N for 15 s. The tensile and fatigue properties were investigated using a hydraulic-type testing machine with 50 kN capacity at room temperature. In the tensile tests, the specimens were loaded at a loading speed of 1 mm·min^{-1} to final fracture (JIS Z2241). The load and strain values were measured by a standard load cell and strain gauge, respectively. The fatigue tests were carried out under sinusoidal cyclic loading at a frequency of 30 Hz, where tensile-tensile cyclic loading was conducted at R = 0.1 under load control until final fracture or 10^6 cycles. Figure 4.3 displays the dimension of the test specimens for the tensile and fatigue tests, which were designed based on JIS Z2201-No. 8.

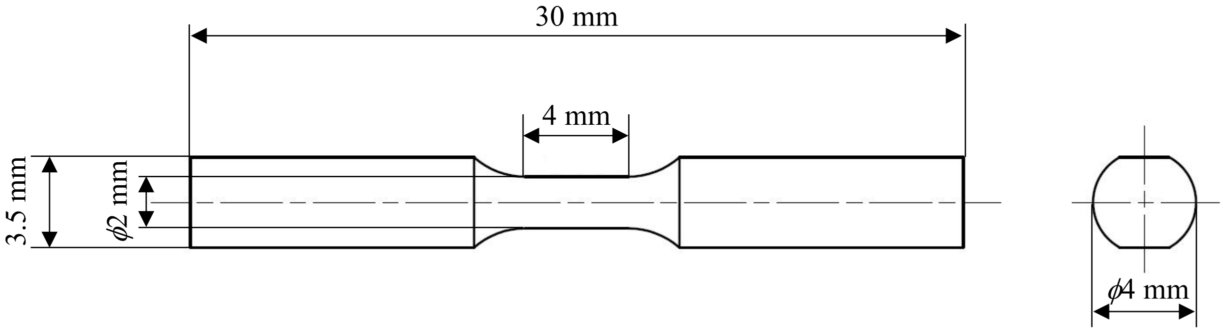

Fig. 4.3 Test specimens for tensile and fatigue tests.

Microstructural characteristics introduced by the aging processes were examined by electron energy-dispersive X-ray spectroscopy (EDX), backscatter diffraction (EBSD) and transmission electron microscopy (TEM). The TEM samples were prepared by conventional methods such as mechanical thinning followed by ion thinning to about 100 nm thickness. The test piece was machined directly from the cast sample, the microstructure of the cast sample was observed, and its mechanical properties were investigated. Figure 4.1 shows a schematic showing the location of specimens for GC and HMC samples.

4.2 Results and discussion

4.2.1 Microstructural characteristics

Figure 4.4 shows the optical micrographs of representative GC-Al and HMC-Al alloys before and after the aging processes: sample A (as-cast), sample I (175 °C for 13 h), sample II (175 °C for 100 h) and sample III (220 °C for 100 h). The microstructure consists basically of the α-Al phase and various eutectic structures, such as $CuAl_2$, Al-Fe-Mn and Si, which are embedded between the α-Al phases. The sizes of these structures vary according to the cooling rate, with large α-Al grains and acicular eutectic structures (Si and Al-Fe-Mn) for GC samples and fine α-Al grains and tiny eutectic structures for HMC samples. After the aging process (HT), the shape of the microstructures is changed, fragmented eutectic and spheroidal eutectic particles [6] are observed in the HT-GC and HT-HMC samples, respectively. There is no apparent difference in the size of α-Al grain among the cast samples after the aging process. However, comparing HMC sample I and HMC sample II shows a slightly different size of the eutectic phases: the larger eutectic phases are obtained for the sample with the longer aging time.

GC HMC

(a) Sample A: as-cast

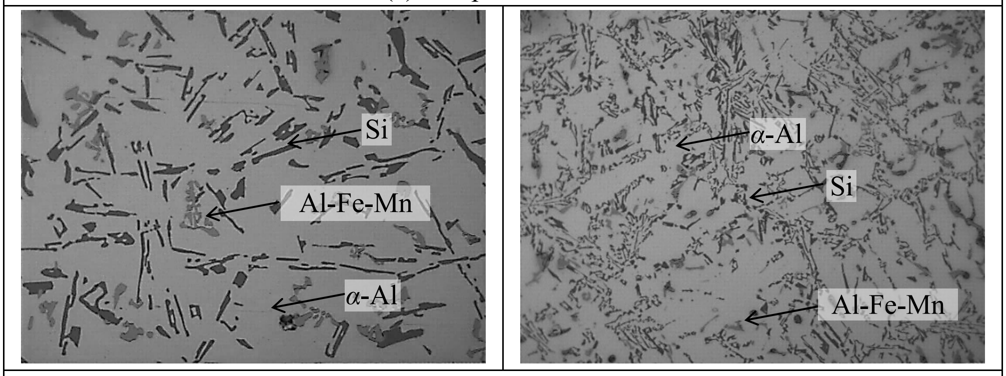

(b) Sample I: 175 °C, 13 h

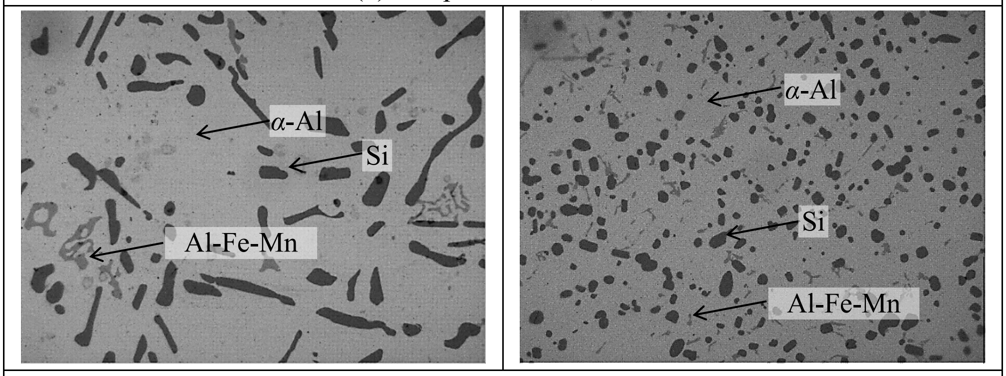

(c) Sample II: 175 °C , 100 h

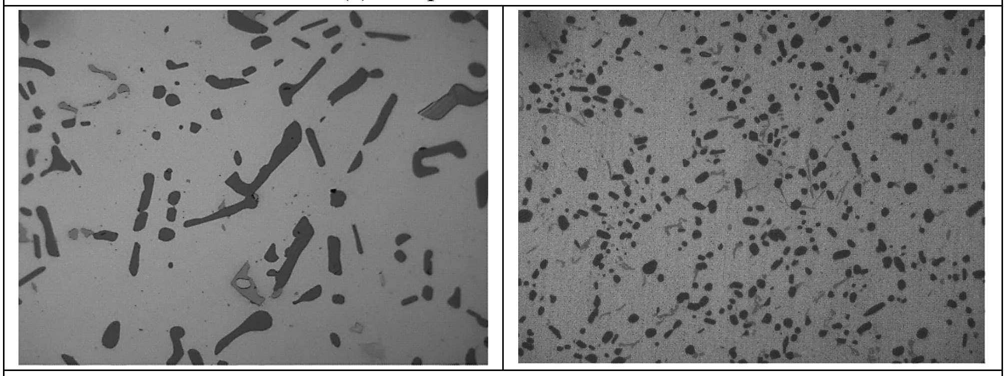

(d) Sample III: 220 °C , 100 h

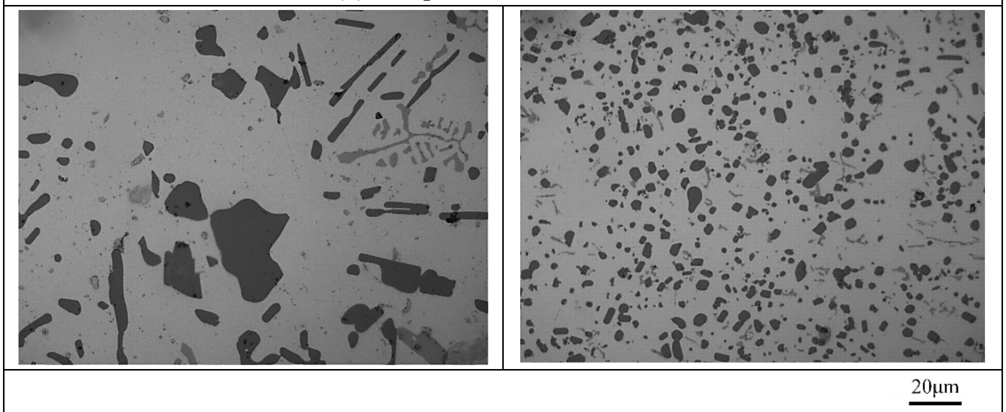

Fig. 4.4 Optical micrographs of GC and HMC samples before and after aging: (a) sample A (as-cast); (b) sample I (175 °C for 13 h); (c) sample II (175 °C for 100 h); (d) sample III (220 °C for 100 h).

Furthermore, to reveal the micro characteristics, crystal orientation analysis was performed by EBSD. The results are shown in Fig. 4.5: (a) Sample A (as-cast sample) and (b) Sample I (175 °C for 13 h). The crystal orientation characteristics were evaluated with an inverse pole figure (IPF) map and pole figure. The color level of each pixel in the IPF maps is defined according to the deviation of the measured orientation, as indicated in the stereographic projection. Different crystal orientations can be seen in the GC sample in the as-cast sample, depending on the grain. On the other hand, rather like a true single crystal, the crystal orientation for the HMC sample is almost perfectly orientated. From the results of the pole figure, it was found that the crystal orientations of the HMC samples were formed in $\langle 100 \rangle$ directions. It could be due to the unidirectional solidification process in the HMC process [7]. In contrast, the crystal orientation of the GC sample was random. The differences in the crystal orientations can no longer be detected clearly before and after the aging process. It was also confirmed that the grains size of the HMC samples is finer than those of the GC samples in this approach.

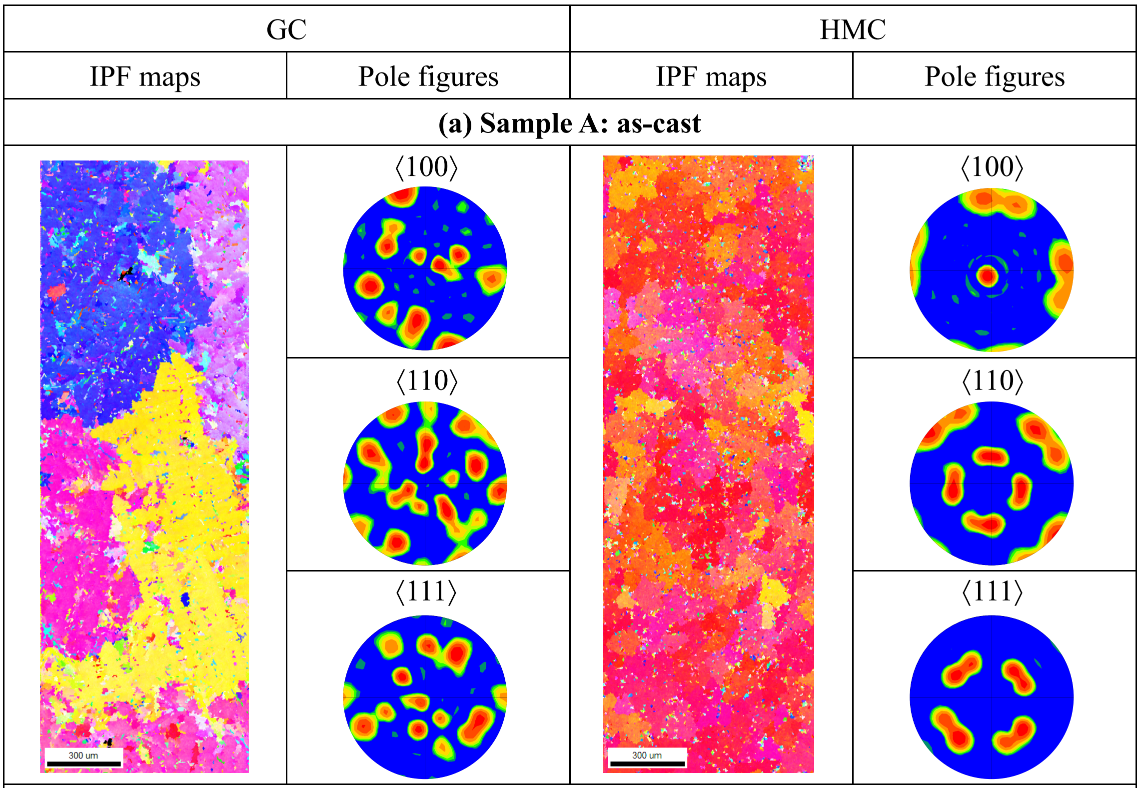

(b) Sample I: 175 °C, 13 h

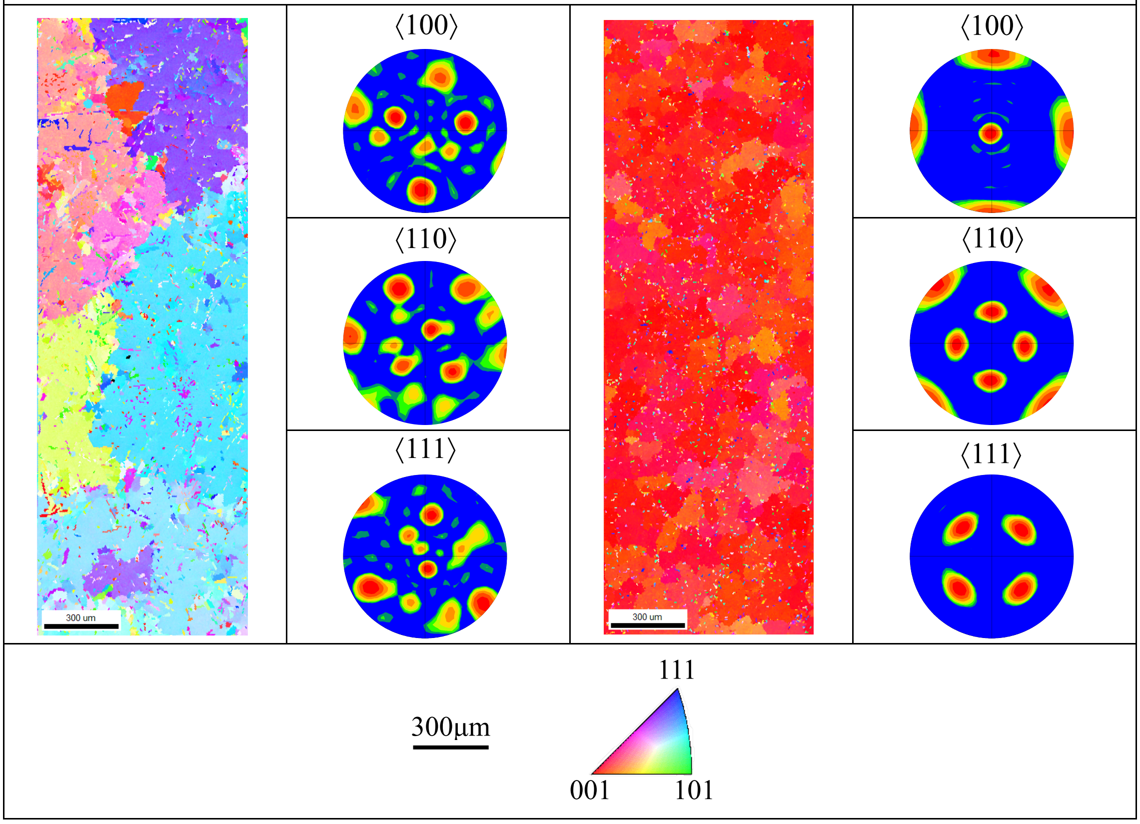

Fig. 4.5 Microstructural characteristics of GC and HMC samples: (a) sample A (as-cast) and (b) sample I (175 °C for 13 h) examined by EBSD.

4.2.2 Vickers hardness

Figure 4.6 displays the change of Vickers hardness as a variable of aging time. The data plots show the mean hardness value obtained from more than 10 measurement data, where the hardness measurement was taken in the area including the α-Al grains as well as various eutectic phases. It seems that the hardness data are relatively unstable, whereas there are clear hardness trends overall. The instability of the data is due to the presence of a number of eutectic structures with different hardness levels. The Martens hardness of Cu-based eutectic phases is about 798 MPa, which is similar to that of the α-Al grains. However, the hardness of the Si- and Fe-based eutectic structures are as high as 4109 and 6361 MPa, respectively [8]. From Fig. 4.6, it can be seen that the variations of the Vickers hardness of the GC and HMC samples show different trends depending on the aging condition, with the hardness level of the GC sample being higher overall than that of the HMC sample. This result was verified by hardness measurement of the α-Al grains alone for the GC and HMC samples (Fig. 4.7). It can be seen that, as with the results in Fig. 4.6, the hardness of the GC sample appears to be higher overall than that of the HMC sample. However, this result is questionable, since (i) the HMC sample, having finer microstructures, should have strong grain boundary strengthening, and (ii) the hardness of the heat-treated GC and HMC samples should be at the same level, owing to the solid solution process at high temperature (525 °C). These discrepancies will be discussed later in this paper. The hardness value increases nonlinearly with increasing aging time for samples aged at 145 °C, and it saturates at around 145 HV after heating for more than 50 h, which is about 25% higher than the hardness of the as-cast samples. At aging temperatures of 160, 175 and 190 °C, the hardness increases remarkably during the early stage of aging, and aging peaks in hardness variation are obtained when samples are heated for 10-15 h. At an aging temperature of 175 °C, a clear aging peak with the highest hardness is detected at about 13 h, where strong precipitation hardening would have occurred. A similar result was observed in previous work by Sjölander and Seifeddine [9], where Al-7Si-0.45Mg-*x*Cu (0-3%) alloys were aged at 175 °C and high hardness values were detected at about 10 h. Another approach was adopted by Furui et al. [10], using Al-10Si-0.5Mg alloy, in which high hardness was obtained at an aging temperature of 150 °C, but low hardness at 200 and 250 °C. It is interesting to note that the hardness variations for the samples aged at 160, 175 and 190 °C seem to have double aging peaks. Similar double aging peaks were identified by Li et al. [5], who investigated the age-hardening behavior of cast Al-9.55Si-2.48Cu-0.53Mg alloys (in wt%). They reported that an "obvious interval during the transition from GP zone to metastable phase, which is caused by dissolution of GP zone and the nucleation of metastable phase on dislocation, may be the main reason of the formation of double aging peaks" [5]. With prolonged aging at 220 °C, as shown in Fig. 4.7, the hardness value gradually declined as a result of an over-aging effect, with the hardness value after aging for 100 h (sample III) being as low as 100 HV, which is about 10% lower than the hardness of the as-cast samples. A related approach was adopted by Lumley et al. [11], who examined the effects of aging time on hardness for similar Al-Si-Cu alloys, produced by a high-pressure die-casting process. In their work, a clear hardness peak was seen after aging at 220 °C for about 12 min, although this result indicates a different trend compared with ours.

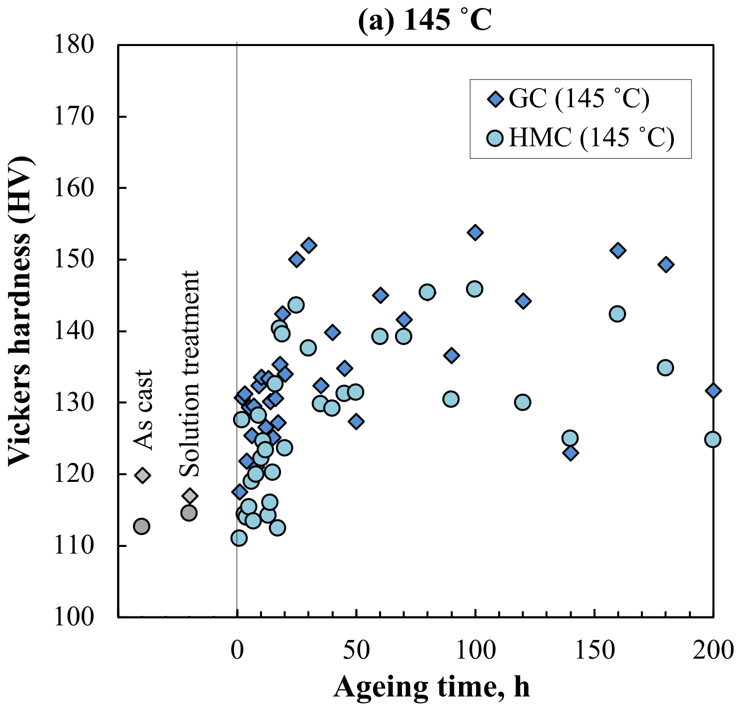

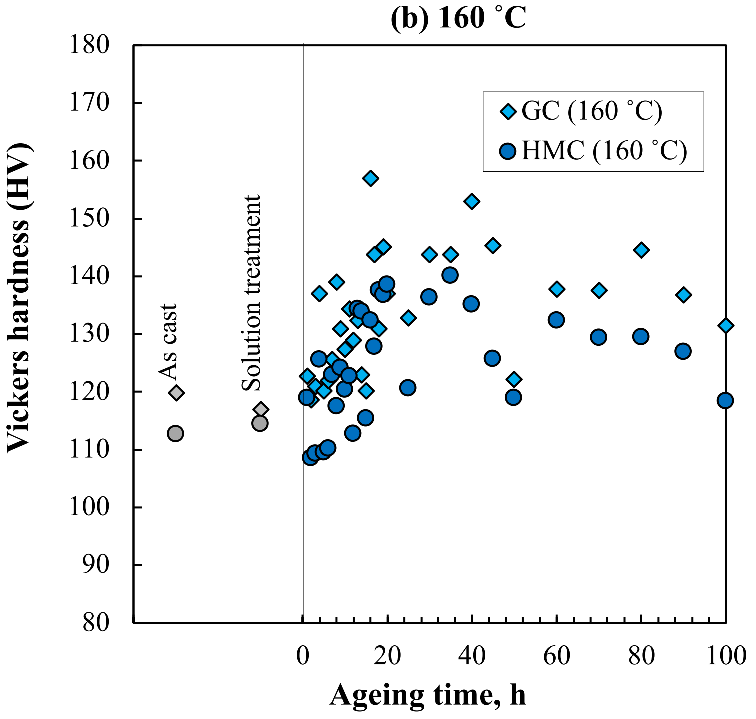

Fig. 4.6 Change of Vickers hardness as a variable of aging time for GC and HMC samples: (a) 145 °C; (b) 160 °C; (c) 175 °C; (d) 190 °C; (e) 220 °C.

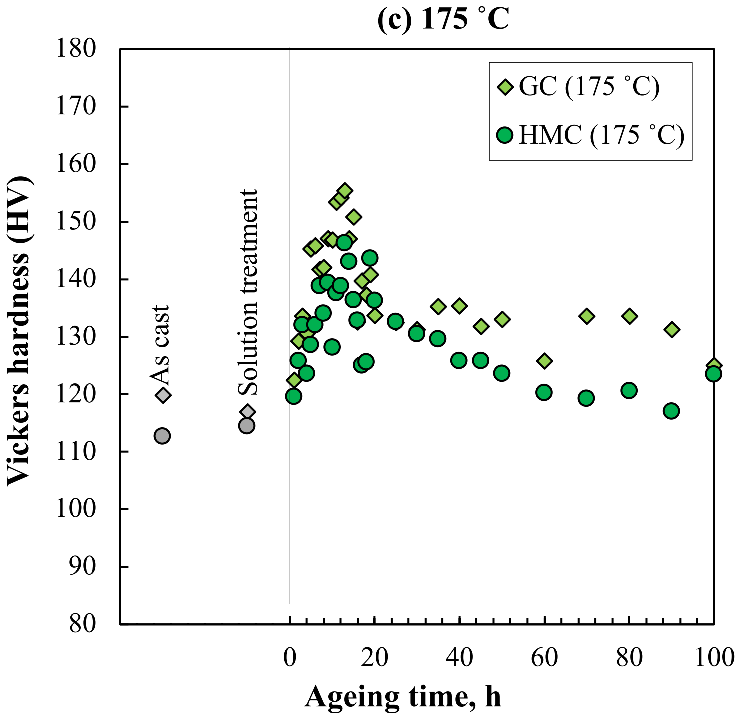
(c) 175 ˚C
Vickers hardness (HV)
180
170
160
150
140
130
120
110
100
90
80
As cast
Solution treatment
0
20
40
60
80
100
Ageing time, h
◆ GC (175 ˚C)
● HMC (175 ˚C)

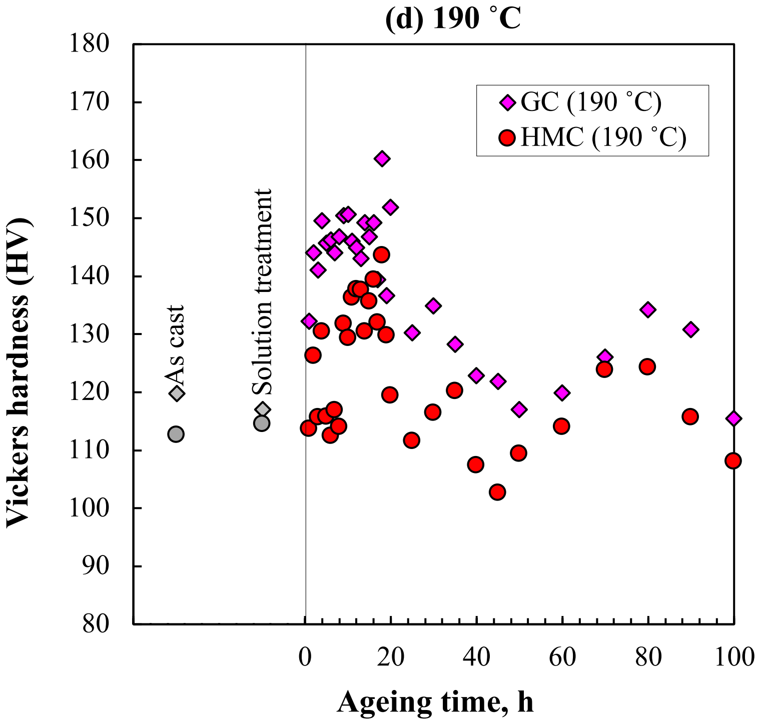
(d) 190 ˚C
Vickers hardness (HV)
180
170
160
150
140
130
120
110
100
90
80
As cast
Solution treatment
0
20
40
60
80
100
Ageing time, h
◆ GC (190 ˚C)
● HMC (190 ˚C)

Fig. 4.6 Cont.

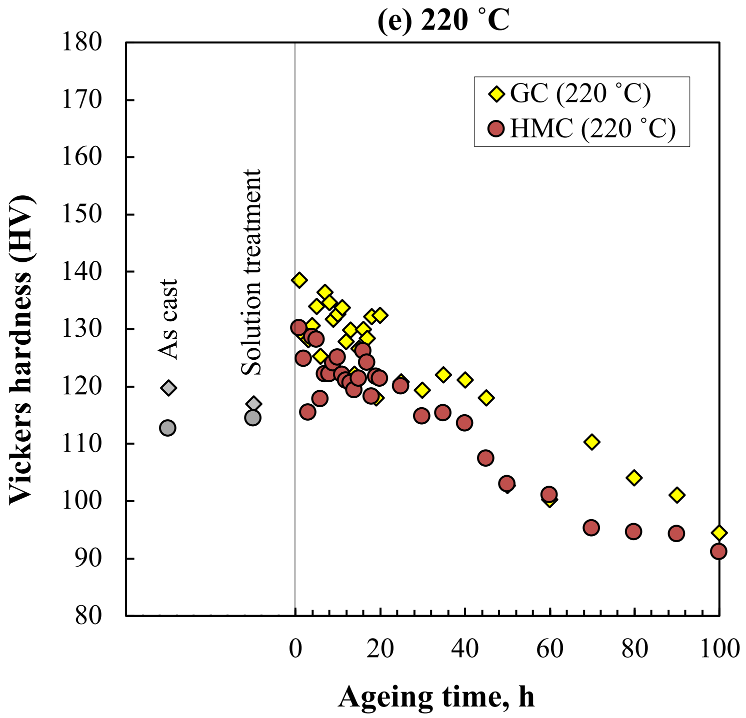

Fig. 4.6 Cont.

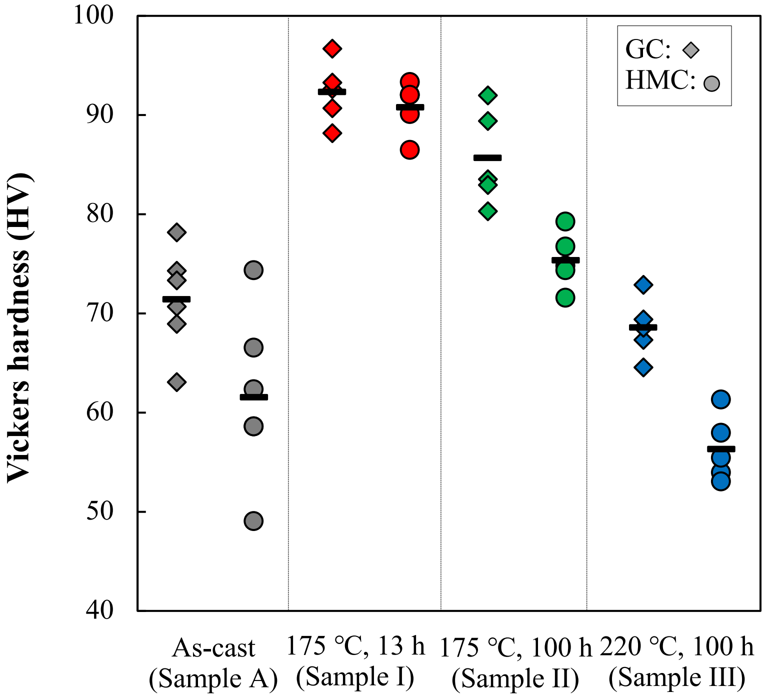

Fig. 4.7 Vickers hardness of α-Al grains for GC and HMC samples.

4.2.3 Tensile properties

Figure 4.8(a) shows tensile stress-tensile strain curves for representative samples, namely the as-cast sample A and the aged samples I, II and III. It is clear that the stress-strain curve shows different trends depending on the aging, with the tensile strength and ductility apparently being altered. Based on the stress-strain curve, the ultimate tensile strength σ_{UTS}, 0.2% proof strength $\sigma_{0.2}$ and fracture strain ε_f are summarized in Fig. 4.8(b) - (d). Note that more than three specimens were tested in each sample. The ultimate tensile strength for GC sample A is lower than that for HMC sample A. This is a different trend to their hardness results in Fig. 4.6, and this is due to the different extents of stress concentration around the brittle eutectic phases, where a higher stress concentration is possible for the GC sample because of the larger eutectic phases, as mentioned above. T The highest tensile strength is obtained for HMC sample I and is about 15% greater than GC sample I and HMC sample A. This could be due not only to the refined microstructure but also to the precipitation hardening. In contrast, the σ_{UTS} values of HMC samples II and III are lower than GC samples II and III, respectively, even though higher ductility was measured for the HMC samples. The highest ductility of over 30% was obtained in HMC Sample III. This is more than five times the ductility of HMC sample A. Such a high ductility for ADC12 alloy has not been reported previously. On the other hand, no apparent improvement in ductility is detected for the HT-GC samples. These experimental results show that the tensile strength and ductility of the HMC samples are more sensitive to the aging process than those of the GC samples. Lumley et al. [11] investigated the tensile properties of ADC12 after T6 treatment and found that after aging at 150 ° C for 24 hours, high tensile strength was obtained: σ_{UTS} = 382 MPa and $\sigma_{0.2}$ = 294 MPa. However, the elongation at failure was as low as 2.4% [11], less than one-sixth of HMC Sample I (175 ° C, 13 h).

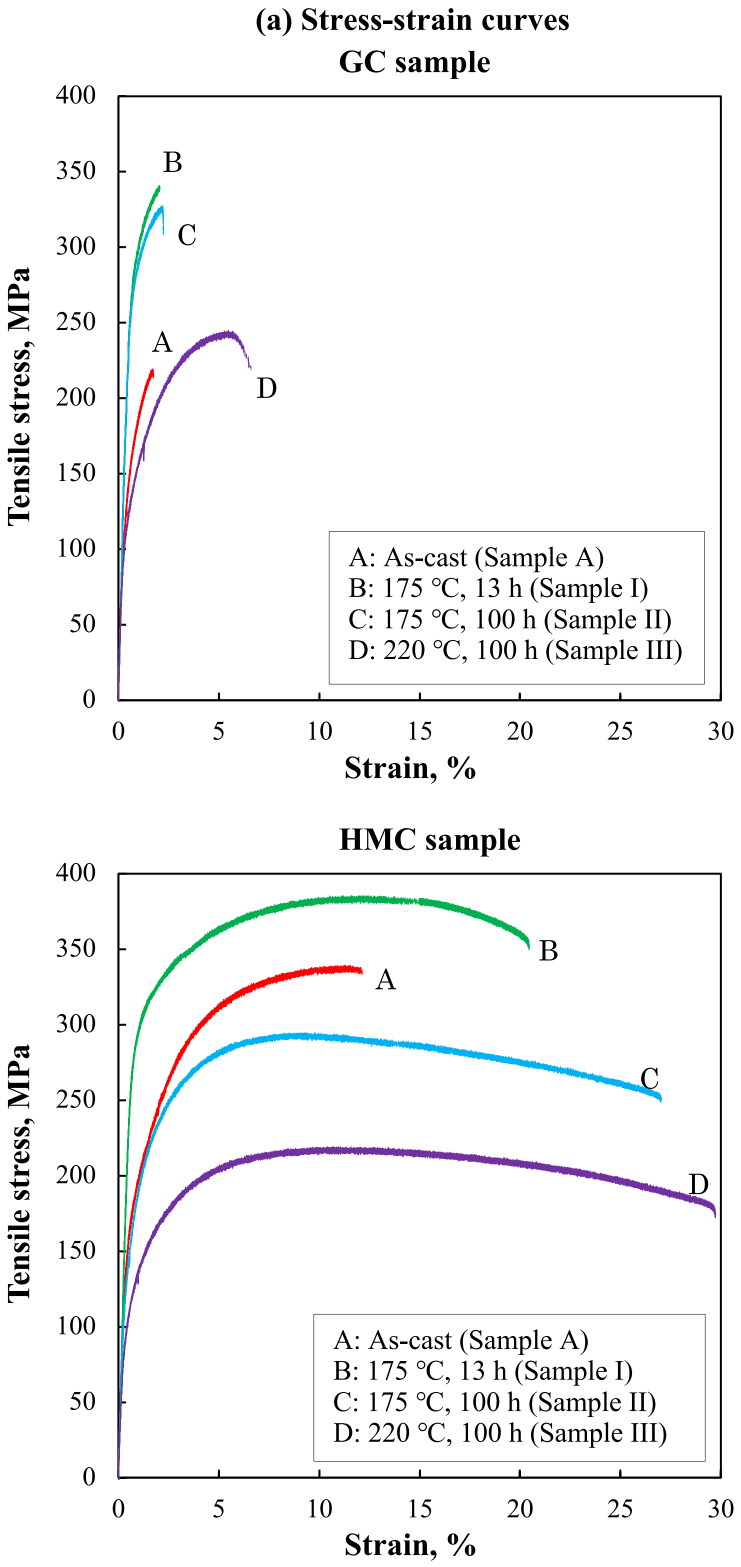

Fig. 4.8 Tensile properties of GC and HMC samples: (a) stress-strain curves; (b) tensile properties; (c) 0.2% proof strength; (d) fracture strain.

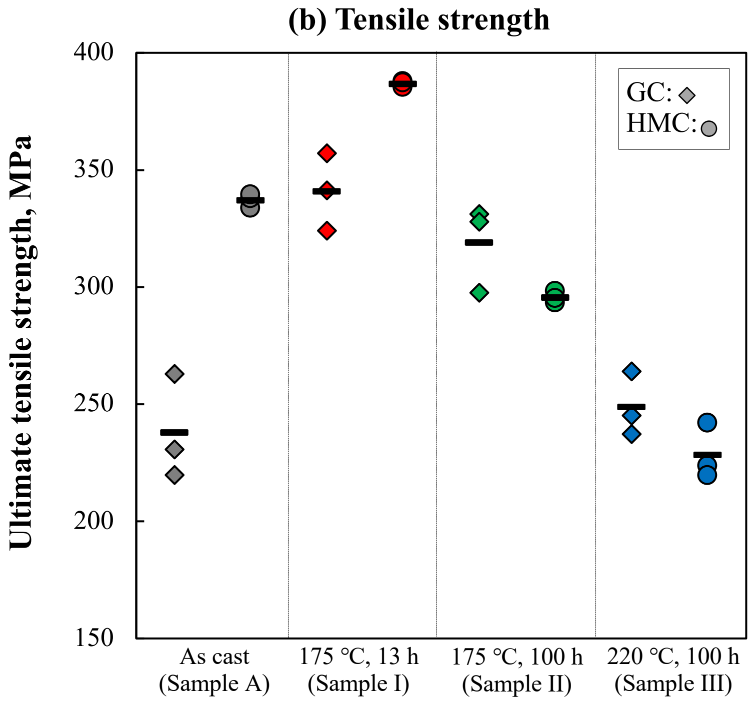
(b) Tensile strength
Ultimate tensile strength, MPa
400
350
300
250
200
150
GC:
HMC:
As cast (Sample A)
175 °C, 13 h (Sample I)
175 °C, 100 h (Sample II)
220 °C, 100 h (Sample III)

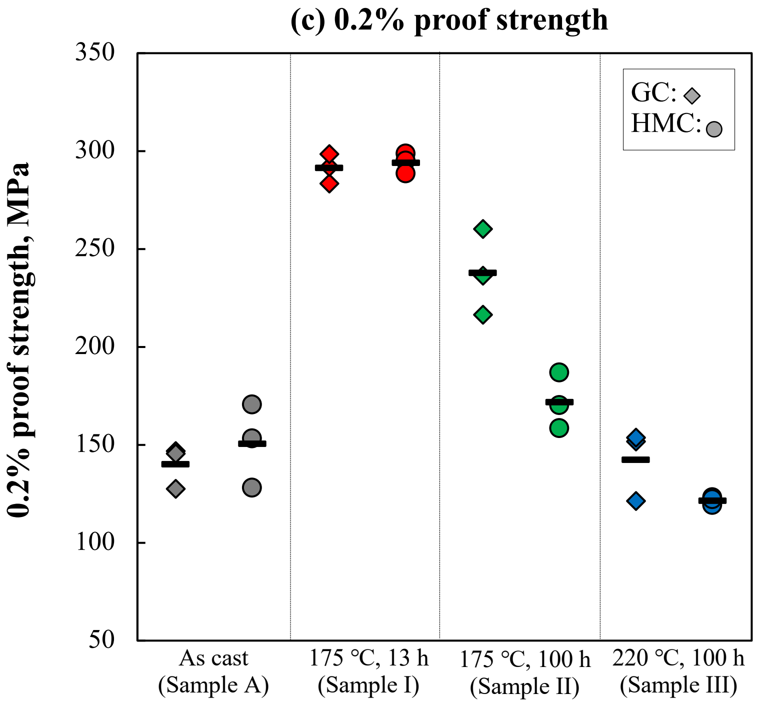
(c) 0.2% proof strength
0.2% proof strength, MPa
350
300
250
200
150
100
50
GC:
HMC:
As cast (Sample A)
175 °C, 13 h (Sample I)
175 °C, 100 h (Sample II)
220 °C, 100 h (Sample III)

Fig. 4.8 Cont.

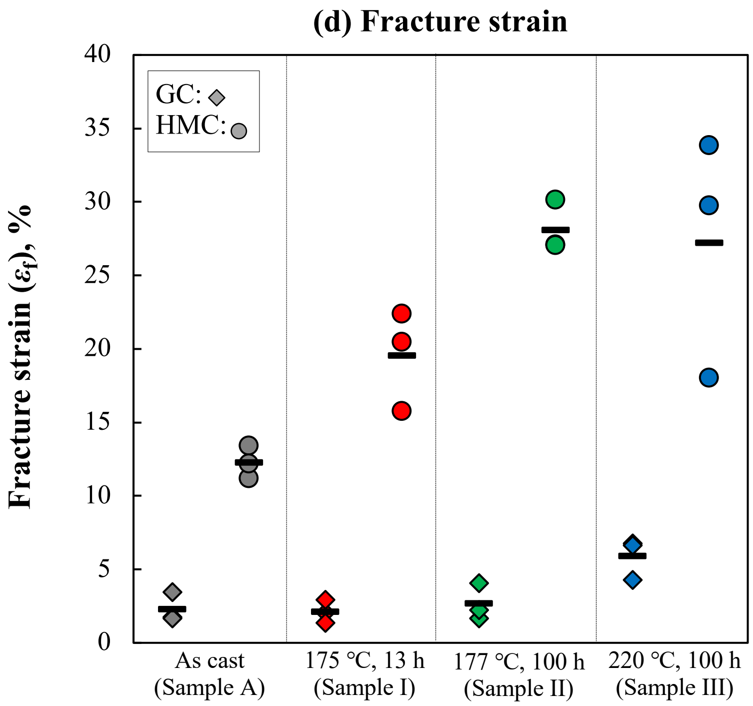

Fig. 4.8 Cont.

Similar to the UTS results, the 0.2% proof strength varies depending on the aging condition (Fig. 4.8(c)), and high $\sigma_{0.2}$ v values were obtained for both GC and HMC samples aged at 175 °C, for 13 h (sample I). The value of $\sigma_{0.2}$ seems to be correlated with the value of σ_{UTS}. Interestingly, the 0.2% proof strengths for GC and HMC samples under the same aging conditions are almost the same, particularly for GC sample A versus HMC sample A and for GC sample I versus HMC sample I, which is in contrast to the results for UTS. The reason is that the value of $\sigma_{0.2}$ is affected mainly by the extent of age precipitation and only weakly by microstructure formation (e.g., the sizes of α-Al grains and eutectic phases). However, due to the different $\sigma_{0.2}$ value for sample II, further study will be required. A related study was reported in Ref. [2], where the mechanical properties of several cast Al alloys with different sizes of microstructure (α-Al phase and eutectic structures) were investigated. In that study, the 0.2% proof strength values of the samples were all similar as a result of severe material damage occurring adjacent to grain boundaries and eutectic phases following severe plastic deformation.

In order to consider the results of the tensile test, the fracture surface was observed and shown in Fig. 4.9. Cleavage fracture surface morphology was entirely observed for the GC samples regardless of heat treatment conditions, and the fracture was brittle. On the other hand, the fracture surfaces of HMC samples shown a ductile fracture due to dimples. Compared to the as-cast sample, the shape of the dimples of HMC-sample I became rounder and grew even larger. It may be influenced by excellent ductility caused by the spherical eutectic phase because of the heat treatment, resulting in a relaxed stress concentration. Therefore, HMC-sample I showed excellent ductility despite its high strength.

<table>
<tr><th>GC</th><th>HMC</th></tr>
<tr><td colspan="2">(a) Sample A: as-cast</td></tr>
<tr><td>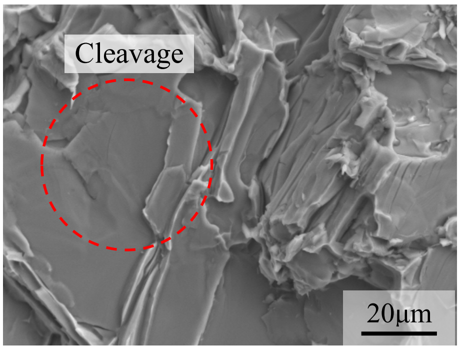 </td><td>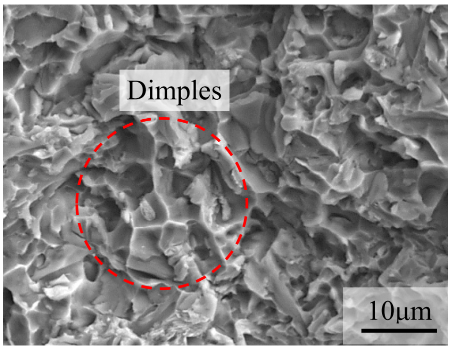 </td></tr>
<tr><td colspan="2">(b) Sample I: 175 °C, 13 h</td></tr>
<tr><td>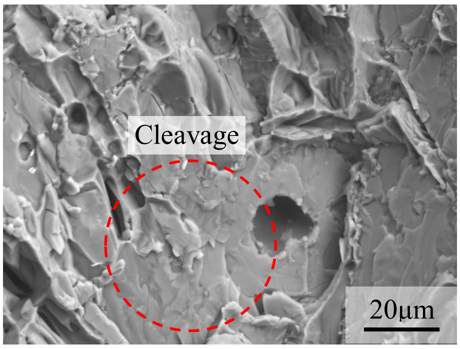 </td><td>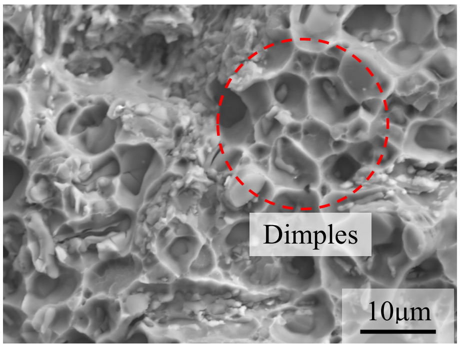 </td></tr>
<tr><td colspan="2">(c) Sample II: 175 °C, 100 h</td></tr>
<tr><td>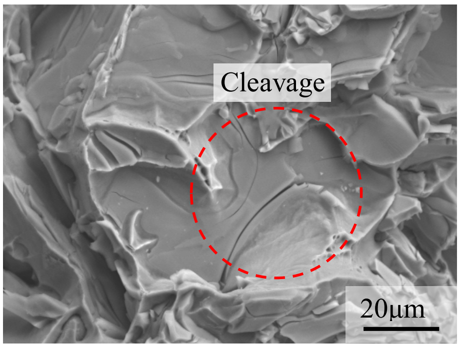 </td><td>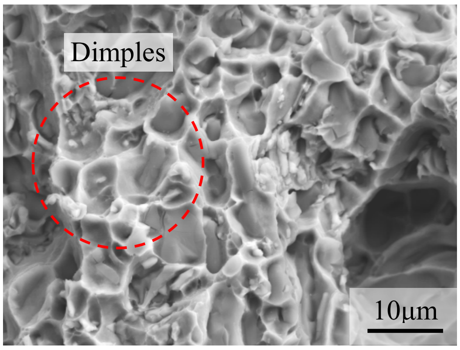 </td></tr>
</table>

Fig. 4.9 SEM images of fracture surfaces obtained by tensile test: (a) sample A (as-cast); (b) sample I (175 °C for 13h) and (c) sample II (175 °C for 100 h).

4.2.4 Fatigue properties

Figure 4.10 shows the relationship between stress amplitude S_a and fatigue life N_f for representative GC and HMC samples. In this case, 10^6 cycles are determined as the endurance limit σ_e, which is indicated by the arrows in Fig. 4.10. One specimen was tested in each loading condition, as the fatigue data obtained was relatively stable. It can be seen that the fatigue strength of HMC sample A (σ_e = 83 MPa) is higher than that of GC sample A (σ_e = 70 MPa). This shows a similar trend to the tensile strength. The S_a-N_f curve for HMC sample I lies above those for the other HMC samples and all GC samples. The fatigue strength of HMC sample A is almost the same as that of HMC sample II, and their S_a-N_f curves almost coincide with those for GC sample I. On the other hand, the fatigue properties of both GC and HMC sample III are at a lower level. To quantify the fatigue strength, the S_a-N_f relationship is evaluated using the Basquin equation as follows:

$$S_a = \sigma_f N_f^b \quad \text{(MPa)}, \tag{4.1}$$

where σ_f (in MPa) is the fatigue strength coefficient and b is the fatigue strength exponent. In this case, it is expected that the fatigue life will be longer as the fatigue strength coefficient increases. It should be noted first that the above parameters are approximated based on the power-law dependence of the applied repetitive stress on the number of cycles to final failure shown by the dashed curve in Figure 4.10. The σ_f values for the cast samples are shown in Table 4.1. This estimation also verified that the HMC sample aged at 175 °C, for 13 h (HMC sample I) has excellent fatigue strength. It has been reported previously [2] that high fatigue properties are obtained for the HMC-ADC12 alloy, which is made at a high casting speed of 7.5 mm·s^{-1}, because of the high cooling rate, but are not as high as those for the HMC sample I showed in Fig. 4.10.

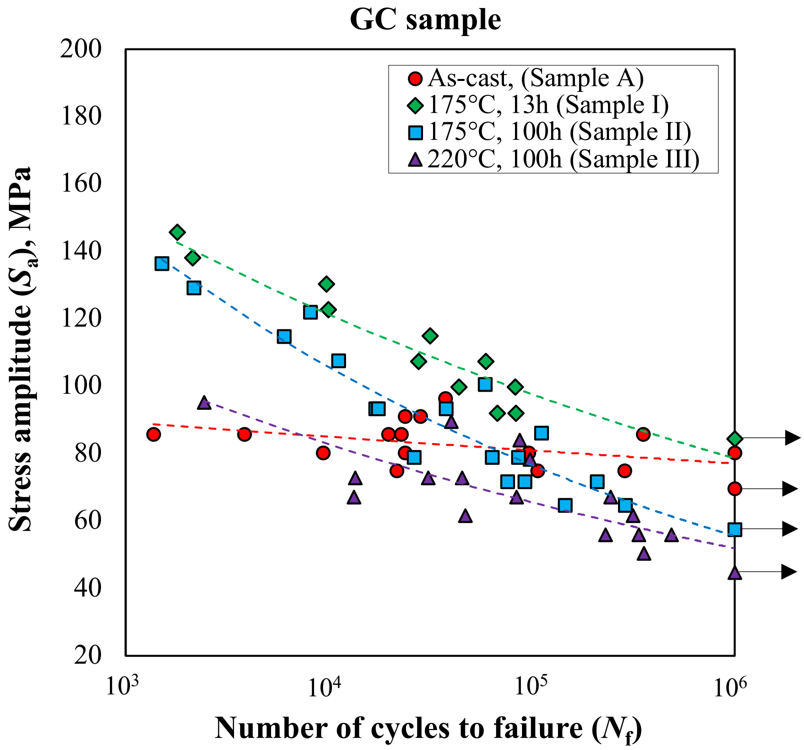

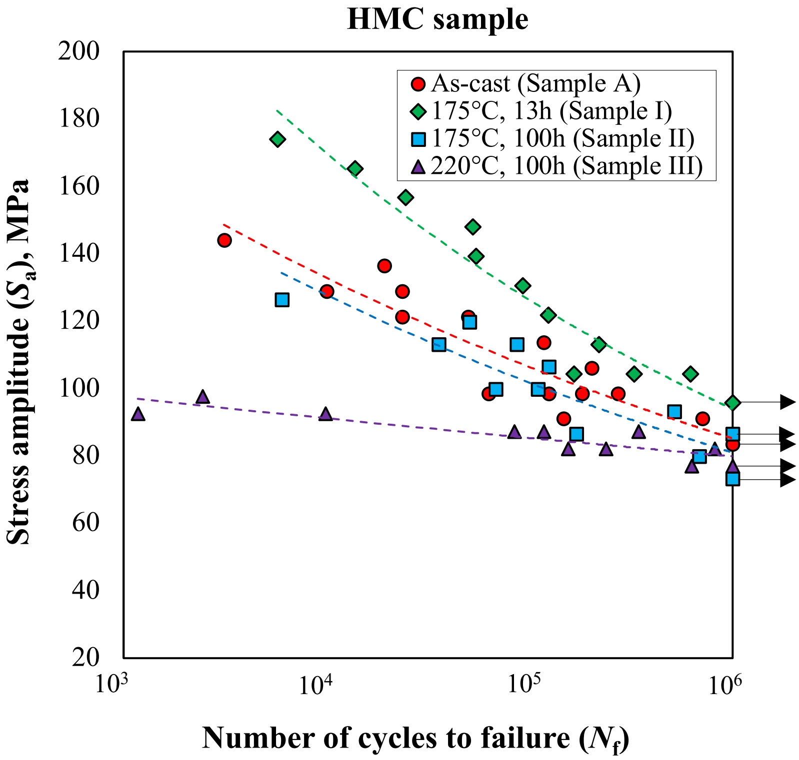

Fig. 4.10 S_a-N_f curves of GC and HMC samples: sample A; sample I, sample II, and sample III.

Table 4.1 Fatigue strength coefficient σ_f for GC and HMC sample: sample A, sample I, sample II and sample III.

		As-cast (Sample A)	175 °C, 13 h (Sample I)	175 °C, 100 h (Sample II)	220 °C, 100 h (Sample III)
Fatigue strength coefficient σ_f, MPa	GC	103.5	231.2	382.1	210.9
	HMC	322.7	554.2	317.2	118.8

The relationship between fatigue strength and tensile properties for both GC and HMC samples was analyzed to understand further the fatigue properties described above. Fig. 4.11 shows the results for (a) σ_f versus $\sigma_{0.2}$, (b) σ_f versus σ_{UTS}, (c) σ_f versus ε_f and (d) σ_{UTS} versus $\sigma_{0.2}$. Since the fatigue properties are directly related to the region of macroscopic elastic deformation, there is a linear correlation between $\sigma_{0.2}$ and σ_f at $\sigma_f = 1.42\sigma_{UTS} + 4.67$(correlation rate $R^2 = 0.46$). It is interesting to mention that although σ_{UTS} is associated with relatively large plastic strain, a similar linear relationship is obtained between σ_{UTS} and σ_f, Fig. 4.11(b). The reason behind this is not apparent at the moment, but this would be related to the linear correlation between $\sigma_{0.2}$ and σ_{UTS}, see Fig. 4.11(d). In contrast, a weak trend is detected for the results for fracture strain ε_f versus σ_f ($R^2 = 0.03$), see Fig. 4.11(c). It follows from this that the tensile strengths can play an important role in influencing fatigue properties.

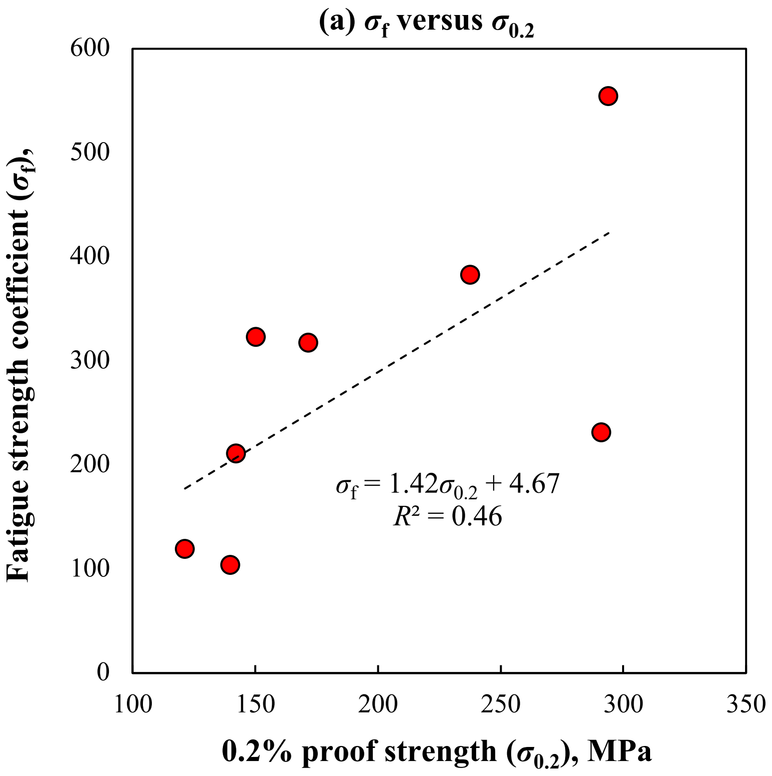
(a) σ_f versus $\sigma_{0.2}$

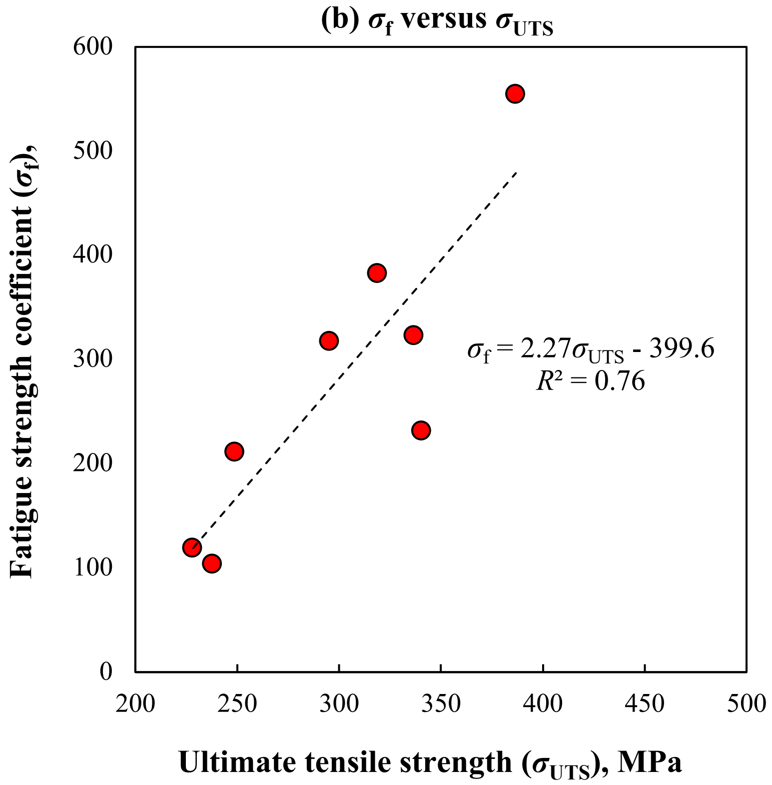
(b) σ_f versus σ_{UTS}

Fig. 4.11 Relationship between fatigue properties and tensile properties of GC and HMC samples: (a) σ_f versus $\sigma_{0.2}$; (b) σ_f versus σ_{UTS}; (c) σ_f versus ε_f; (d) σ_{UTS} versus $\sigma_{0.2}$.

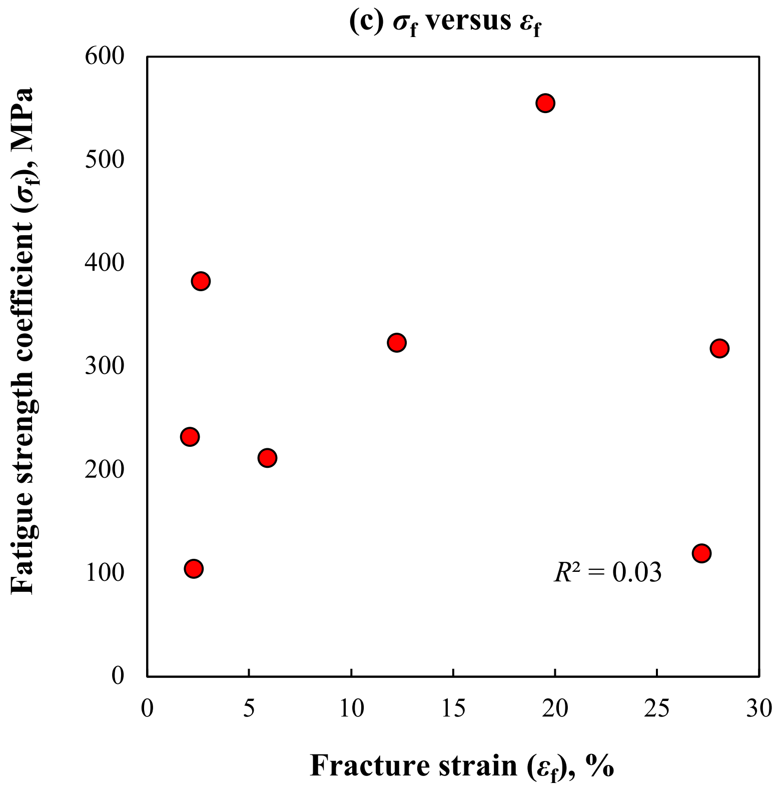
(c) σ_f versus ε_f

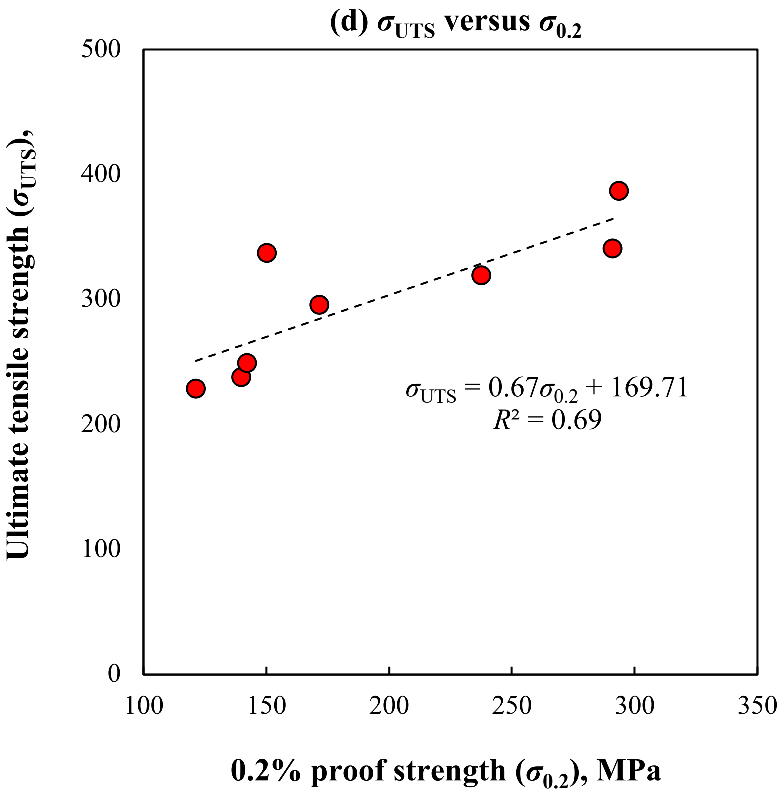
(d) σ_{UTS} versus $\sigma_{0.2}$

Fig. 4.11 Cont.

4.2.5 TEM analysis

TEM observations were performed to understand the effect of microstructural properties on mechanical properties, and the resulting images are shown in Figure 4.12. From the TEM images of the GC and HMC samples (Fig. 4.12 (a)), the dislocation walls and dislocation cells clearly intersect in the complex pattern of GC sample A [12]. In contrast, sub micrometer-sized particles and fine dislocation cells are observed in HMC sample A. From the TEM-EDX analysis in the α-Al phases, a large amount of Cu, Si, Mg and Fe, solidified within the α-Al matrix, is detected in GC sample A, at a higher level than that in HMC sample A: 3 mass% Cu versus 0.3 mass% Cu; see Fig. 4.13. It might be assumed that the complex dislocation walls and the high solubility of the chemical elements inα-Al grains explain the high hardness of GC sample A (Fig. 4.6). As with the as-cast samples, many elements are seen in the aged GC samples compared with the aged HMC samples. The high chemical content of aged GC samples is not clear at this time, but it is also related to the results of hardness measurements. On the other hand, the high tensile strength of HMC sample A is influenced by small α-Al particles of sub micrometer size, and the low tensile strength of GC sample A is mainly due to the presence of large brittle eutectic structures.

It can be observed in the TEM images of GC sample I and HMC sample I (Fig. 4.12(b)) that there is high-density fine precipitation of the θ'(Al$_2$Cu) metastable phase in HMC sample I, where the average size of the plate-like Al$_2$Cu is 100 × 3 nm^2 in the α-Al matrix. This is expected to provide the strengthening mechanism for the related aluminum alloy, namely precipitation hardening. On the other hand, coarsening of the θ'(Al$_2$Cu), i.e., to 50 × 10 nm^2, is seen in GC sample I. Such thick θ'(Al$_2$Cu) phases are also seen in both GC sample II and HMC sample II (Fig. 4.12(c)), where these phases are precipitated with higher density as a result of over-aging. This precipitation behavior could weaken the precipitation hardening of the aluminum alloy.

GC	HMC
(a) Sample A: as-cast	
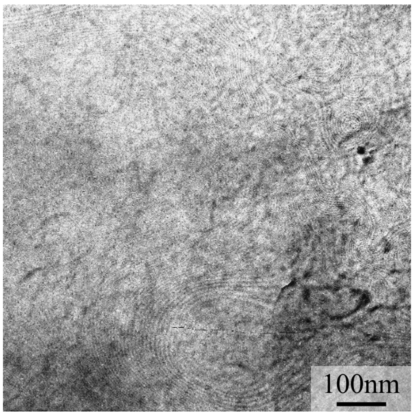	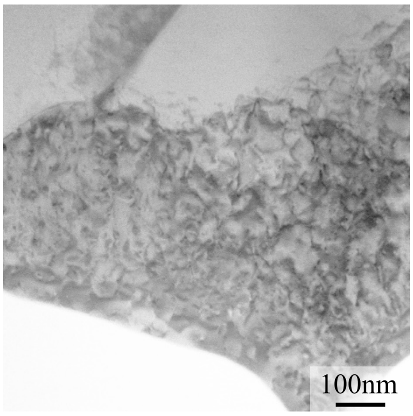
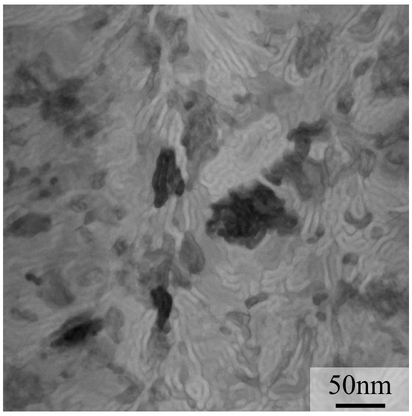	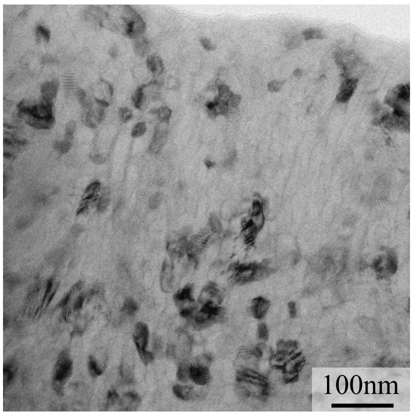

Fig. 4.12 TEM images of GC and HMC samples: (a) sample A; (b) sample I; (c) sample II.

GC	HMC
(b) Sample I: 175 °C, 13 h	
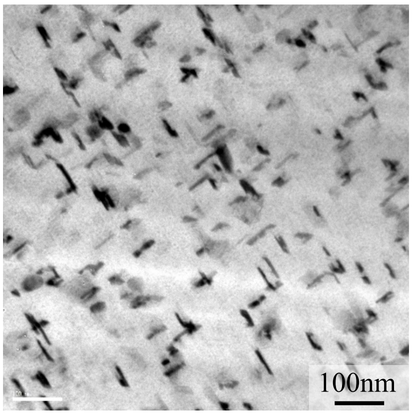	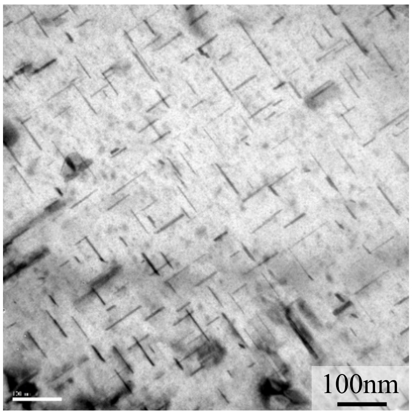
(c) Sample II: 175 °C, 100 h	
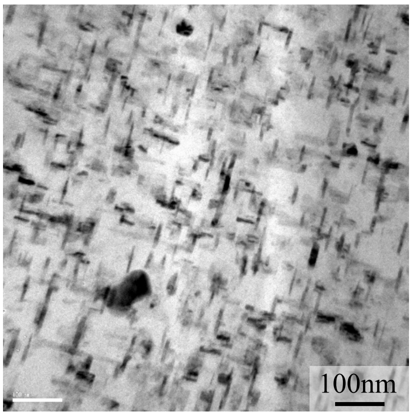	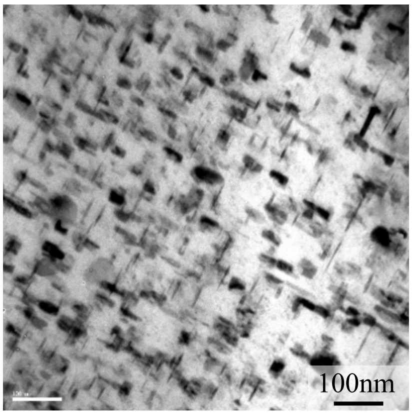

Fig. 4.12 Cont.

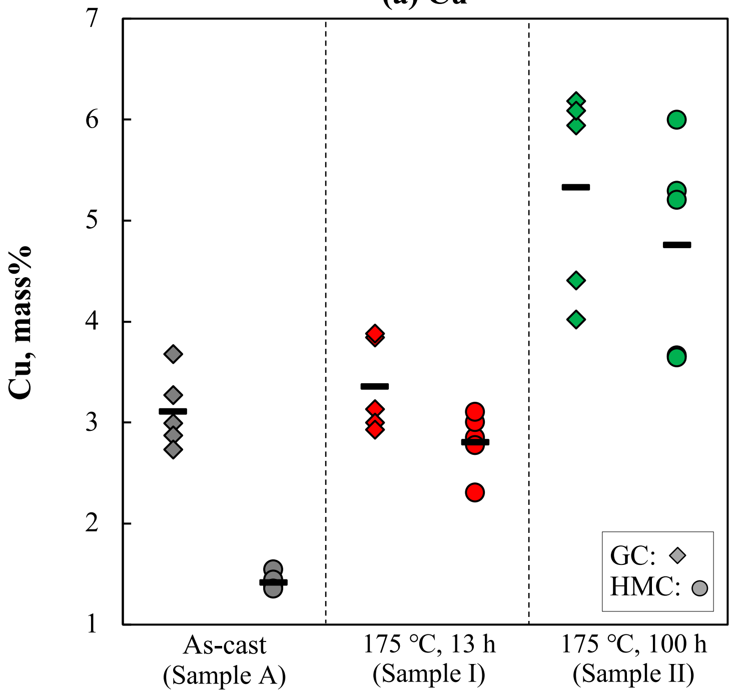
(a) Cu

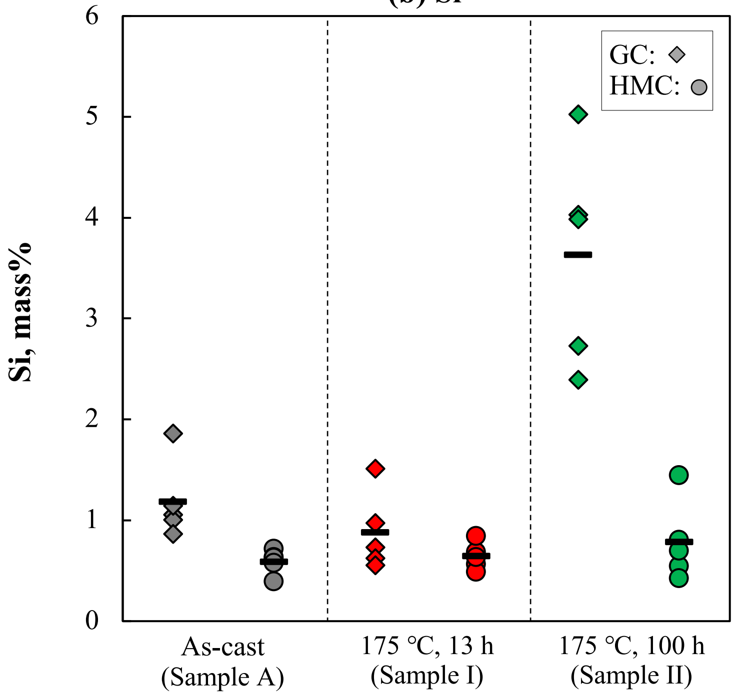
(b) Si

Fig. 4.13 Amount of Cu, Si, Mg and Fe in the *α*-Al phase for GC and HMC samples.

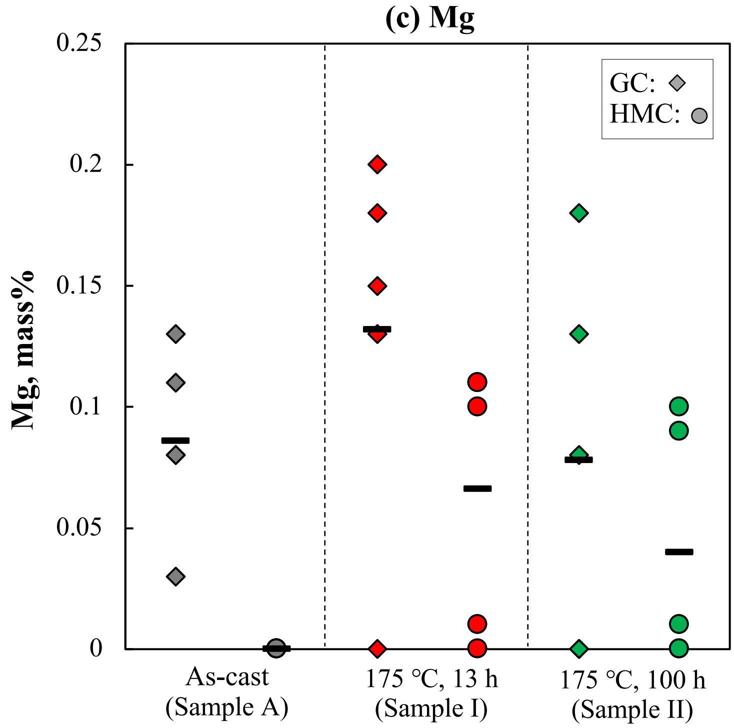
(c) Mg
Mg, mass%
0.25
0.2
0.15
0.1
0.05
0
GC: ◆
HMC: ●
As-cast
(Sample A)
175 °C, 13 h
(Sample I)
175 °C, 100 h
(Sample II)

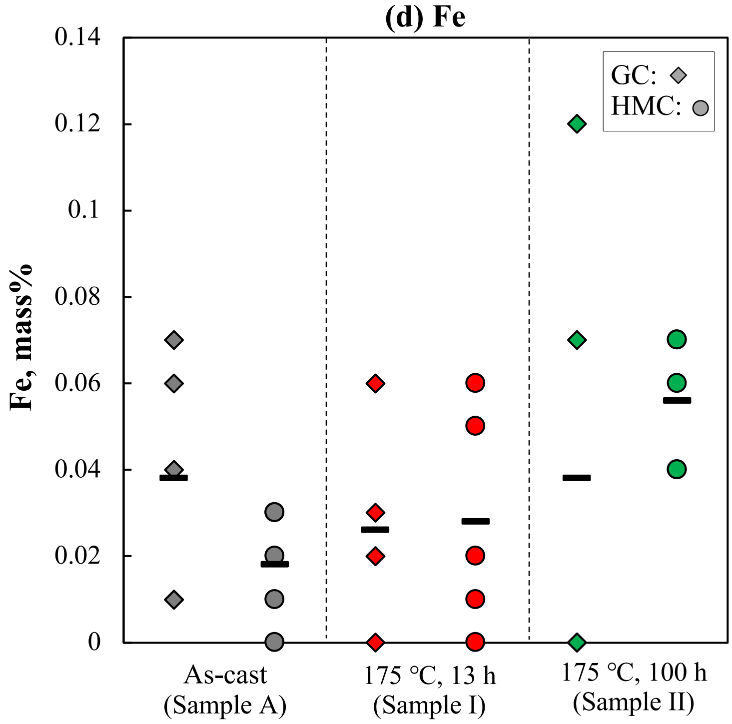
(d) Fe
Fe, mass%
0.14
0.12
0.1
0.08
0.06
0.04
0.02
0
GC: ◆
HMC: ●
As-cast
(Sample A)
175 °C, 13 h
(Sample I)
175 °C, 100 h
(Sample II)

Fig. 4.13 Cont.

4.3 Summary

The effect of artificial aging on the mechanical properties of cast Al-Si-Cu-based aluminum alloys has been experimentally studied. The results can be summarized as follows:

1) The Vickers hardness of the GC samples was higher overall than that of the HMC samples both before and after aging. The high hardness of GC was due to the high solubility of the alloying elements (Cu, Si, Mg and Fe) in the α-Al matrix and the presence of complicated dislocation walls. The hardness of GC and HMC samples aged at 160, 175, and 190 ° C increased with increasing aging time, with aging peaks on the 10-15 h aging hardening curve.

2) The UTS of the as-cast HMC sample was about 30% higher than that of the as-cast GC sample, and the highest UTS was obtained with the HMC sample aged at 175 ° C for 13 h. The high UTS value of the HMC sample is due to the fine precipitation of the θ' (Al_2Cu) metastable phase and the formation of tiny microstructures. With over-aging at 190 ℃ and 220 ℃ for 100 h, the fracture strain for HMC samples increased considerably to 30%. On the other hand, there was no apparent improvement in material ductility for GC samples because of large brittle eutectic structures.

3) UTS in both GC and HMC samples may be directly due to fatigue intensity, but no significant effect of ductility on fatigue properties was detected. There was a linear correlation between the UTS and the fatigue strength coefficient σ_f, but no clear trend was detected in the fracture strain versus σ_f results.

References

1. A. Ohno, Solidification, 1st ed. Springer. Germany, (1987)113-118.

2. M. Okayasu, S. Takeuchi, M. Yamamoto, H. Ohfuji, T. Ochi, Precise analysis of microstructural effects on mechanical properties of cast ADC12 aluminum alloy, Metall. Mater. Trans. A, 46(2015)1597-1609.

3. R.N. Lumley, I.J. Polmear, P.R. Curtis, Rapid heat treatment of aluminum high-pressure diecastings, Metall. Mater. Trans. A, 40A(2009)1716-1726.

4. D. Mohr, R. Treitler, Onset of fracture in high pressure die casting aluminum alloys, Eng. Fract. Mech., 75(2008)97-116.

5. R.X. Li, R.D. Li, Y.H. Zhao, L.Z. He, C.X. Li, H.R. Guan, Z.Q. Hu, Age-hardening behavior of cast Al-Si base alloy, Mater. Lett., 58(2004)2096-2101.

6. Kh.A. Ragab, A.M. Samuel, A.M.A. Al-Ahmari, F.H. Samuel, H.W. Doty, Influence of fluidized sand bed heat treatment on the performance of Al-Si cast alloys, Mater. Design, 32(2011)1177-1193.

7. M. Okayasu, K. Ota, S. Takeuchi, H. Ohfuji, T. Shiraishi, Influence of microstructural characteristics on mechanical properties of ADC12 aluminum alloy, Mater. Sci. Eng., 592(2014)189-200.

8. M. Okayasu, S. Takasu, M. Mizuno, Relevance of instrumented nano-indentation for the assessment of the mechanical properties of eutectic crystals and α-Al grain in cast aluminum alloys, J. Mater. Sci., 47(2012)241-250.

9. E. Sjölander, S. Seifeddine, The heat treatment of Al-Si-Cu-Mg casting alloys, J. Mater. Process. Technol., 210(2010)1249-1259.

10. M. Furui, T. Kitamura, T. Ishikawa, S. Ikeno, S. Saikawa, N. Sakai, Evaluation of age hardening behavior using composite rule and microstructure observation in Al-Si-Mg alloy castings, Mater. Trans., 52(2011)1163-1167.

11. R.N. Lumley, N. Deeva, R. Larsen, J. Gembarovic, J. Freeman, The role of alloy composition and T7 heat treatment in enhancing thermal conductivity of aluminum high pressure diecastings, Metall. Mater. Trans. A, 44A(2013)1074-1086.

12. X.W. Li, Y. Zhou, W.W. Guo, G.P. Zhang, Characterization of dislocation structures in [111] copper single crystals using electron channelling contrast technique in SEM, Cryst. Res. Technol., 44(2009)315-321.

Chapter 5 Effects of Sb, Sr and Bi on the Material Properties of Al-Si-Cu Foundry Alloy

5.1 Experimental procedures

5.1.1 Material preparation

A cast aluminum alloy, ADC12 (Al-10.6Si-2.5Cu), with the addition of several rare earth (RE) metals (Sr, Sb and Bi) was utilized. Based on a previous study [1], the amount of RE metals was determined to be 0.02-0.06Sr, 0.25-0.75Sb and 0.5-1.5Bi.

Cast ADC12 samples were created in two different methods, namely, HMC and GC. HMC samples were created using an HMC device consisting of a melting furnace, a graphite mold, a graphite crucible, and a water cooling device [2]. Small blocks of ADC12 ingot were melted in the graphite crucible by the furnace at a temperature of 635 °C, which is slightly higher than the melting point of ADC12 alloy. Flux treatment was performed in the liquid state of ADC12 before the casting process to remove inclusions in the casting sample. The molten metal was continuously fed at 1.9 mm·s^{-1} from the heated graphite mold through the use of a dummy rod to the outside using a motor-driven system. The Casting samples were continuously produced under cooling with water droplets. The casting sample was designed with a ϕ5 mm × 1000 mm round bar.

To clearly understand the mechanical properties of the HMC-ADC12-RE alloy, we compared their material properties with those of the same aluminum alloy made by GC. The molten aluminum alloy was poured directly into a ϕ60×80 mm sand mold in the GC process. The melting temperature of the aluminum alloy in the GC process was designed to be approximately equal to the melting temperature in the HMC process.

5.1.2 Material properties

Tensile properties were examined experimentally at room temperature using an electro-servo-hydraulic system with 50 kN capacity. This approach employed dumbbell-shaped test specimens with ϕ2 mm dimension and 10 mm gauge length. The tensile properties were evaluated via tensile stress versus tensile strain curves, which were monitored by a data acquisition system with a computer through a standard load cell and a commercial strain gauge. The loading velocity in the tensile test was 1 mm·min^{-1} to the fracture point. A microstructural observation was executed with an optical microscope and a scanning electron microscope. In addition, the lattice structures of the aluminum alloys were examined through electron back scattering diffraction (EBSD) analysis.

5.2 Results and discussion

5.2.1 Microstructure characteristics

Figure 5.1 shows the microstructures of the ADC12-RE alloys produced through GC and HMC. The size of the α-Al phase (SDAS) for HMC is smaller than that for GC, SDASGC = Ave. 7.41 mm (Standard deviation (SD): 0.315 mm) and SDASHMC = Ave. 32.9 mm (SD: 2.76 mm) because of the high cooling rate in the HMC process. The eutectic Si structures are refined for all

HMC samples with RE metals. Microstructural analysis was conducted to understand the characteristics of the eutectic Si structures clearly.

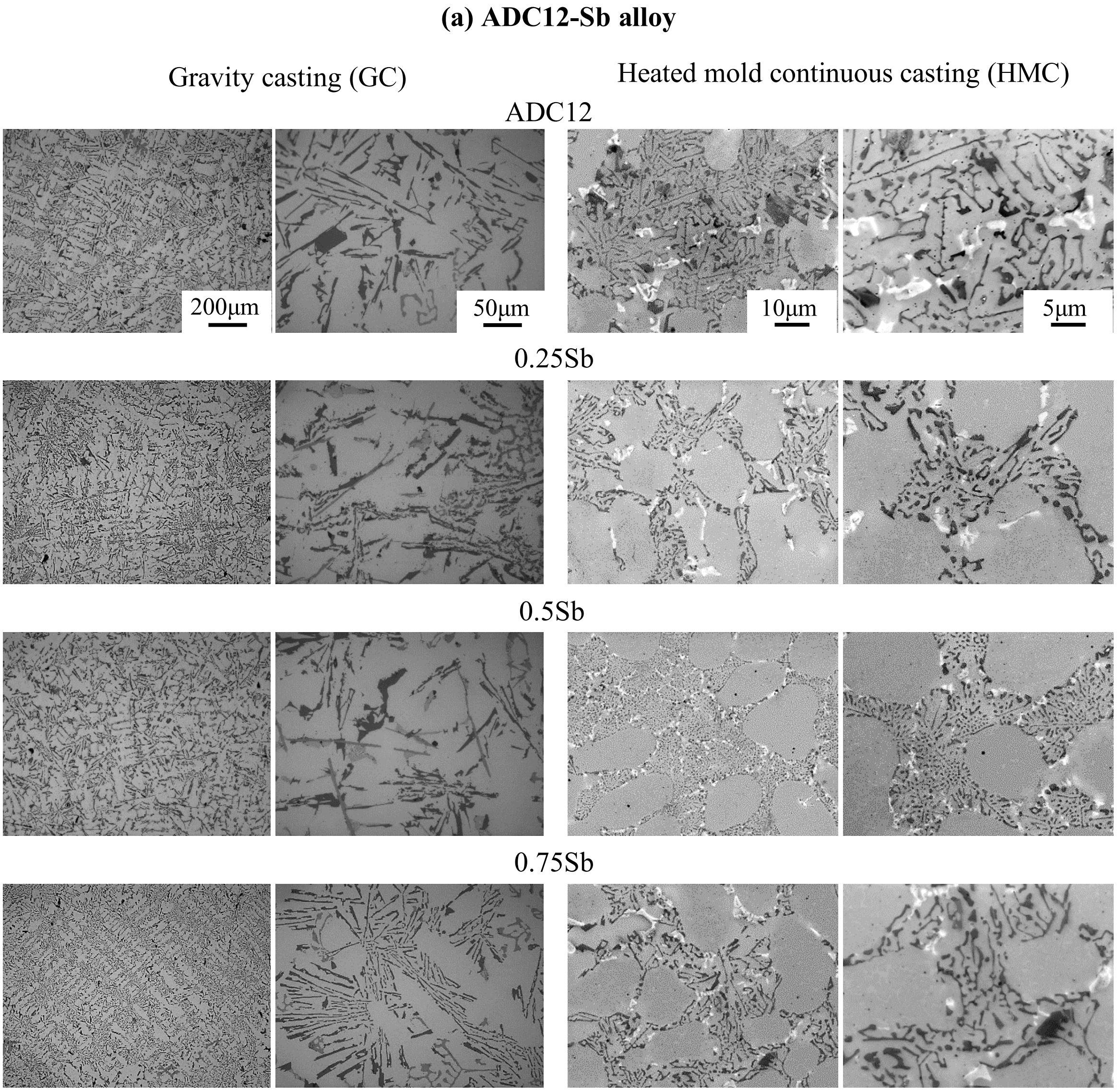

Fig.5.1 Microstructural characteristics of the HMC and gravity cast aluminum alloys: (a) ADC12-Sb; (b) ADC12-Sr; (c) ADC12-Bi.

(b) ADC12-Sr alloy

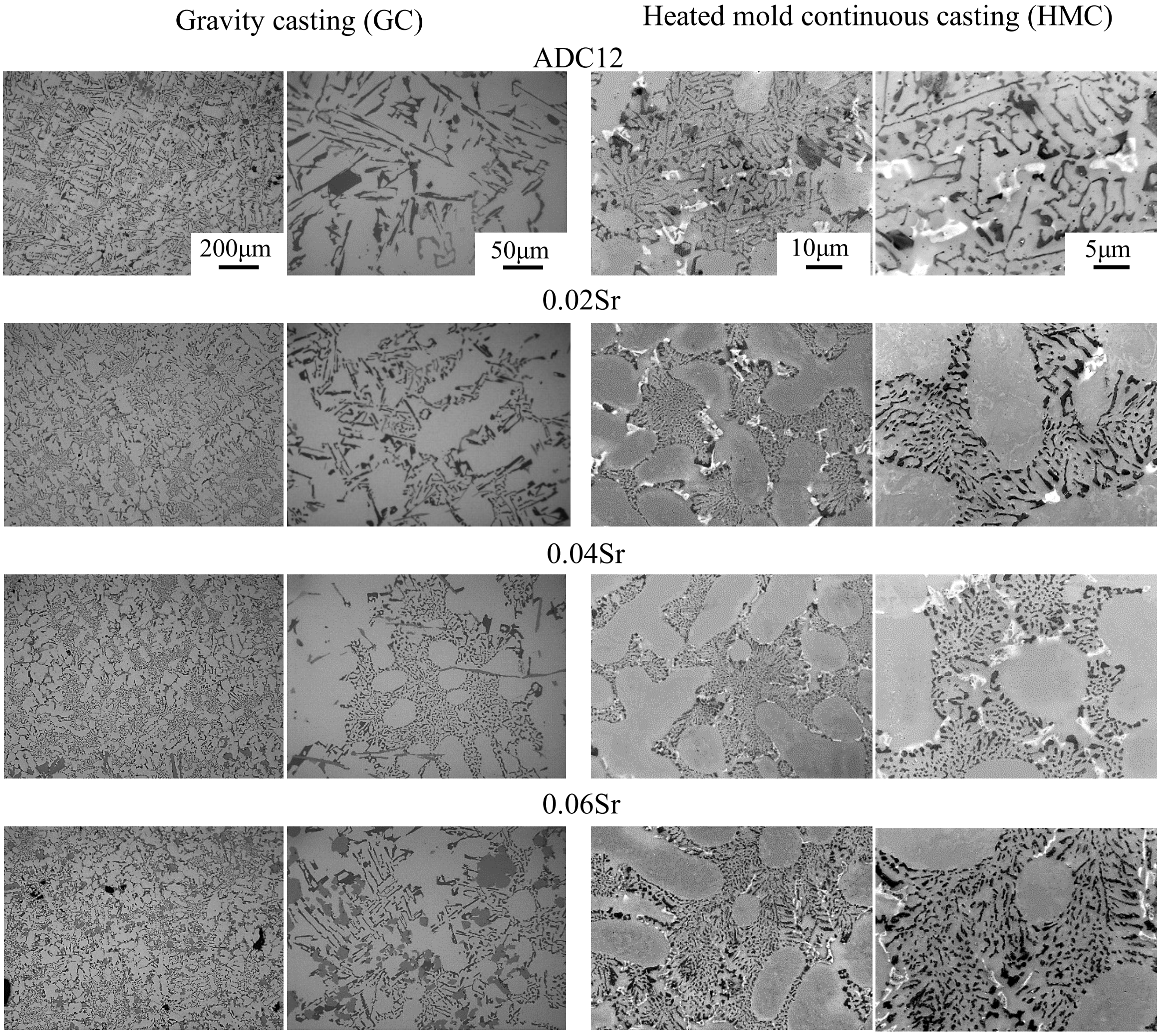

Fig.5.1 Cont.

(c) ADC12-Bi alloy

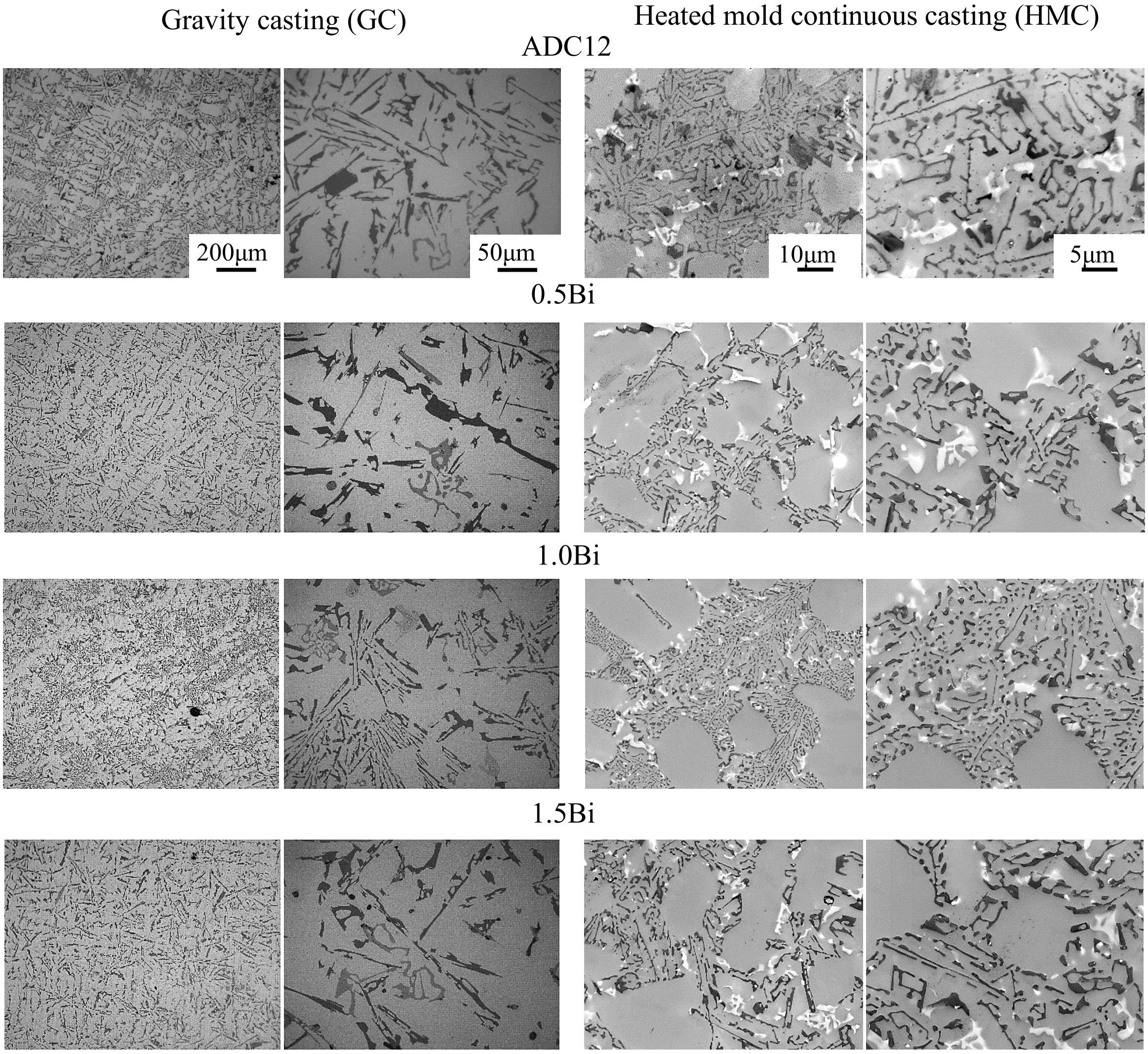

Fig.5.1 Cont.

Figure 5.2 shows the size (*SZ*) and aspect ratio (*AS*) of the eutectic Si phase of the HMC-ADC12-RE alloy evaluated with over 300 eutectic Si phases. In this case, the eutectic Si phase with an area greater than 0.03 mm^2 observed on the sample surface was selected. Delicate eutectic Si phases were obtained by adding the RE metal elements to the HMC samples (0.5Sb, 0.02Sr, 0.04Sr and 1.0Bi). The size of the Si phase is less than 0.2 mm^2. A low aspect ratio of Si particles was obtained for the ADC12-0.04Sr alloy (e.g., $AS = 2.19$). The eutectic phases for the others, such as 0.5-0.75Sb and 0.5-1.5Bi, were formed with lamellar shapes (more than $AS = 2.51$). Such eutectic Si phase characteristics were similarly obtained in previous related work [1]. In this case, RE metal additions reduce the nucleation and growth temperature of Al-Si eutectic phases. The different eutectic Si characteristics between ADC12-Sr and ADC12-Sb (or Bi) may be attributed to the different severity degrees of recalescence, namely, Bi and Sb cause an increase in recalescence with increased cooling rate, whereas Sr causes a reduction in recalescence [1]. For the GC samples shown in Fig. 5.1, refinement of the eutectic Si phase was not clearly observed compared with that for HMC, whereas tiny Si particles and fibrous Si morphology are created for GC-ADC12-0.04Sr and -0.75Sb, respectively. The as-cast microstructures of Al-Si with or without 0.03Sr consist of a coarse acicular plate of eutectic Si in the α-Al matrix but with different sizes and morphologies [3].

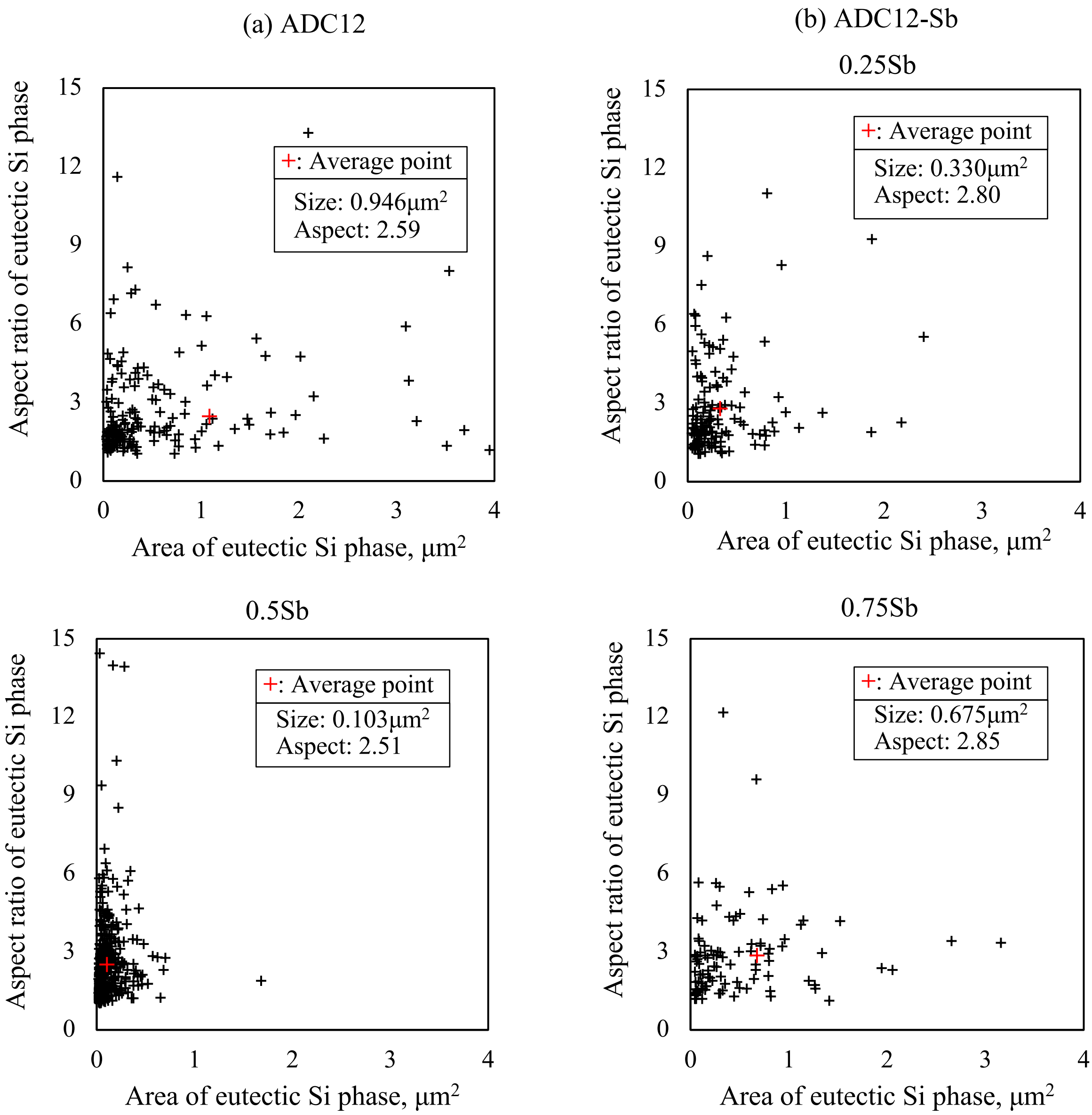

Fig.5.2 Relationship between the size (*SZ)* and aspect ratio (*AS*) of eutectic Si phases for (a) ADC12; (b) ADC12-Sb; (c) ADC12-Sr; (d) ADC12-Bi.

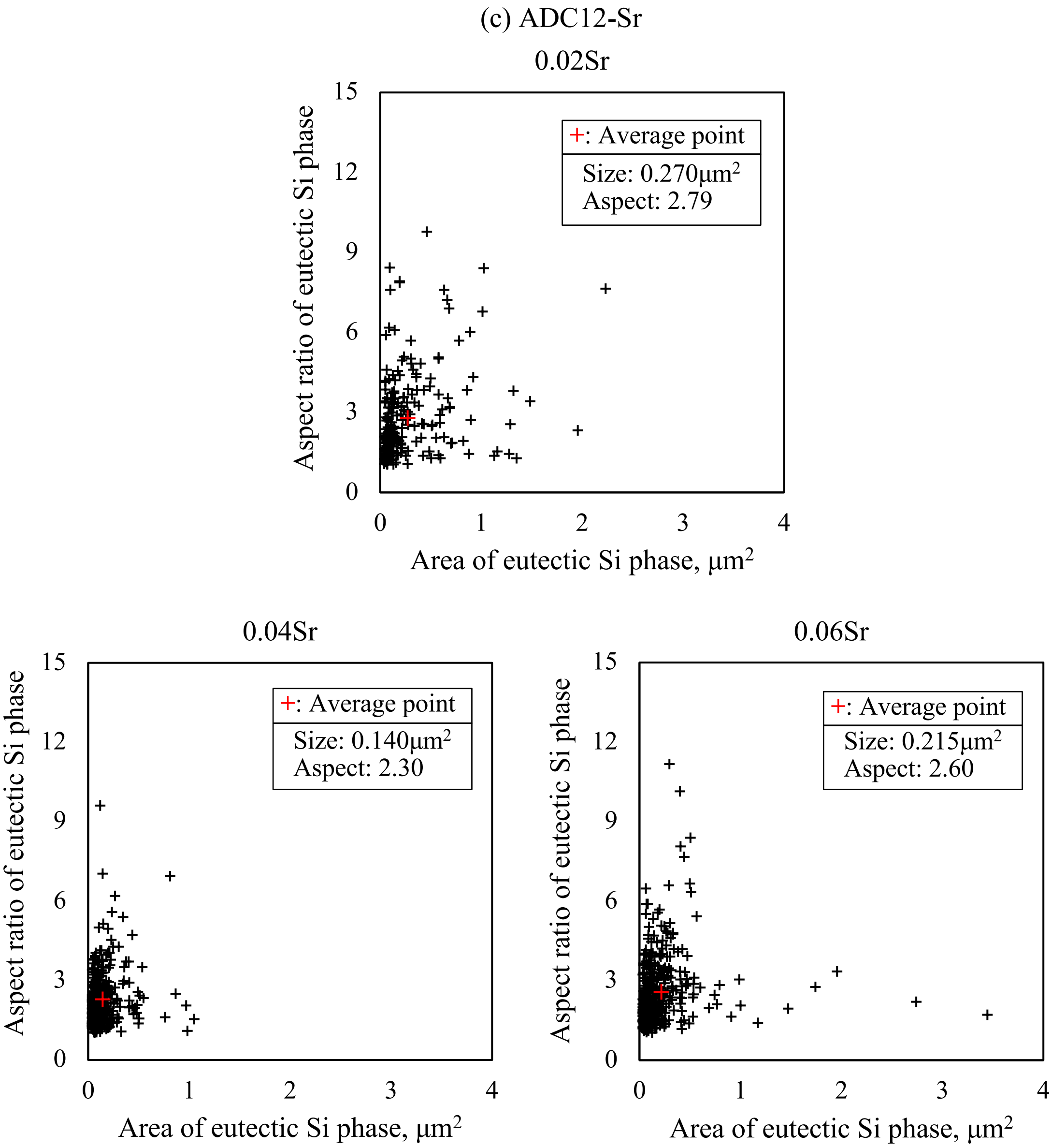
(c) ADC12-Sr
0.02Sr
+: Average point
Size: 0.270μm²
Aspect: 2.79
0.04Sr
+: Average point
Size: 0.140μm²
Aspect: 2.30
0.06Sr
+: Average point
Size: 0.215μm²
Aspect: 2.60
Aspect ratio of eutectic Si phase
Area of eutectic Si phase, μm²
0
3
6
9
12
15
0
1
2
3
4

Fig. 5.2 Cont.

(d) ADC12-Bi

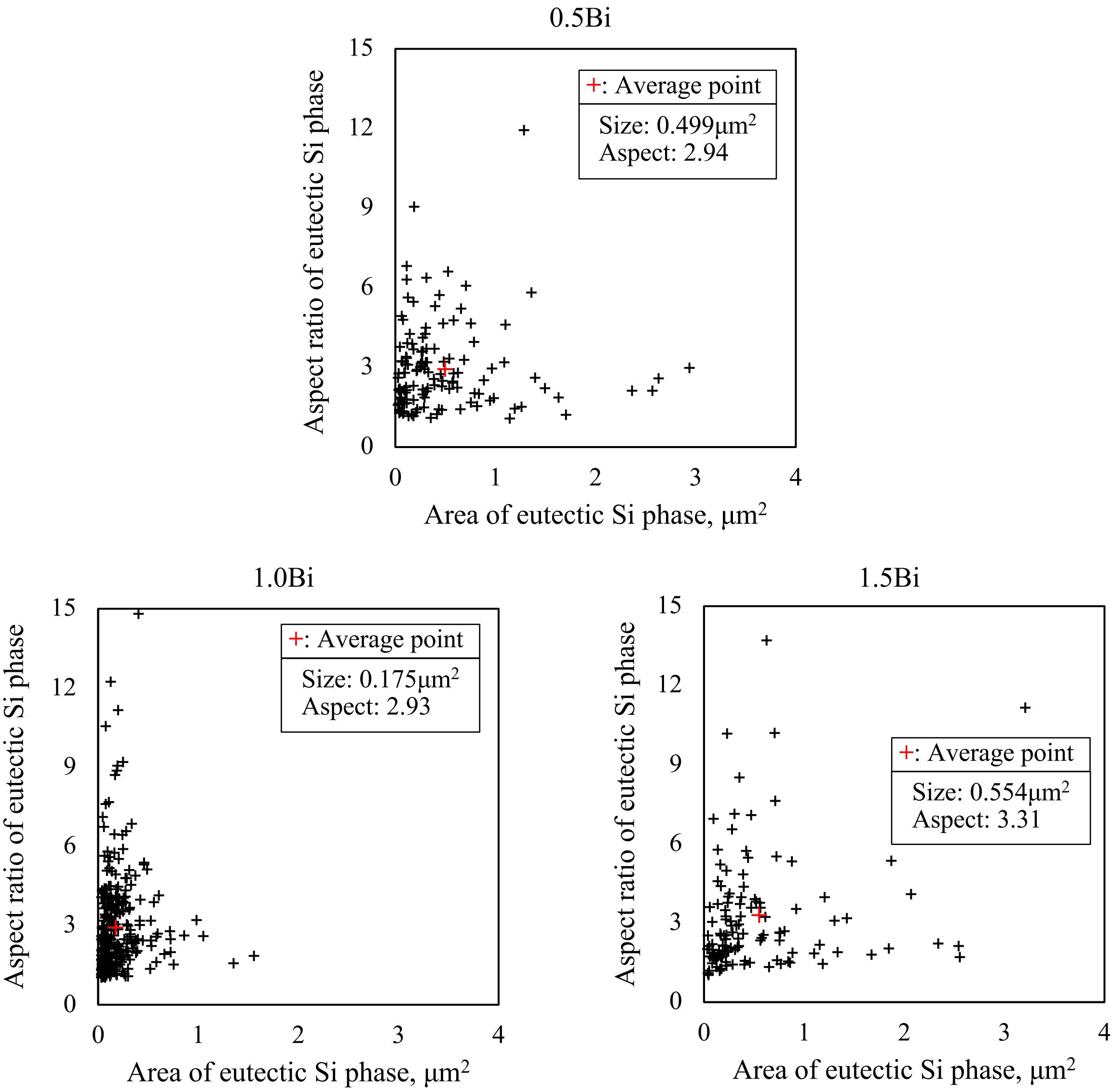

Fig. 5.2 Cont.

The crystal orientation of each HMC sample was investigated through EBSD analysis to understand the microstructural characteristics further. Figure 5.3 shows the crystal orientation map (IPF) of the HMC-ADC12 alloy. A uniformly organized crystal formation with the [100] direction was obtained for the HMC-ADC12 alloy and a low proportion of RE metal. This occurrence is affected by the unidirectional solidification state in the casting process. The change in the dynamics of the alloying atoms from liquid to solid is affected by the less closely packed plane because of the lower energy state [4]. When RE metal increased in the ADC12 alloys, their crystal orientations collapsed, thereby. exhibiting a random lattice formation (e.g., ADC12-0.04Sr and -1.5Bi). This phenomenon could be affected by the fact that interruption of the columnar α-Al grain growth occurred as a result of the different dynamics of alloying atoms and the creation of a core for eutectic structures. Consideration should be given as to whether microstructures affect the mechanical properties in our cast sample.

HMC samples

(a) ADC12

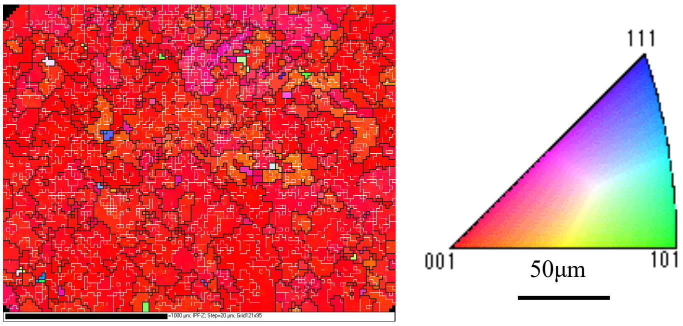

(b) ADC12-Sb

0.25Sb 0.5Sb 0.75Sb

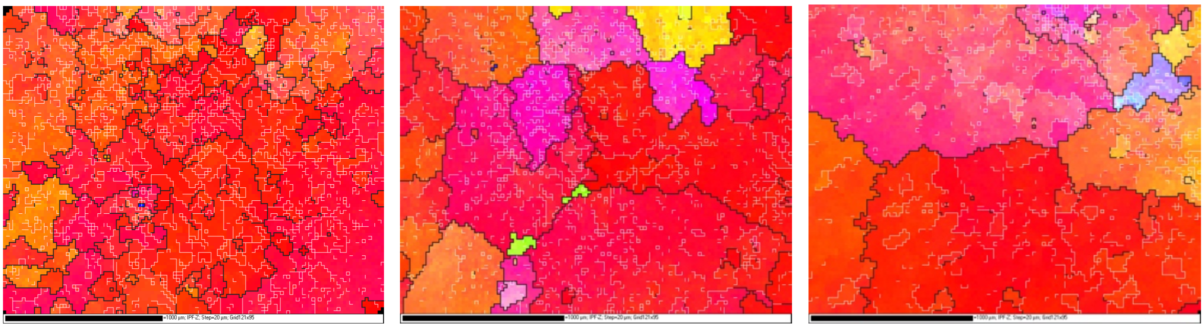

(b) ADC12-Sr

0.02Sr 0.04Sr 0.06Sr

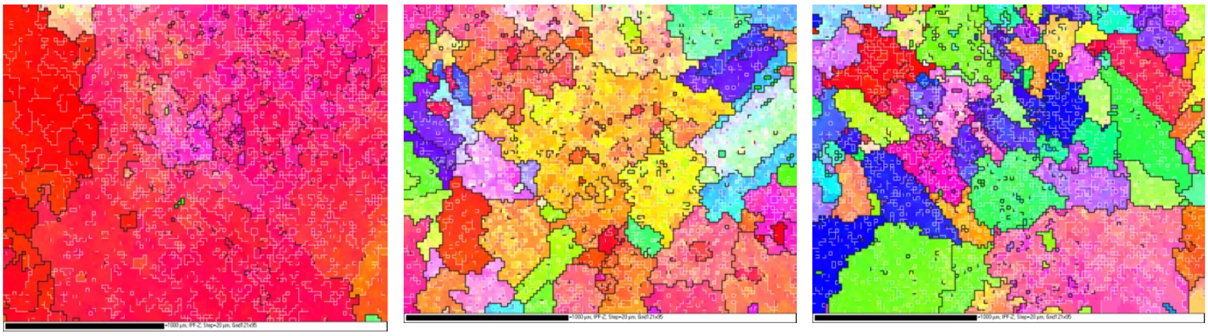

(c) ADC12-Bi

0.5Bi 1.0Bi 1.5Bi

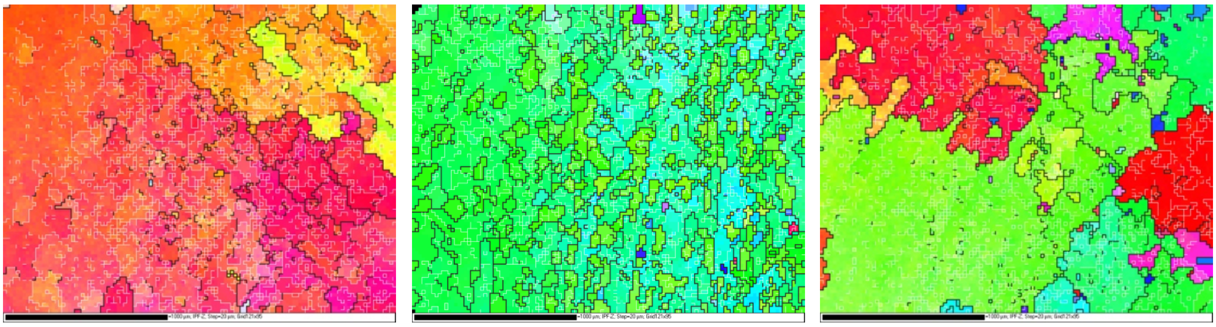

Fig. 5.3 EBSD analysis of the HMC samples: (a) ADC12; (b) ADC12-Sb; (c) ADC12-Sr; (d) ADC12-Bi.

5.2.2 Mechanical properties

Figure 5.4 shows the Vickers hardness (HV) results for GC and HMC samples. Different hardness values were obtained depending on the sample. The hardness value of HMC is generally higher than the hardness value of GC-ADC12 sample. The hardness value of HMC increases as the Sr content increases. Similar hardness results for the Al-Si-Sr alloy were obtained in Ref. [3]. The high hardness of ADC12-Sr may be due to the delicate eutectic Si phase and the randomly organized crystal orientation. Al_2Si_2Sr intermetallic compound particles can also contribute to high hardness and are produced by adding high Sr elements [5]. The creation of the intermetallic particles results in a reduction in the amount of Sr in the melt [5]. Conversely, the hardness of ADC12-Sr decreased with the addition of large amounts of Sr (e.g., 0.06%) . It can be affected by large eutectic Si phases or wide interparticle spacing [6]. Unlike the ADC12-$Sr_{0.06}$ alloy, a similar hardness level was obtained for the other ADC12 with high amounts of Sb and Bi. For the GC samples, their hardness results are widely scattered, and no clear trend is present, although their hardness variations appear to be similar to those for the HMC samples. This condition may be influenced by the fact that in the hardness measurement, a Vickers indentation was loaded on the GC-ADC12 surface of the non-uniformly distributed large size of the hard eutectic Si phase embedded in the α-Al matrix. Figure 5.5 shows the relationship between hardness and microstructural characteristics, where Figure 5.5(a) shows the aspect ratio of the Si phase versus HV, Figure 5.5(b) shows the size of the Si phase versus HV, and Figure 5.5(c) shows SDAS versus HV. As shown in Fig. 5.5(c), no clear correlation exists for SDAS versus HV with R^2=0.03 despite the fact that they should have a linear relationship (i.e., Hall-Petch relation). The reason for this result is unclear at the moment but is assumed to be due to the narrow range of SDAS for HMC (e.g., 6.9-7.8 mm). In fact, the SDAS versus HV relation using the data plots for both GC and HMC samples shows a clear correlation with R^2 = 0.67. By contrast, a relatively linear relationship exists between AS and HV (R^2 = 0.34) and between SZ and HV (R^2 = 0.11). A delicate Si phase and a low aspect ratio result in a high hardness value. Hence, the eutectic Si phases are directly attributed to their mechanical properties.

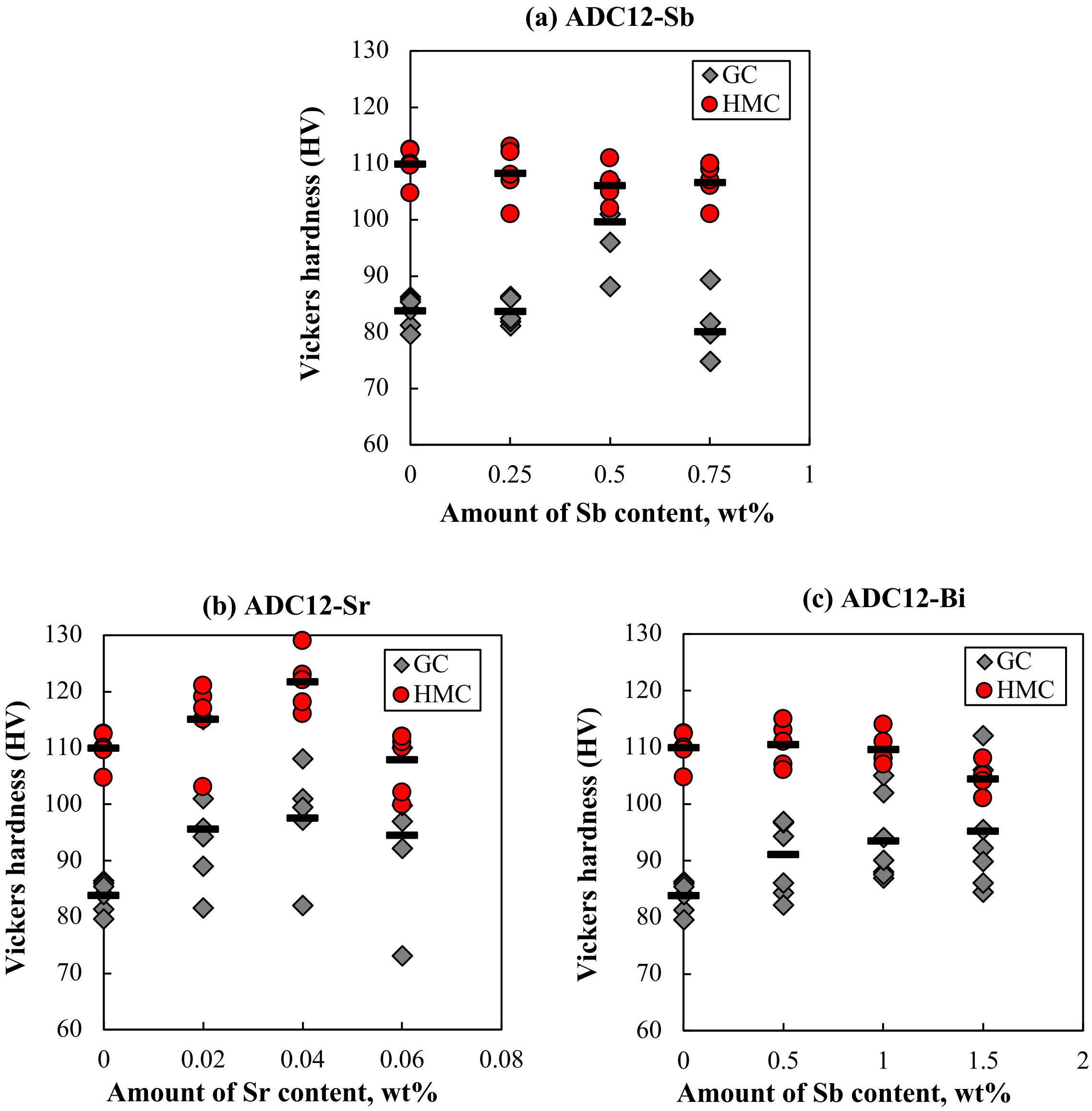

Fig. 5.4 Vickers hardness of the cast aluminum alloys for the HMC and GC samples: (a) ADC12-Sb; (b) ADC12-Sr; (c) ADC12-Bi.

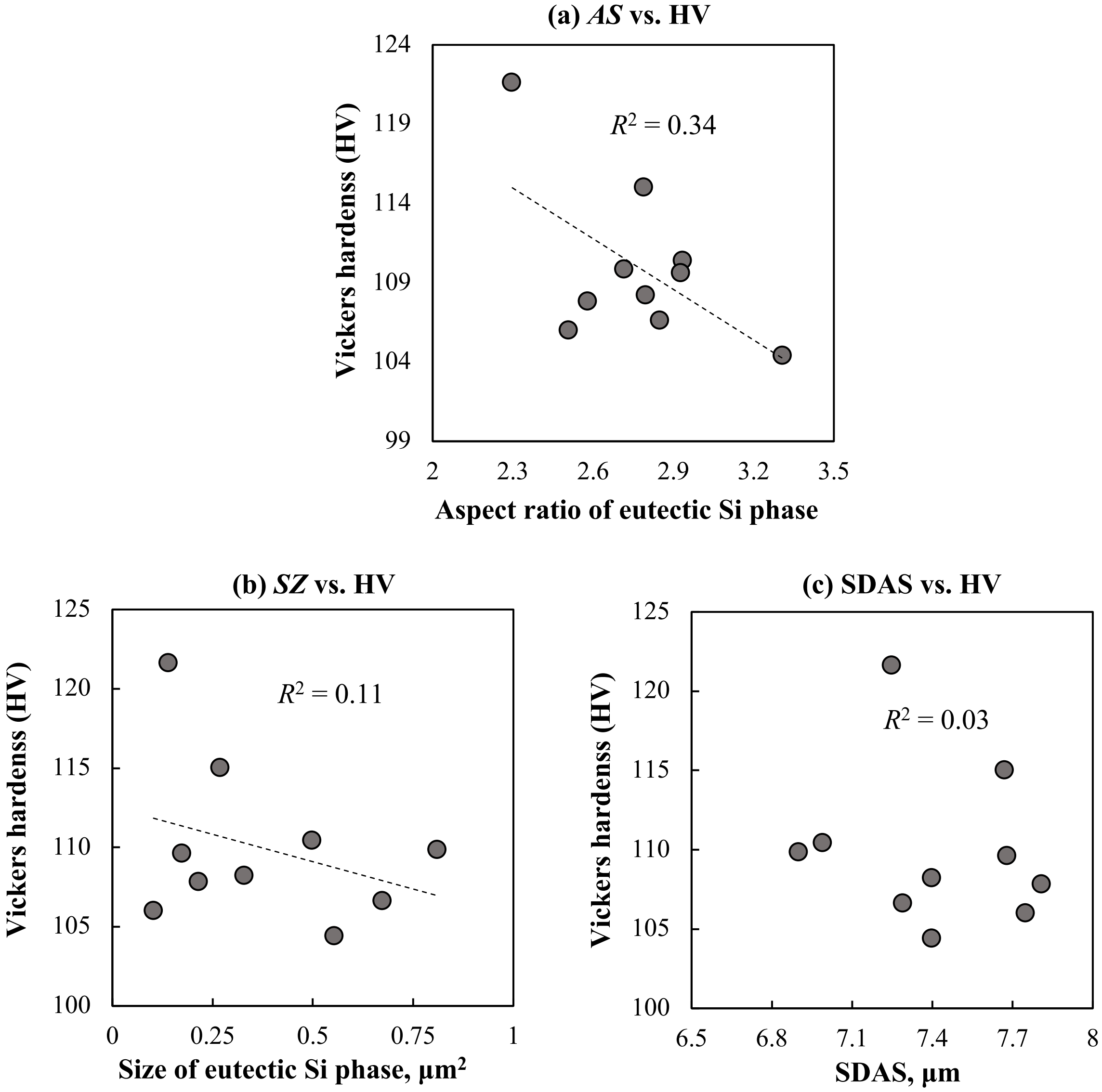

Fig. 5.5 Relationship between hardness and microstructural characteristics: (a) Aspect (*AS*) vs. HV; (b) size (*SZ*) vs. HV; (c) SDAS vs. HV.

Figure 5.6 shows representative tensile stress-strain curves for GC and HMC samples. The tensile stress vs. strain of the HMC-ADC12-Sr sample provides higher values than the GC sample. Due to the similar tensile properties of all GC samples, only the GC-ADC12-Sr alloy was selected for this approach. Based on the stress-strain relations, the ultimate tensile strength (σ_{UTS}) and strain to failure (ε_{f}) are summarized in Fig. 5.6. The tensile strength of the HMC-ADC12-Sr samples increases insignificantly with increasing Sr content, and the highest σ_{UTS} value is obtained when $\mathrm{Sr}_{0.04\text{-}0.06}$ is added. GC-ADC12-Sr produced a delicate eutectic Si phase, but in this case no clear increase in σ_{UTS} was detected. This can be affected by the large size of the α-Al phases (SDAS). In previous studies, the addition of Sr reduced the porosity of the hotspot area of the casting, allowing the pores to be well dispersed and rounded, resulting in high mechanical properties [7]. No apparent defects (porosity) were detected in our HMC-ADC12 alloy. Therefore, the defects did not strongly affect the mechanical properties of the cast sample [7]. Unlike the tensile strength of the HMC-ADC12-Sr alloys, the tensile strength of HMC-ADC12-Sb and -Bi decreases with increasing Sb and Bi content, respectively. Such tensile properties are related to the hardness result. In fact, the tensile strength of HMC samples has a linear correlation with hardness (R^2=0.34) (see Fig. 5.7). The fracture strain of HMC-ADC12-Sb and -Bi increases with the increase of RE element, and high ductility is obtained with HMC-ADC12-1.5Bi (approximately ε_{f} = 14%). Such an increment in the fracture strain was similarly detected with the addition of RE elements in the study of Chen et al. [8], in which the strain level for the Al-2Si-0.1La-0.05B alloy was as high as approximately 17%, although its tensile strength was approximately 130 MPa. From these tensile tests, high mechanical properties were obtained with the HMC-ADC12-Sr alloy, and the addition of Sb and Bi improved the ductility of the HMC-ADC12 alloy material.

(a) ADC12-Sb

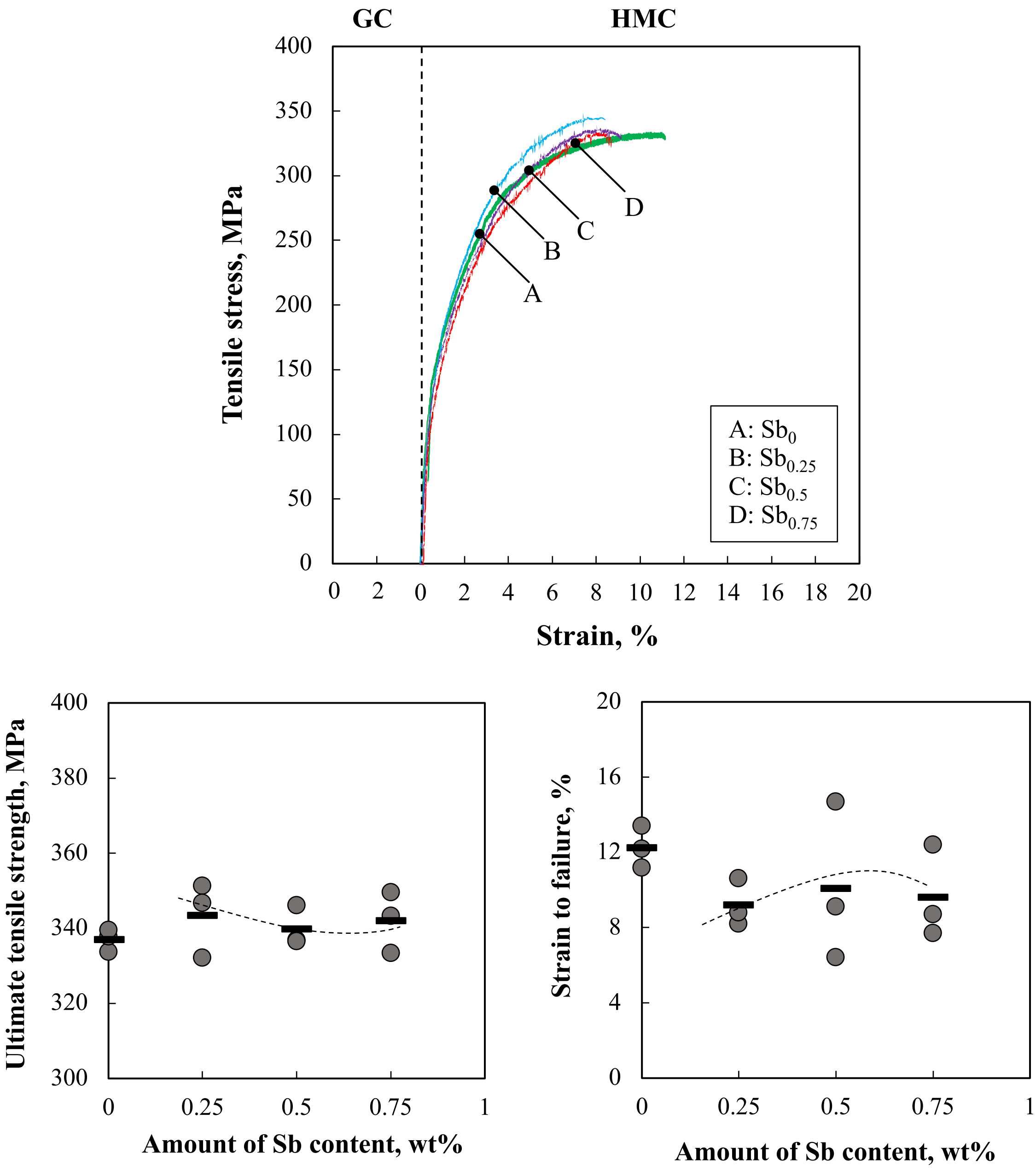

Fig. 5.6 Tensile properties of the cast aluminum alloys for the HMC and GC samples: (a) ADC12-Sb; (b) ADC12-Sr; (c) ADC12-Bi.

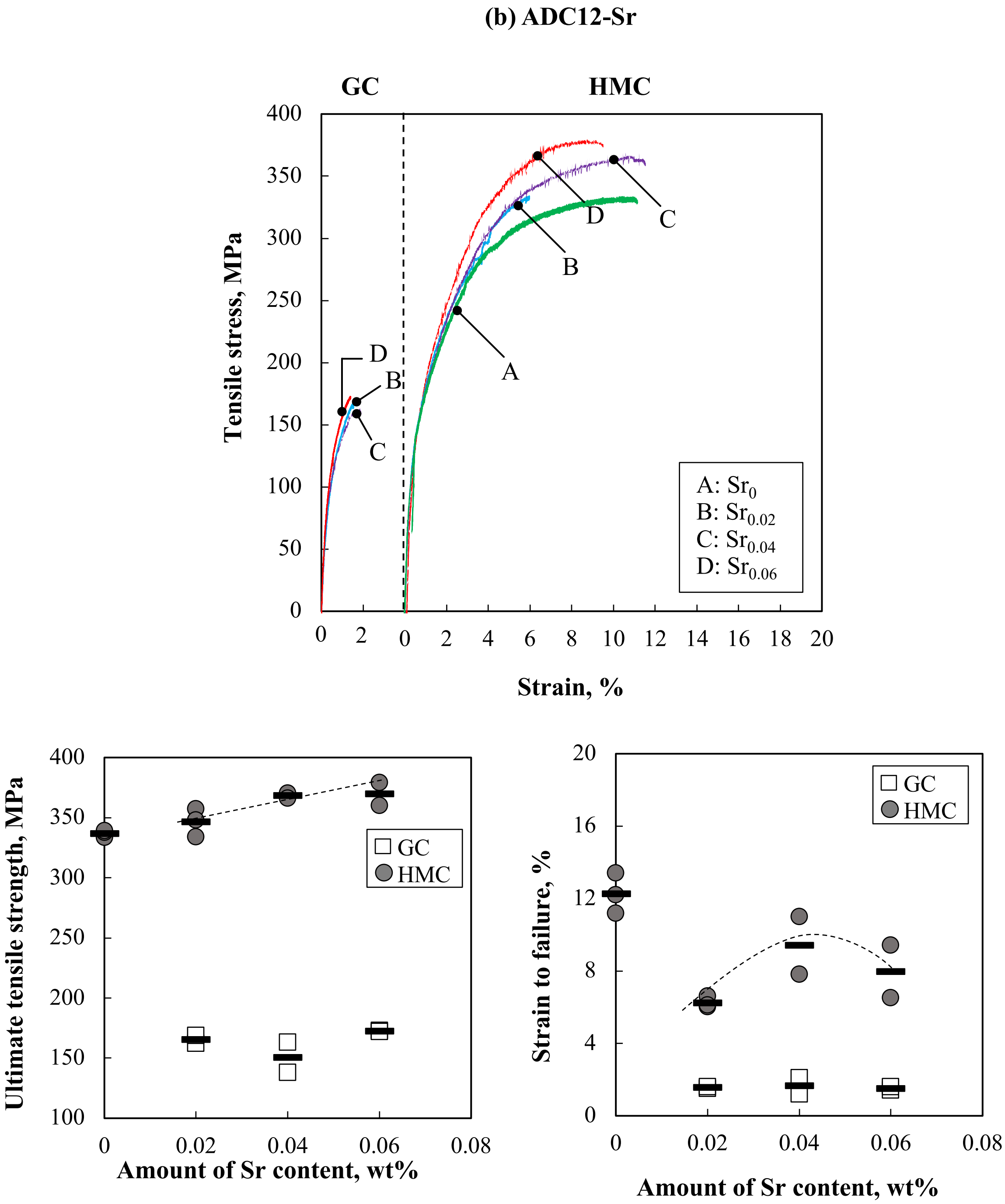
(b) ADC12-Sr

Fig. 5.6 Cont.

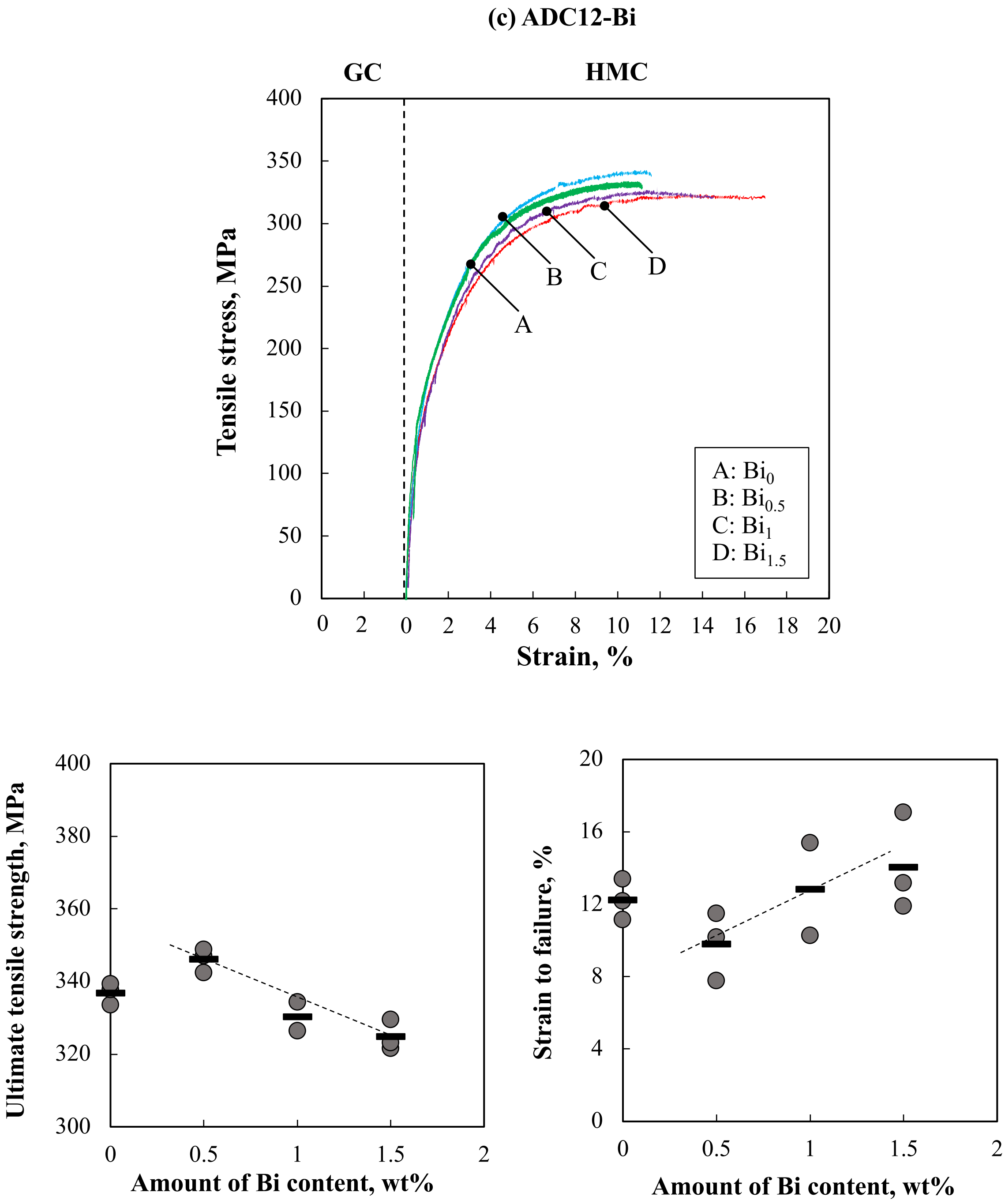
(c) ADC12-Bi
GC
HMC
Tensile stress, MPa
0
50
100
150
200
250
300
350
400
0
2
0
2
4
6
8
10
12
14
16
18
20
Strain, %
A
B
C
D
A: Bi$_0$
B: Bi$_{0.5}$
C: Bi$_1$
D: Bi$_{1.5}$
Ultimate tensile strength, MPa
300
320
340
360
380
400
0
0.5
1
1.5
2
Amount of Bi content, wt%
Strain to failure, %
0
4
8
12
16
20
0
0.5
1
1.5
2
Amount of Bi content, wt%

Fig. 5.6 Cont.

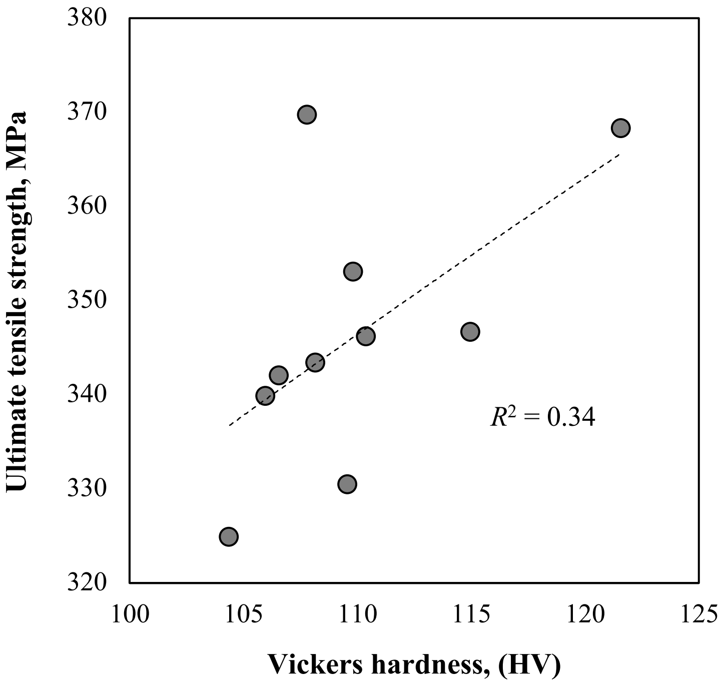

Fig. 5.7 Relationship between ultimate tensile strength and hardness.

5.3 Summary

The material properties of ADC12-RE alloys produced by HMC and GC were investigated experimentally. The results obtained are as follows:

1) With the addition of RE metals (Sb, Sr, and Bi), delicate eutectic structures were obtained in the HMC-ADC12 samples; Sr created tiny eutectic Si particles, and delicate lamellar eutectic Si phases were created in the ADC12-Sb and -Bi alloys. For the GC samples, eutectic Si structures were refined by adding Sr, whereas no apparent effects of Si phase refinement were obtained with the addition of Sb and Bi. A regular oriented lattice structure was observed in the HMC sample containing a small amount of RE element. That is, the crystal orientation of the plane perpendicular to the casting direction was formed by [110]. However, this formation collapsed with the addition of numerous RE elements.
2) The mechanical properties of the HMC-ADC12 sample increased with increasing Sr content, and high hardness was obtained when 0.04% Sr was added. Fine eutectic Si was observed in the GC-ADC12-Sr alloy, but its tensile properties were not significantly improved. In HMC-ADC12, as Sb and Bi added increased, the tensile strength decreased and the fracture strain increased. In particular, the ADC12-1.5Bi alloy showed high ductility (approximately ε_f=14%).

References

1. S.Farahany, A.Ourdjini, M.H. Idrsi, S.G. Shabestari, Evaluation of the effect of Bi, Sb, Sr and cooling condition on eutectic phases in an Al-Si-Cu alloy (ADC12) by in situ thermal analysis, Therm. Acta, 559(2013)59-68.

2. H. Soda, G. Motoyasu, A. Mclean, C.K. Jen, O. Lisbôa, Method for continuous casting of metal wire and tube containing optical fibre, Mater. Sci. Technol., 11(1995)1169-1173.

3. W. Eidhed, Effects of solution treatment time and Sr-modification on microstructure and mechanical property of Al-Si piston alloy, J. Mater. Sci. Technol., 24(2008)29-32.

4. M. Okayasu, K. Ota, S. Takeuchi, H. Ohfuji, T. Shiraishi, Influence of microstructural characteristics on mechanical properties of ADC12 aluminum alloy, Mater. Sci. Eng., 592(2014)189-200.

5. M. Zarif, B. Mckay, P. Schumacher, Study of heterogeneous nucleation of eutectic Si in high-purity Al-Si alloys with Sr addition, Matell. Mater. Trans. A, 42A(2011)1684-1691.

6. S. Khan, A. Ourdjini, Q.S. Hamed, M.A. Alam Najafabadi, R. Elliott, Hardness and mechanical property relationships in directionally solidified aluminum-silicon eutectic alloys with different silicon morphologies, J. Mater. Sci., 28(1993)5957-5962.

7. C.M. Dinnis, M.O. Otte, A.K. Dahle, J.A. Taylor, The influence of strontium on porosity formation in Al-Si alloys, Metall. Mater. Trans. A, 35(2004)3531-3541.

8. Y. Chen, Y. Pan, T. Lu, S. Tao, J. Wu, Effects of combinative addition of lanthanum and boron on grain refinement of Al-Si casting alloys, Mater. Des., 64(2014)423-426.

Chapter 6 New high pressure diecast shot-sleeves for creation of high-quality cast aluminum alloy

6.1 Experimental procedures

6.1.2 Casting materials

Four different casting materials were employed to examine the effect of material properties on the insulation characteristics of the shot sleeve: two aluminum alloys (ADC12: Al-10.6Si-1.1Cu-1.1Fe and ADC6: Al-3.6Mg-0.8Si), tin (99.9Sn), and a bismuth-based alloy (Bi-34.6Pb-18.5Sn-5.4Cd). Their material properties, namely, density, melting point, and surface tension, are summarized in Table 6.1. It should be pointed out that the aluminum alloys (ADC12 and ADC6) are conventional diecasting materials that have been employed for a variety of engineering applications. ADC12 is a representative cast aluminum alloy with high castability and good mechanical properties, while ADC6 alloy has high ductility and high corrosion resistance. In this study, four different materials were selected due to the following reason. The cast metals with different surface tension were chosen based on the extent of surface tension for ADC12 (842 mN·m^{-1}). In this instance, the higher surface tension of ADC6 (1042 mN·m^{-1}) and the lower ones for Sn and Bi-based alloy, see Table 6.1. Because of the similar surface tension level, other diecast aluminum alloys cannot be employed in this approach, e.g., ADC10 and ADC14.

Table 6.1 Material properties of the cast materials.

	Melting point, °C	Density, g·cm^{-3}	Surface tension, mN·m^{-1}
ADC12	580	2.68	842 [6]
ADC6	590	2.65	1042 [7]
Sn	232	7.37	549.3 [8]
Bi-based alloy	70	9.98	432.5 [9]

6.1.2 Casting Machine

To examine the material properties of the cast samples, a compact casting machine was specially made, with a design based on that of a typical cold-chamber diecasting system. Fig. 6.1(a) shows a photograph of the casting machine, consisting of mold, shot-sleeve, and injection system. The molten materials were injected into the mold cavity using a commercial air cylinder at a casting pressure of 1.4 MPa and a casting speed of 115 mm·s^{-1}. It should be pointed out that the casting speed of 115 mm·s^{-1} is much lower than that for the conventional high pressure diecasting process, e.g. 1550 mm·s^{-1} [1]. The reason behind the slow casting speed is to make the cast sample without defects, i.e., air blow and pinhole. The pouring temperatures of the cast metals are as follows: 580 °C (ADC12), 590 °C (ADC6), 232 °C (Sn) and 70 °C (Bi-based alloy). The injection process was performed after the melt was poured into the shot-sleeve, with the shot time lag (STL) set to about 1 s. The mold, made of hardened carbon steel, was designed with a rectangular plate of dimensions 50 × 100 × 5 mm. Figure 6.1 (b) shows a photograph of an Sn casting sample made with this casting machine. A vent (0.5 mm thick, 10 mm wide) was created in the mold to prevent air and gas defects in the cast sample, as shown in Figure 6.1 (a).

6.1.3 Shot-sleeves

The hardened carbon steel shot-sleeve is 30 mm x 150 mm in diameter and was designed in two versions with two different patterns, a flat inner surface, and a grooved inner surface. The grooves were 0.5 mm deep and 1.0 mm wide and intersected at right angles to each other. The groove's purpose was to create an air gap between the melt and the sleeve surface to provide thermal insulation, reduce the contact area between the melt and the sleeve surface, and delay solidification [2]. Figure 6.2 (a) shows a photo and schematic of a shot-sleeve with a flat grooved surface. To facilitate the investigation of the insulation properties of the grooved surface, we created a small rectangular mold with various groove formations. Figure 6.2 (b) shows these molds. Three different molds were prepared: flat and grooved surfaces with widths of 0.5 mm and 1.0 mm. Similar to the shot-sleeves above, the grooves are designed to be 0.5 mm deep and 1.0 mm wide and intersect at right angles to each other. The surface area ratio in contact with the melt was changed by 25, 50, 100% to alter the extent of the thermal insulation. The mold temperature profile was measured directly using a thermocouple mounted on the back of each mold. Three casting samples were created for each metal to verify the quality of the material properties.

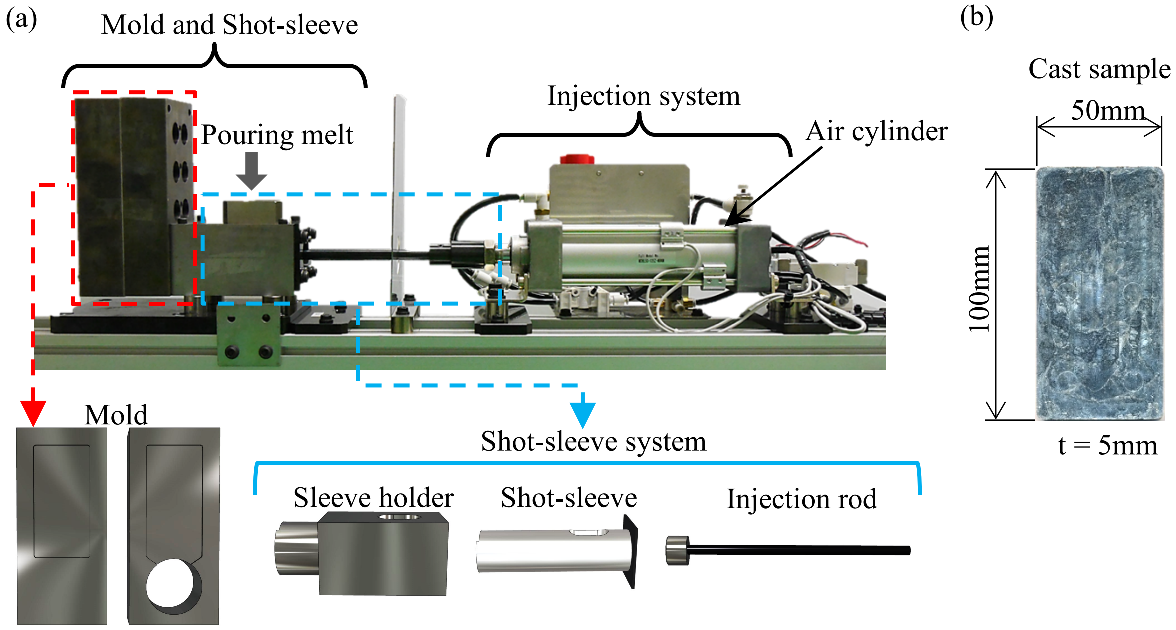

Fig. 6.1(a) Photograph of the casting machine, consisting of mold, shot-sleeve and injection system; (b) photograph of the Sn cast sample.

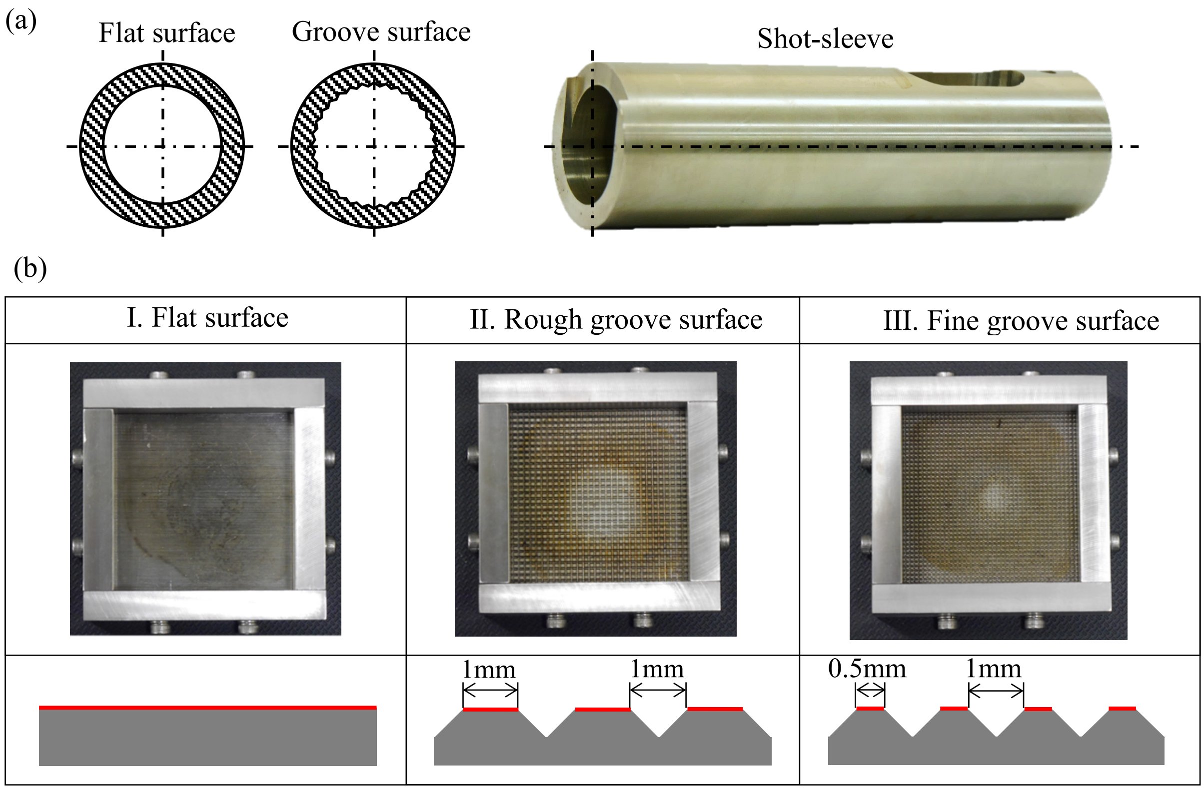

Fig. 6.2 Photograph and schematic diagram of (a) the shot-sleeve and (b) the rectangular molds.

6.1.4 Mechanical properties

The mechanical properties of the cast sample were investigated by hardness and bending tests. Hardness measurements were performed by loading a diamond indenter at 9.8 N for 15 seconds on the surface of the cast sample using a Micro Vickers hardness tester. A three-point bending test was performed at room temperature. A rectangular specimen (50 x 20 x 5 mm) cut from a cast sample was used. The bending load was applied to the center of the specimen at a load rate of 5 mm·min^{-1} to the fracture point using a screw-driven universal tester with a capacitance of 50 kN. The load value was measured with a commercially available load cell.

6.2 Results and discussion

6.2.1 Thermal insulation properties

Figure 6.3 (a) shows the mold temperature profiles after injecting the molten aluminum alloy into the rectangular molds, and Fig. 6.3 (b) shows the maximum mold temperature and the rate of increase of the mold temperature. Note that in each case, the same amount of about 36 cm^3 of molten material was used. The temperature profile of the mold depended on the material and the formation of the mold surface. It is clear that flat molds have resulted in higher mold temperatures than grooved molds. In addition, the finely grooved mold provided a stronger insulating effect on both aluminum alloys. The rate of increase in mold temperature depends on the condition of the mold surface. For example, a higher rate being obtained with the flat mold. It is interesting to note that although a similar trend was observed for both aluminum alloys, the enhancement of the insulation effect with the finely grooved molds was greater for the ADC6 alloy, as indicated with the greater temperature ranges (α and β) in Fig. 6.3(a). This may be due to differences in material properties such as viscosity, surface tension, melting temperature and density. Since the melting temperatures and densities of ADC12 and ADC6 are about the same, the difference in insulation effect can be due to the difference in viscosity and surface tension between the two alloys. Information on the viscosity of aluminum alloys is available, but the data are widely scattered [3-7] . Therefore, in this case, the insulation effect was explained in terms of surface tension energy. This is approximately 842 $mN\cdot m^{-1}$ for ADC12 [8] and 1042 $mN\cdot m^{-1}$ for ADC6 [9]. In this case, the high surface tension of ADC6 suppresses the penetration of melt into the grooves, thereby assisting in the creation of air gaps and reducing the drop in mold temperature.

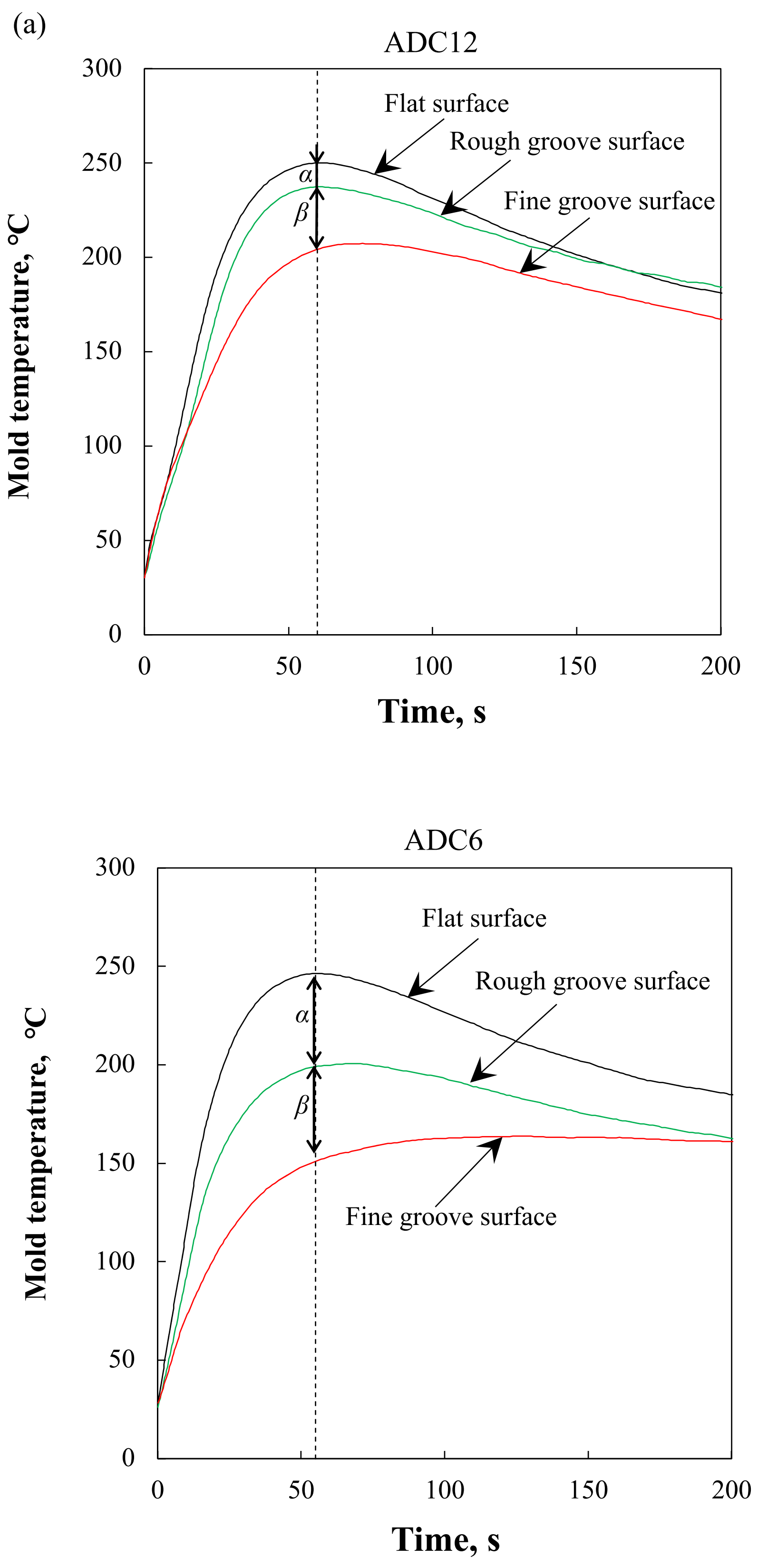

Fig. 6.3(a) Temperature profiles of the mold after pouring molten aluminum alloys in the rectangular molds; (b) the maximum mold temperature and increment rate of the mold temperature.

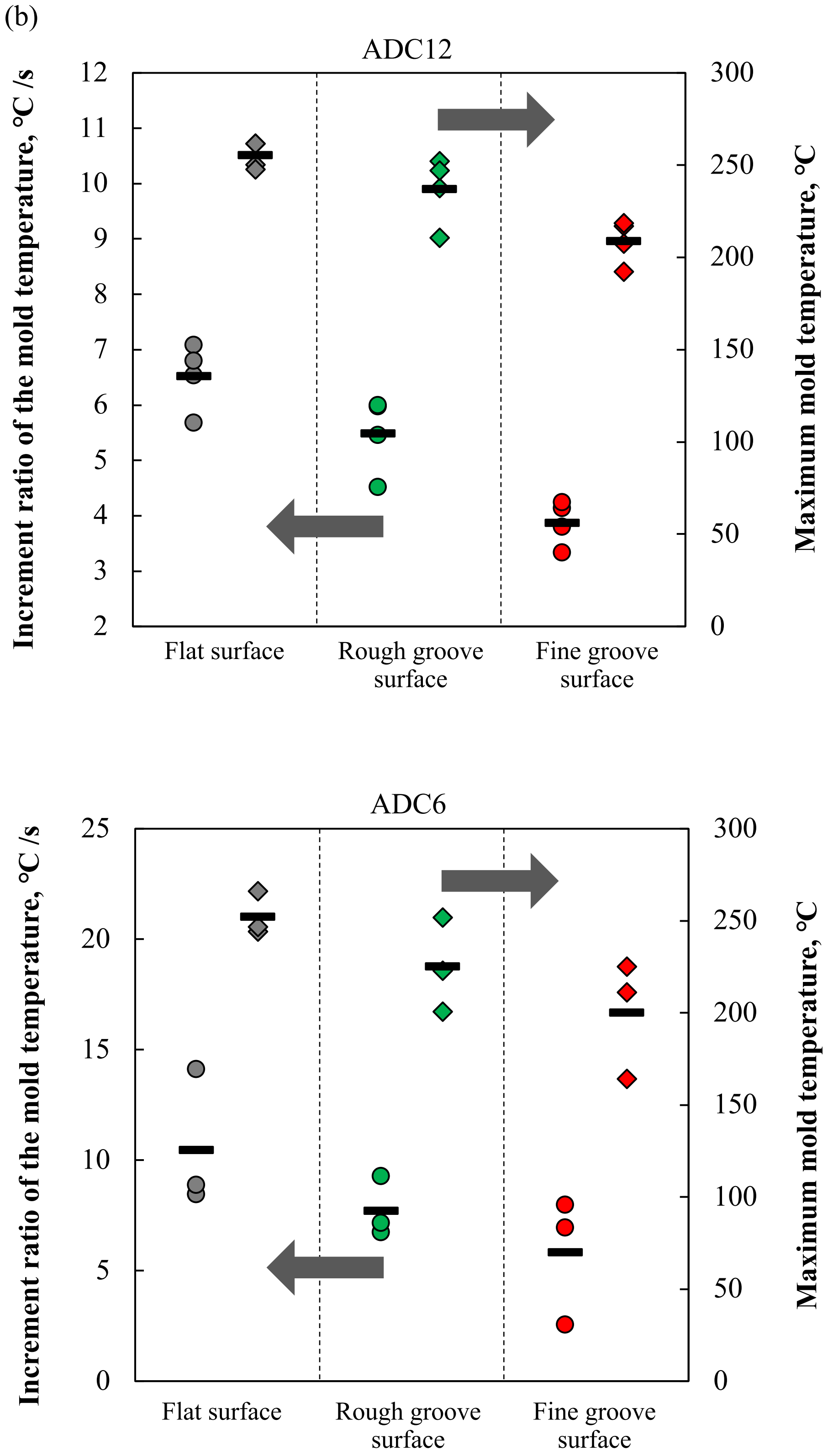
(b)
ADC12
Increment ratio of the mold temperature, °C /s
2
3
4
5
6
7
8
9
10
11
12
Maximum mold temperature, °C
0
50
100
150
200
250
300
Flat surface
Rough groove surface
Fine groove surface
ADC6
Increment ratio of the mold temperature, °C /s
0
5
10
15
20
25
Maximum mold temperature, °C
0
50
100
150
200
250
300
Flat surface
Rough groove surface
Fine groove surface

Fig. 6.3 Cont.

To better understand the insulation properties of shot-sleeves, we experimented with other casting materials with very low surface tension, namely Sn and Bi-based alloys with a surface tension energy of 549.3 mN·m^{-1} [10] and 423.5 mN·m^{-1} [11], respectively. The viscosities of these materials have been reported to be 1.5 mPa·s (at 300 °C) for Sn [12] and 2.0 mPa·s (at 100 °C) for the Bi-based alloy [13]. The results obtained are shown in Figures 6.4 (a) and (b). Due to the low melting point of Bi-based alloys, there was no apparent difference in the temperature profile. However, it seems that a slightly lower mold temperature was obtained with a mold with fine grooves. Interestingly, Sn found the opposite temperature profile. Grooved molds have a higher temperature than flat mold. The difference in temperature profile may be due to the difference in contact area between the melt and the mold surface, with a larger contact area being obtained for the grooved molds because the lower viscosity and lower surface tension facilitated the penetration of the grooves by these melts. To confirm this, cast samples produced in the grooved mold were examined.

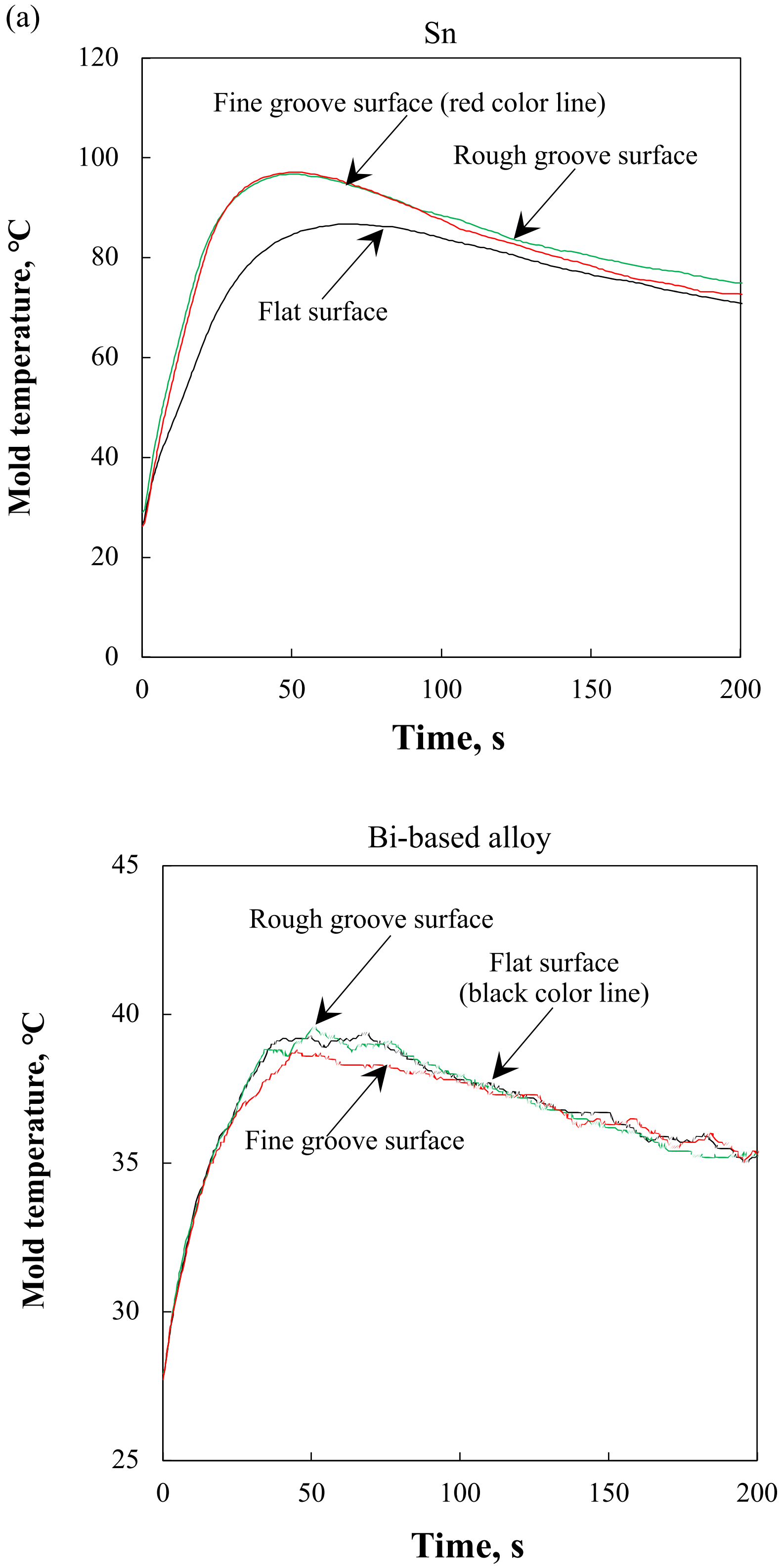

Fig. 6.4(a) Temperature profiles of the mold after pouring molten Sn and Bi-based alloys in the rectangular molds; (b) the maximum mold temperature and increment rate of the mold temperature.

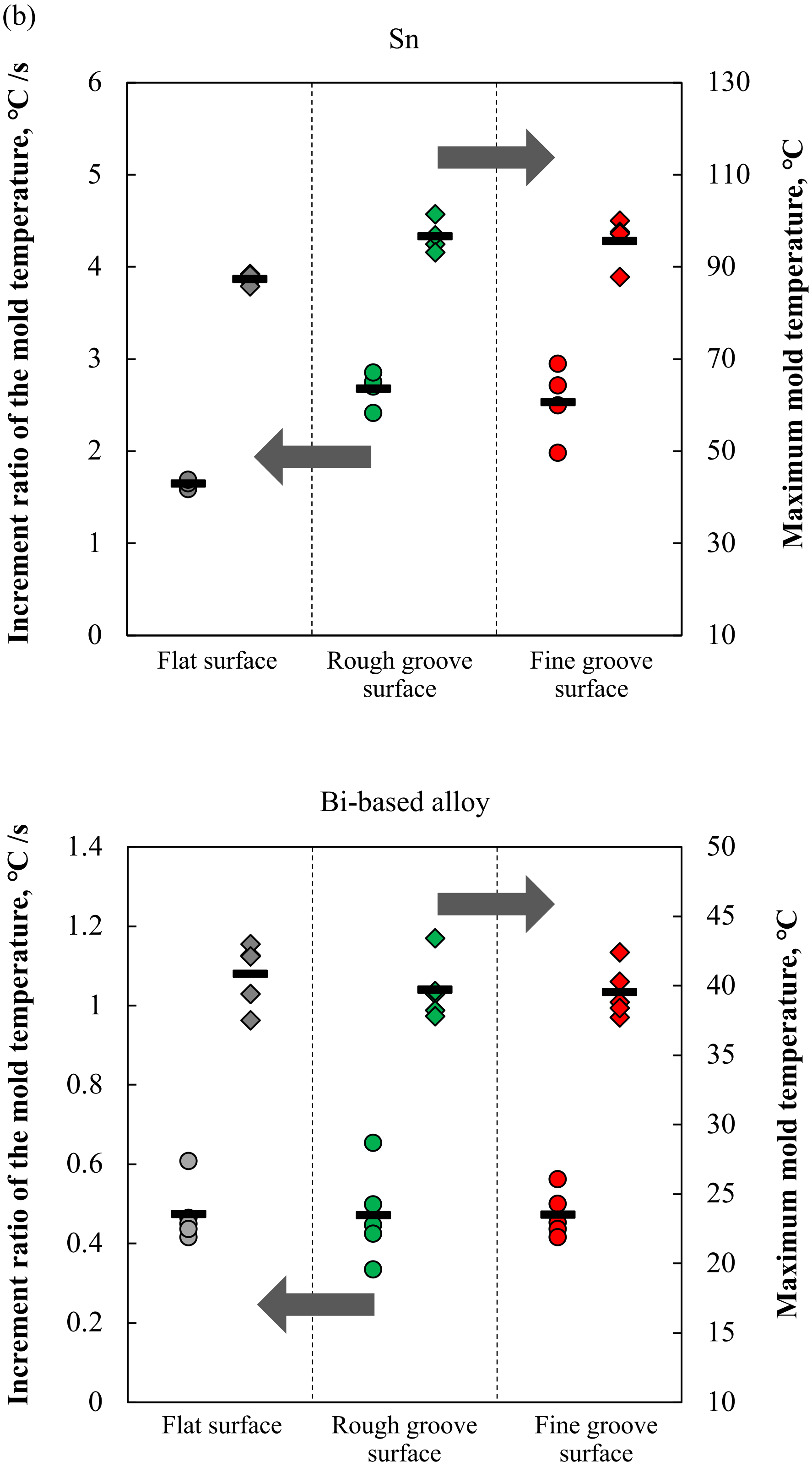
(b)
Sn
Increment ratio of the mold temperature, °C /s
0
1
2
3
4
5
6
Maximum mold temperature, °C
10
30
50
70
90
110
130
Flat surface
Rough groove surface
Fine groove surface
Bi-based alloy
Increment ratio of the mold temperature, °C /s
0
0.2
0.4
0.6
0.8
1
1.2
1.4
Maximum mold temperature, °C
10
15
20
25
30
35
40
45
50
Flat surface
Rough groove surface
Fine groove surface

Fig. 6.4 Cont.

Figure 6.5 shows a cross-section of the casting materials solidified with a rectangular grooved mold. As can be seen, the penetration into the groove varied. For example, both aluminum alloys have low penetrance (although ADC12 has slightly higher penetrance). In contrast, there was strong penetration by Sn and Bi-based alloys, with a greater penetration by the former. As before, these variations in the degree of penetration can be due to the different material properties of the melt.

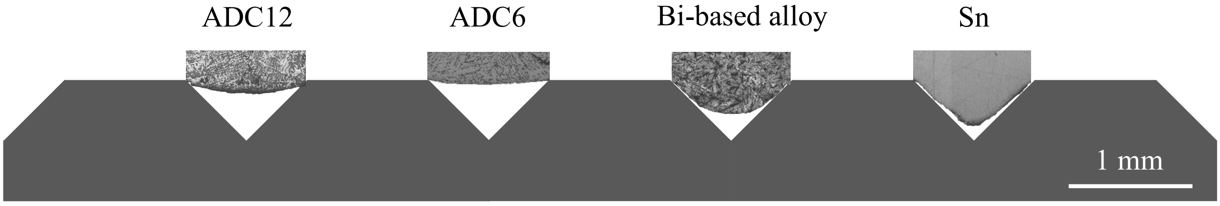

Fig. 6.5 Photograph of the cross-section of the cast samples, solidified in the rectangular groove mold, showing the different severity of the penetration in the groove.

6.2.2 Mechanical properties

To understand the relationship between mold insulation and the presence of casting defects (especially cold flakes), we investigated the material properties of casting samples made with the casting machine shown in Figure 6.1 (a). Due to technical issues with cast samples of the high-melting-point aluminum alloys (ADC12 and ADC6), the first approach used two other materials (Sn and Bi-based alloys). Figure 6.6 shows the results of the bending properties of both materials. (a, b) bending stress versus deflection, and (c, d) bending strength. As shown in Fig. 6.6 (b), the stress versus deflection curve of the Bi-based alloy created using the grooved shot-sleeve surface (Bi-G) is located at a higher level compared with the curve for the flat surface (Bi-F), although the data are relatively scattered. This might be attributed to differences in sample quality. This may be due to differences in sample quality. Interestingly, the elastic region's stress vs. deflection curve is similar in both samples, but the curve clearly varies from yield point to final failure. This may be due to a defect contained in the cast sample.

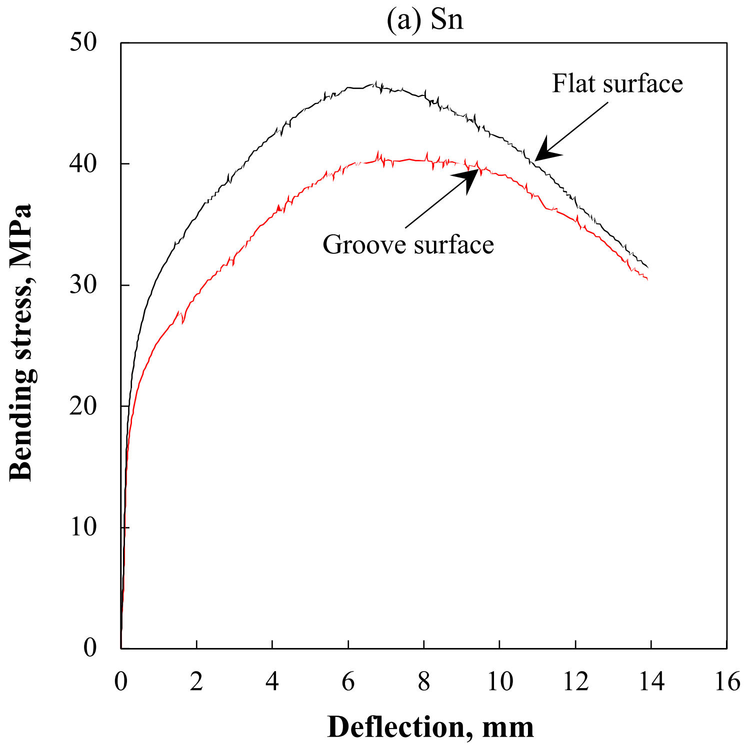

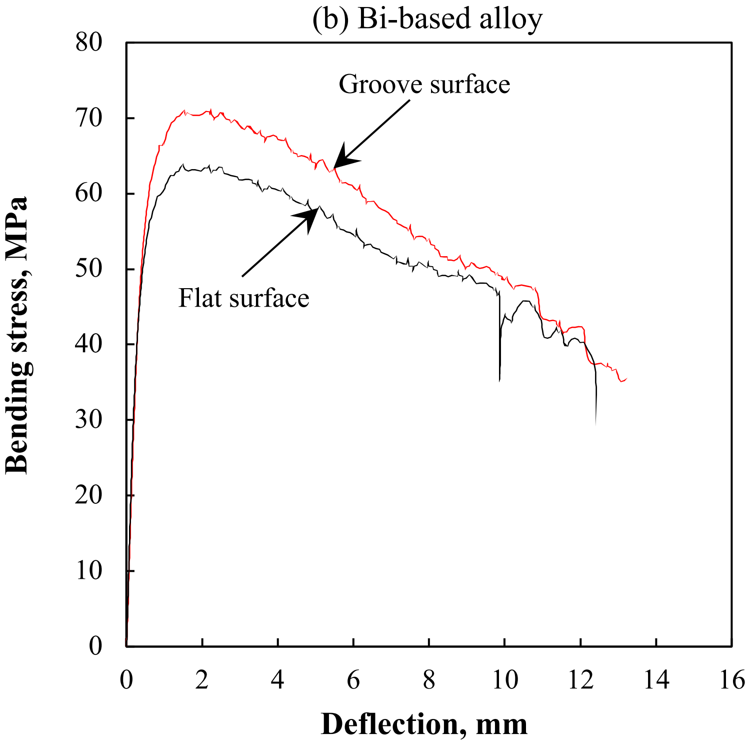

Fig. 6.6 Bending properties of Sn and Bi-based alloy: (a)(b) bending stress vs. deflection curve and (c)(d) bending strength.

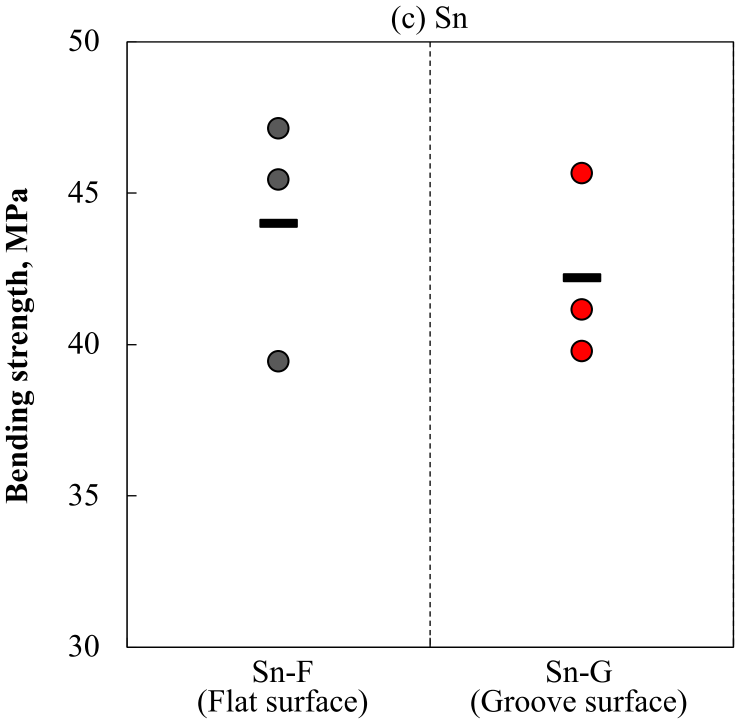
(c) Sn
Bending strength, MPa
50
45
40
35
30
Sn-F
(Flat surface)
Sn-G
(Groove surface)

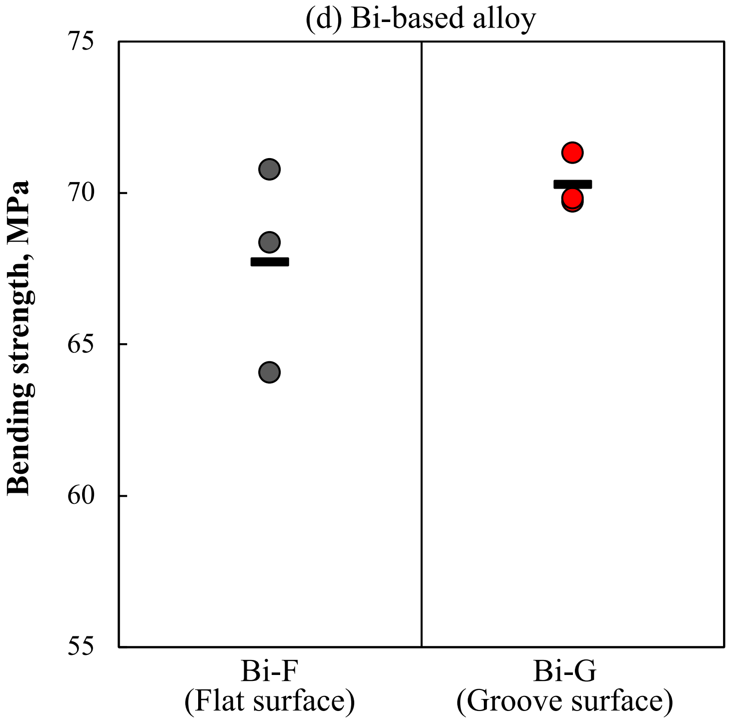
(d) Bi-based alloy
Bending strength, MPa
75
70
65
60
55
Bi-F
(Flat surface)
Bi-G
(Groove surface)

Fig. 6.6 Cont.

Following the bending test, the fracture characteristics of the test piece were investigated. Figure 6.7 shows a photograph of the Bi-F and Bi-G alloys after the bending test. Due to the formation of cold flakes, it is clear that Bi-F has some flaws. Bi-G samples, on the other hand, have no apparent defects. This may be due to the insulation effect of the shot-sleeve. Different bending characteristics can be seen in Sn samples. As shown in Figure 6.6 (a), the stress versus deflection curve of the Sn-F sample is higher than that of the Sn-G sample, in contrast to the curve of the Bi alloy. To substantiate this, the hardness of the Sn sample was measured.

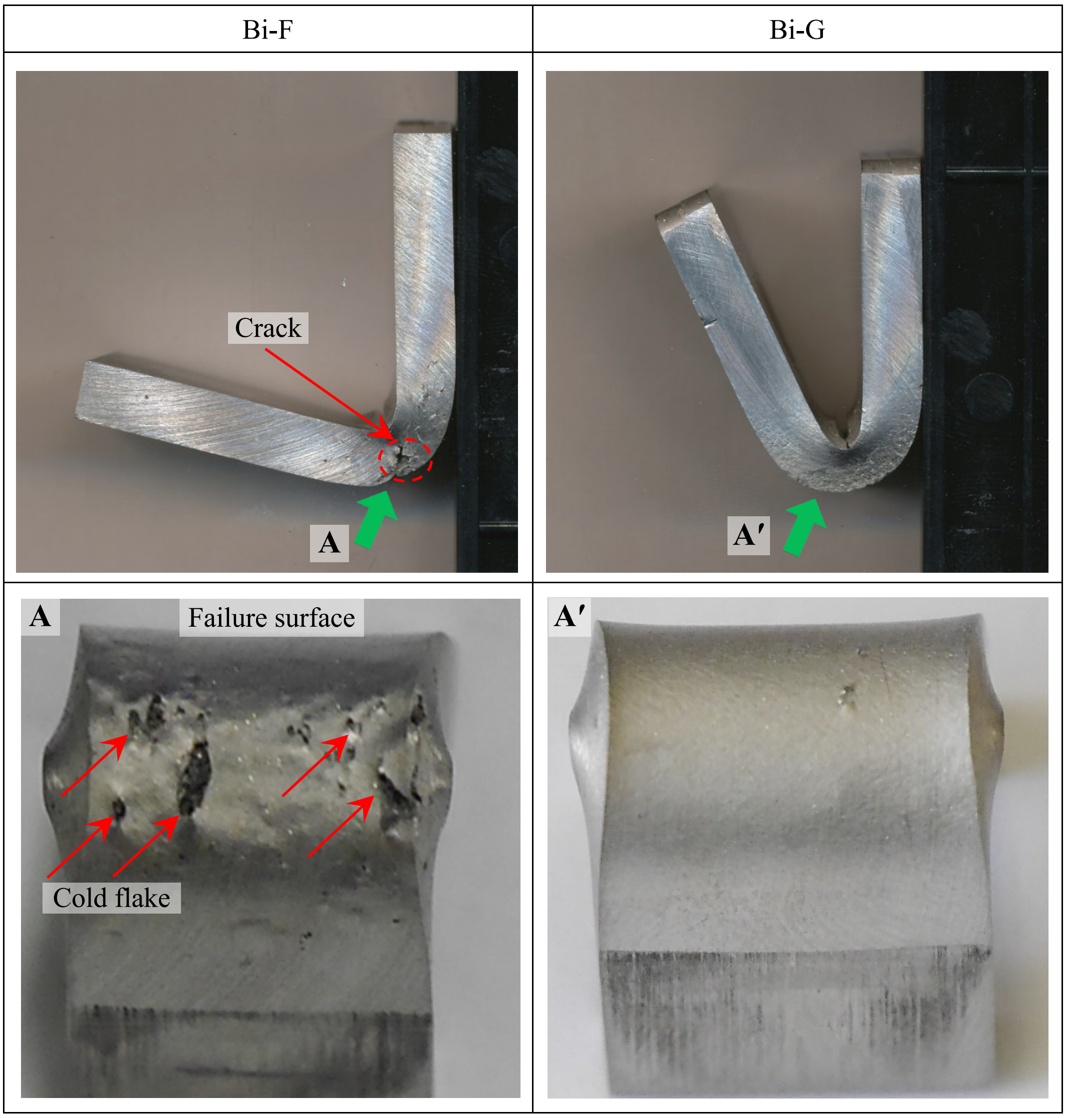

Fig. 6.7 Photograph of the Bi-F and Bi-G alloys after the bending test.

Figure 6.8 shows the Vickers hardness of Sn-G and Sn-F samples. The hardness of the Sn-F sample was about 10% higher than that of the Sn-G sample. The reason is unclear at this time, but it may be due to differences in sample quality. It should be pointed out that the fracture surface observations did not show clear cold flakes in either Sn sample. As shown in Fig. 6.4 (a), the temperature profile of the Sn-G mold is higher than the Sn-F temperature profile, so the injection conditions during the casting process may differ between Sn-F and Sn-G. To clarify this, we investigated the effect of casting pressure fluctuations during the injection process. The strain of the injection rod measured the pressure level; see Fig. 6.1 (a).

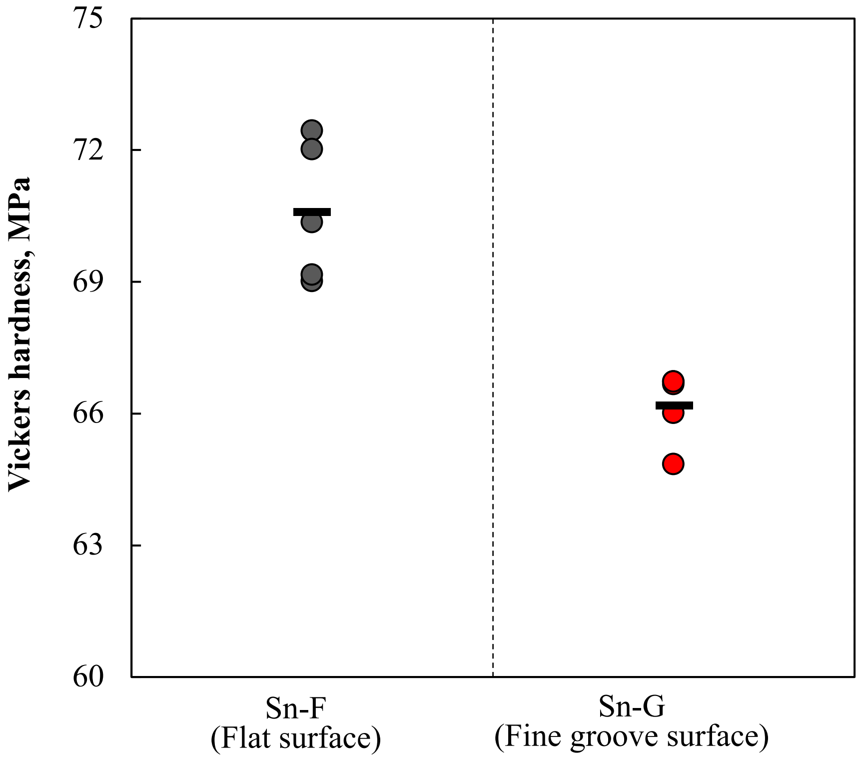

Fig. 6.8 Vickers hardness of the Sn-G and Sn-F samples.

Figure 6.9 shows the change in strain during casting of Sn-G and Sn-F samples. In contrast to the relatively smooth movement of flat shot-sleeves, grooved shot-sleeves show irregular strain behavior. These results show that the injection pressure changes during the casting process, especially for grooved sleeves, resulting in higher injection resistance or lower casting pressure for Sn-G samples. This might be assumed to reduce the sample density. This is likely to reduce the sample density. The densities of Sn-G and Sn-F samples were measured by the Archimedes method and the results are shown in Figure 6.10. As you can see, the density of Sn-G is lower than that of Sn-F. Note that the standard regular density of Sn is 7.365 g·cm^{-3} [14]. In this case, low-density Sn-G samples will result in poor mechanical properties, as shown in Fig. 6.6 and 6.7.

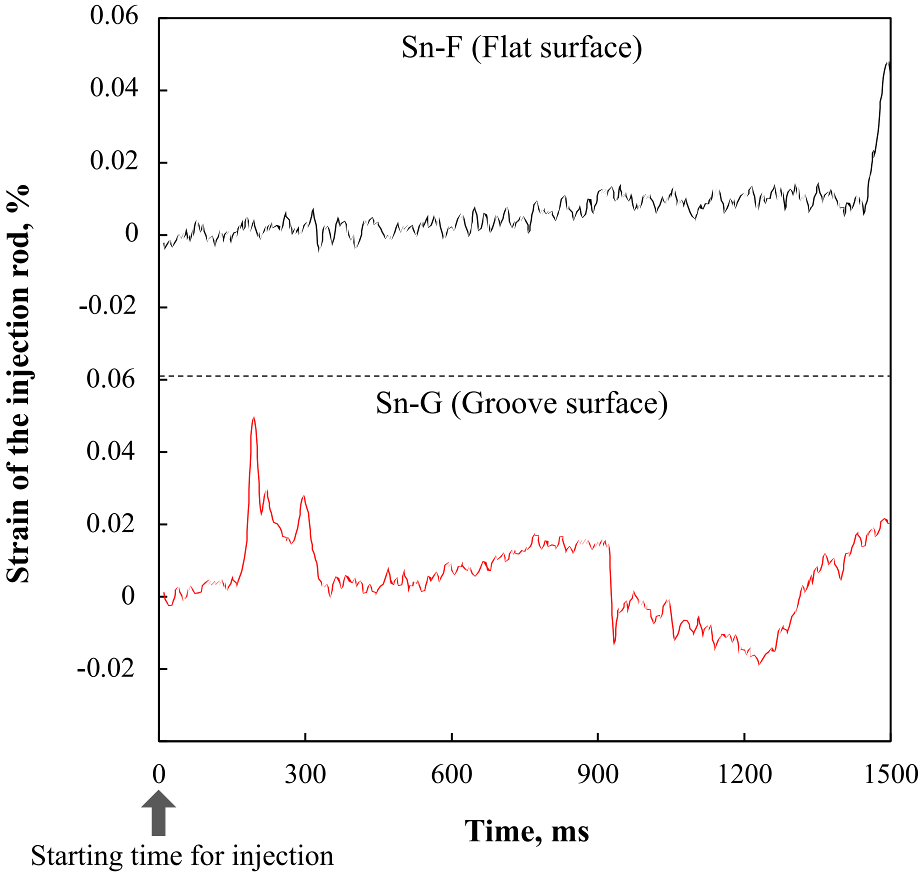

Fig. 6.9 Variation of the strain of the injection rod during the casting process with the flat and groove shot-sleeve.

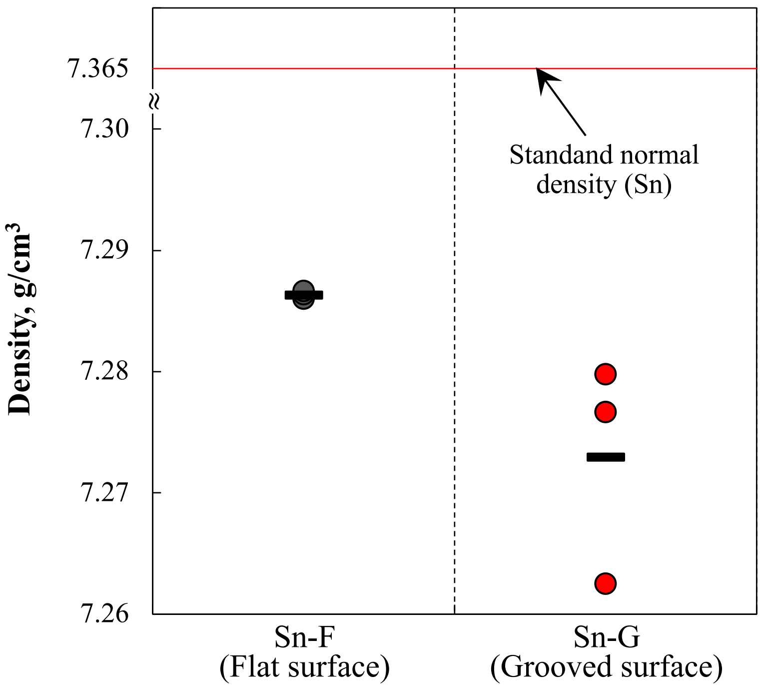

Fig. 6.10 Density of Sn-G and Sn-F samples, determined by Archimedes' method.

The reason for the high injection resistance of the Sn-G sample is as follows: the thick solid layer of Sn in the grooved shot-sleeve interrupts the injection process, as shown schematically in Fig. 6.11. To understand this, a finite element analysis (FEA) was carried out to estimate the thickness of the solid layer. The model for the analysis was constructed based upon our experimental conditions (see, e.g., Figs. 6.2(a) and 6.5), and the analysis used the following parameters: melt temperature (Sn) 300 °C, sleeve temperature 160 °C, thermal conductivity between sleeve and liquid Sn 60 W $mm^{-2} \cdot °C^{-1}$. The results of the analysis are shown in Fig. 6.12(a) and (b), for shot time lags (STL) of 5 s. Note that the STL of 5 s is longer than that for the actual test condition, 1 s, at which no solid layer is seen in this FE analysis. Although solid layer is not obtained numerically at STL of 1 s, this result may imply a high resistance to the injection process in the injection process of the Sn sample.

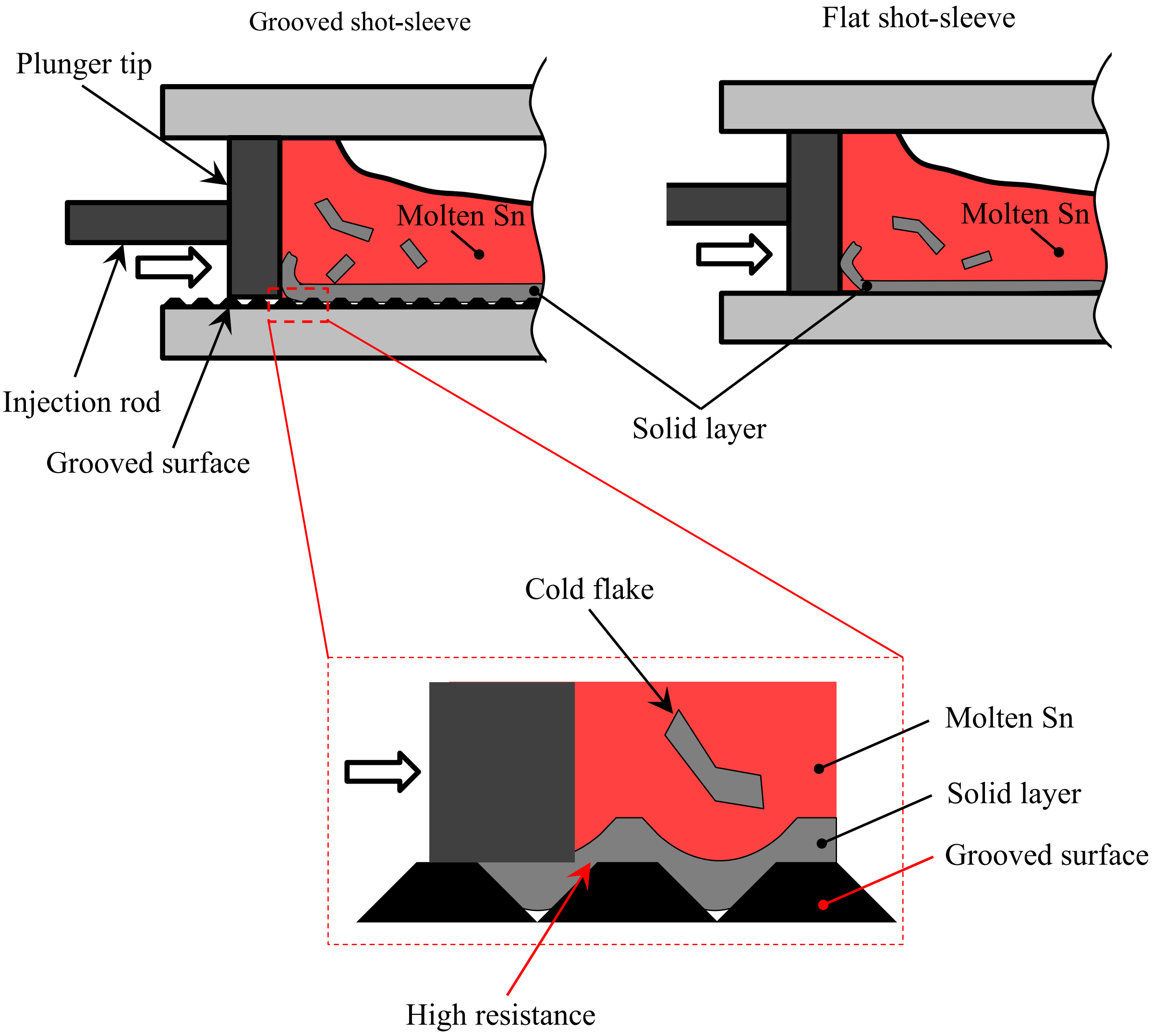

Fig. 6.11 Schematic illustration of the injection process in the grooved and flat shot-sleeves, showing the Sn solid layer.

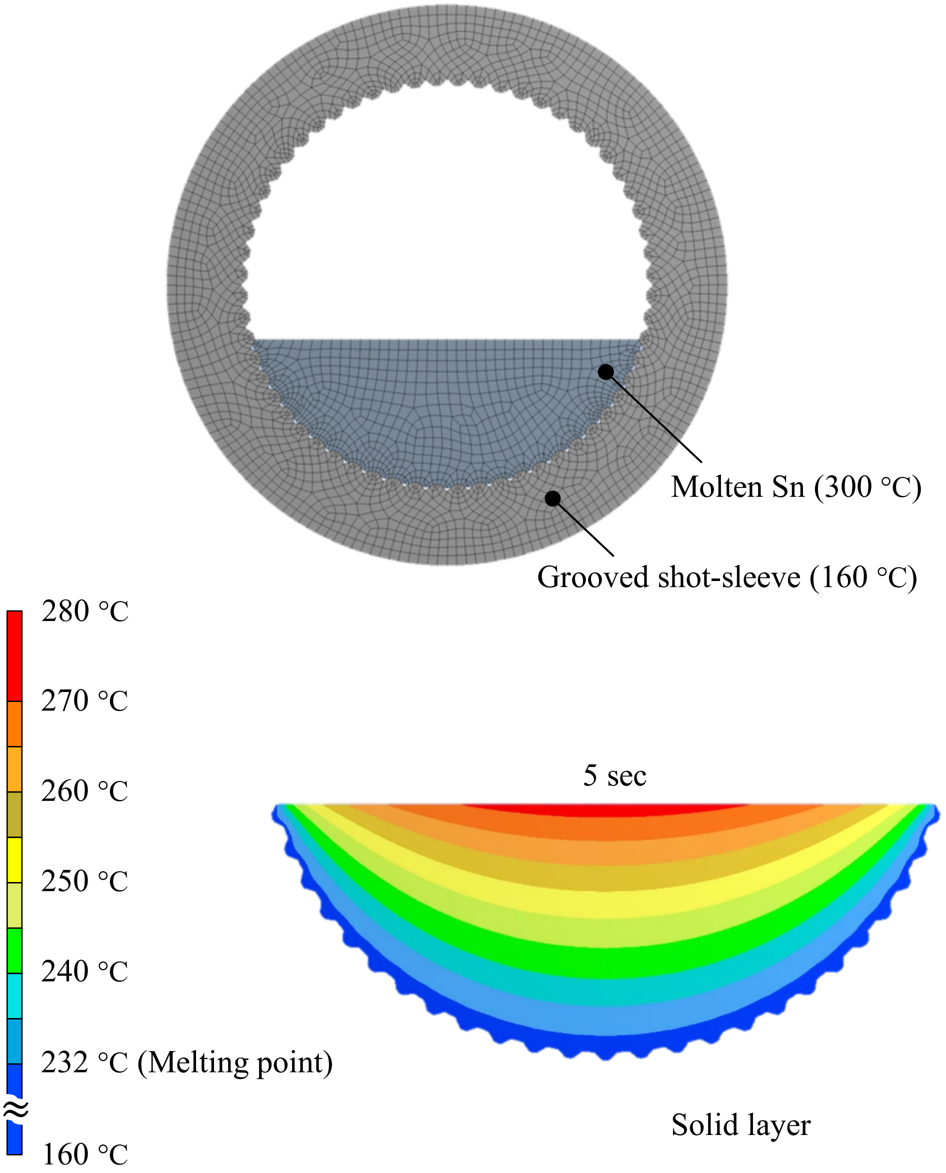

Fig. 6.12 Solid layer of Sn in the grooved shot-sleeve at the shot time lags of 5 s calculated by FE analysis.

6.3 Summary

In this work, a new shot-sleeve was proposed to prevent the creation of cold flakes. To investigate the insulation properties of the shot-sleeve, experimental and numerical investigations were carried out using four different materials: an Al-Si-Cu alloy, an Al-Mg alloy, Sn, and a Bi-Pb-Sn-Cd alloy. The results obtained lead to the following conclusions:

1) The maximum mold temperature and rate of increase of mold temperature are altered depending on the surface condition, for example, a lower rate being obtained with the grooved mold. The enhancement of the insulation effect with the finely grooved molds is greater for the ADC6 alloy due to high surface tension.
2) The amount of cold flakes in the cast sample is reduced by using a grooved shot-sleeve. This is more effective when casting materials with high surface tension because it creates an air gap between the melt and the sleeve surface (inside the groove) and reduces thermal conductivity. Casting samples containing cold flakes showed low bending strength and high stress concentration caused fracture due to defects.
3) The stress versus deflection curve for the cast materials made using the grooved shot-sleeve surface is located at a higher level compared with the curve for the flat surface ones. The stress vs. deflection curve in elastic region is similarly seen in both samples although the yield stress and ultimate bending strength are apparently altered. The change of the stress-deflection curves is caused by the cold flakes created on the inner surface of the shot-sleeve.
4) The cast materials with low surface tension and low viscosity make a thick solid layer in the groove zone, leading to low castability. This results in a low density of the cast sample and consequently to poor mechanical properties, such as hardness and bending strength.

References

1. A. Hamasaiid, G. Dour, M. Dargusch, G. Savage, Heat transfer coefficient and in-cavity pressure at the casting-die interface during high pressure die casting of magnesium alloy AZ91D, Metal. Mater. Trans. A, 39(2008)853-864.

2. T. Loulou, E.A. Artyukhin, J.P. Bardon, Estimation of thermal contract resistance during the first stages of metal solidification process: II-experimental setup and results, Int. J. Heat. Mass. Trans., 42(1999)2129-2142.

3. S. Vinith, A. Uthayakumar, S.S. Rajan, Fluidity of ADC12 alloy based on theoretical and computational fluid dynamics, Int. J. Sci. Research, 4(2015)996-999.

4. C.J. Vreeman, F.P. Incropera, The effect of free-floating dendrites and convection on macro segregation in direct chill cast aluminum alloys: part II: predictions for Al-Cu and Al-Mg alloys, Int. J. Heat & Mass Trans., 43(2000)687-704.

5. Y. Wang, Y. Wu, X. Bian. Composition dependence of viscosity for $Al_{(1-x)}Mg_x(0\leq x\leq 0.10)$ alloys, Chinese Sci. Bulletin, 52(2007)1441-1445.

6. M. D. Sabatino, L. Arnberg, A review on the fluidity of Al based alloys, Matell. Sci. Technol., 22(2013)9-15.

7. B. Zhu, L. Li, X. Liu, et al., Effect of viscosity measurement method to simulate high pressure die casting of thin wall AlSi10MnMg alloy castings, J. Mater. Eng. Perform., 24(2015)5032-5036.

8. H. Kobatake, J. Brillo, J. Schmitz, et al., Surface tension of binary Al-Si liquid alloys, J. Mater. Sci., 50(2015)3351-3360.

9. C.G. Cordovilla, E. Louis, A. Pamies, The surface tension of liquid pure aluminum and aluminum-magnesium alloy, J. Mater. Sci., 21(1986)2787-2792.

10. J. Lee, W. Shimoda, T. Tanaka, Surface tension and its temperature coefficient of liquid Sn-X (X=Ag, Cu) alloys, Mater. Trans., 45(2004)2864-2870.

11. Y. Plevachuk, V. Sklyarchuk, G. Gerbeth, et al., Surface tension and density of liquid Bi-Pb, Bi-Sn and Bi-Pb-Sn eutectic alloys, Surface Sci., 605(2011)1034-1042.

12. H.R. Thresh, A.F. Crawley, The viscosities of lead, tin and Pb-Sn alloys, Metal. Trans., 1(1970)1531-1535.

13. C.J. Morris, Microscale self-assembled electrical contacts, Adelphi, MD: Army Research Laboratory, (2007).

14. X.Wang, M. Feygenson, M.C. Aronson, et al., Sn/SnO_x core–shell nanospheres: Synthesis, anode performance in Li ion batteries, and superconductivity, J. Phys. Chem. C., 114(2010)14697-14703.

Chapter 7 Conclusions

In this thesis, the mechanical properties of cast Al-Si-Cu aluminum alloy created by microstructural control (solidification, precipitation, and the addition of alloy elements) were systematically investigated. Major conclusion and achievements in this work are as follows:

(i) To understand the solidification characteristics of cast Al-Si-Cu alloys, unidirectional casting samples were created under controlling the cooling. In this approach, influence of the size of α-Al and eutectic Si on the mechanical properties was examined. The microstructural properties of the cast sample depended on the cooling rate, e.g., fine and coarse microstructures obtained with cooling rates of 0.02 $°C \cdot s^{-1}$ and 0.14 $°C \cdot s^{-1}$, respectively. The crystal structure was changed by the sample area and resulted in the amount of Si present during solidification. In the lower and middle regions, the α-Al phase formed relatively organized crystal structures of different patterns, e.g., $\langle 101 \rangle$, columnar grain growth of α-Al dendrites with a low eutectic Si content was observed. Although columnar grain growth was also found in the upper region, it was randomly formed, and the area was narrower. Random crystal orientation (i.e., weak control of unidirectional solidification) was created by interrupting columnar α-Al dendrite growth, which resulted from changes in the dynamics of the alloyed Si atoms. Eutectic Si is considered the only Si precipitate in ADC12; however, primary Si was also formed in the middle and upper regions, which was attributed to high Si concentrations resulting from Si migration to the upper region. Fine and coarse microstructures were observed in the lower and upper regions, respectively, with the middle region acting as a transition zone in which the amount of Si rapidly increased following transport between the lower and upper regions. A high amount of hard Si precipitate in the upper region of the sample resulted in high hardness values. In contrast, due to its fine microstructure with unidirectional crystal formation, the lower region exhibited high tensile strength and high ductility.

(ii) To examine the precipitation hardening of Al-Si-Cu alloy, artificial agings were performed under various conditions after water quenching. Two cast samples were employed: gravity casting (GC) and heated mold continuous casting (HMC). The Vickers hardness of the GC sample was higher than that of the HMC sample under all heat treatment conditions. It may be due to the high solubility of the alloying elements in the α-Al matrix and the presence of complex dislocation walls in the GC sample. The hardness of GC and HMC samples aged at 160, 175, and 190 °C increased similarly with increasing aging time, and an aging peak occurred in the age-hardening curve between 10 and 15 h. In contrast to the hardness results, the ultimate tensile strength (UTS) of the as-cast GC sample is about 30% lower than that of the as-cast HMC sample due to the large brittle eutectic Si and Fe structures. The highest UTS: approximately 390 MPa, was obtained with HMC samples aged at 175 °C for 13 h. It was about 20% and 10% higher than the as-cast HMC sample and the GC sample aged at 175 °C for 13 h, respectively. The high UTS of the HMC sample was due to the precipitation of the $\theta'(Al_2Cu)$ metastable phase and the formation of small microstructures.

(iii) To make grain refinement of cast Al-Si-Cu alloy, several RE elements were added. The addition of 0.04Sr produces a fine spherical eutectic Si phase, but the addition of Sb and Bi produces a fine layered eutectic Si phase. It may be because the crystal orientation of the plane perpendicular to the casting direction is formed by [110]. However, in the ADC12 alloy, this uniform formation collapses as Sr added increases, such as Sr > 0.04%. To better understand the effects of the eutectic Si characteristics on the mechanical properties, the shape and size of eutectic Si were statically analyzed. As a result, the mechanical properties of the ADC12-Sr alloy increase with increasing Sr content due to the formation of fine eutectic Si and randomly oriented crystals. On the other hand, the ductility increases with the increasing addition of Sb and Bi elements, and the highest fracture strain of approximately 14% is obtained for the ADC12-1.5Bi alloy.

(iv) To improve the mechanical properties of cast Al-Si-Cu alloy, an attempt was made to reduce cast defects especially cold flakes created in shot-sleeve. Cold flakes are generated by the solidification of the casting material in the shot sleeve before the injection process. To solve this problem, a new shot-sleeve with a thermal insulation system has been introduced on the inner shot-sleeve surface and tiny grooves have been machined to create an air gap between the melt and the sleeve surface. Various casting materials with different material properties are used to examine the insulating effect of the shot-sleeve. As a result, the degree of insulation is affected by the material properties and surface tension is an important factor. This thermal insulation effect allows the production of high-quality samples and excellent mechanical properties. However, when casting materials with low surface tension are used, the melt may penetrate deeply into the grooves of the shot-sleeve, lessening the insulation effect and leading to the defect.

From this work, the mechanical properties can be improved and the high UTS 390 MPa was obtained, which is closed to some ferrous foundry alloys. We believe that this work may contribute to new applications of casting aluminum alloys in automobile parts. Replacing 30% of the steel with aluminum alloy is expected to reduce CO2 emissions by approximately 5 tons per vehicle.